CRANFIELD UNIVERSITY

Sandra Royo Pérez

THERMOELECTRIC ENERGY HARVESTING FOR WIRELESS SELF POWERED CONDITION MONITORING NODES

School of Engineering
Department of Power and Propulsion

MSc by Research
Academic Year: 2012- 2013

Supervisors: Prof. David Mba
Prof. Rob Dorey

May 2013

CRANFIELD UNIVERSITY

School of Engineering

MSc by Research

Academic Year 2012- 2013

Sandra Royo Pérez

THERMOELECTRIC ENERGY HARVESTING FOR WIRELESS SELF POWERED CONDITION MONITORING NODES

Supervisors: Prof. David Mba
Prof. Rob Dorey

May 2013

ABSTRACT

Condition monitoring of machines and structures is commonly utilized in order to prevent failures before they can occur. For these reasons, data such as temperature, vibrations or displacements are collected and analysed. Sensors collect this information, which is sent to a base station to be examined. Wired sensors have been used since the appearance of condition monitoring maintenance; however, wireless sensors are becoming more popular in this area. The use of wired sensors can be very expensive, due to the cost related to the installation and maintenance of the wiring between the sensors and the base station.

In wind turbines, wired sensor networks are starting to be substituted by wireless sensor networks. However, for tidal turbines, such as those developed by Delta Stream, this is still a challenge.

The use of batteries to supply energy to sensors is not an optimal solution for turbines that are located in remote areas. Batteries have a limited life and their replacement is costly and complicated. Thus, alternative sources of energy have to be found. The environment found in a tidal turbine provides several sources of profitable energy, such as vibration and temperature differences which can be used to supply energy by means of energy harvesters.

The aim of this project is to demonstrate the operation of self-powered short-range wireless sensor nodes for a potential use in a Delta Stream nacelle of tidal turbine. This project focuses on the wireless communication inside the nacelle (where most of the sensors are located) using a land protocol (Zigbee), and the energy harvesting using waste heat by means of thermoelectric devices.

In order to prove the operation of the whole system (thermoelectric generator and sensor node), a power management circuit was also constructed and tested.

Keywords: Wireless sensors, tidal turbine, thermoelectric harvester, temperature difference, Zigbee.

ACKNOWLEDGEMENTS

I would like to express my heartily gratitude to Prof. David Mba for giving me the opportunity to carry out this project, for his guidance and encouragement. I would also like to thank Prof. Rob Dorey for his help, guidance and patience during this thesis.

I am deeply grateful to the laboratory technicians, especially Matthew and Norman, for their endless patience and help, as well as all the people from building 70, especially Ewa, Alex and Dr. Paul Jones, for their help during my hours in the lab.

Particular thanks to my office mates for their kindness, support and help, for all the laughs and the good moments that we spent together. My warmest thanks also to my best friends here Yoli, Marta and Bruce for making life easier in Cranfield.

I would also like to thank my family, for their endless love and support in all ways.

Last but not least, I am deeply thankful to my boyfriend Cristóbal for his patient listening, endless love and his support in the good and mainly in the bad moments, helping me to improve in all the aspects of my life.

TABLE OF CONTENTS

LIST OF FIGURES

LIST OF TABLES

LIST OF EQUATIONS

LIST OF ABBREVIATIONS

ADCP	Acoustic Doppler Current Profile
bps	Bits per second
CBM	Condition based monitoring
CCTV	Closed circuit television
CU	Cranfield University
DC	Direct current
ESR	Equivalent Series Resistance
GPRS	General Packet Radio Service
GSM	Global system for mobile communications
IC	Integrated circuit
IEEE	Institute of electrical and electronics engineers
IP	Internet Protocol
ISA	Industry Standard Architecture
LP-WPAN	Low power- Wireless Personal Area Network
MEMS	Microelectromechanical systems
MPP	Maximum Power Point
MPPC	Maximum Power Point Control
MPPT	Maximum power point tracking
PV	Photovoltaic
PVDF	Polyvinylidene Fluoride
PZT	Ceramic Zirconate Titanate
RF	Radio frequency
SIM	Subscriber Identity Module
TEG	Thermoelectric generator
UK	United Kingdom
UWSN	Underwater wireless sensor network
WLAN	Wireless Local Area Network
WPAN	Wireless Personal Area Network
WSN	Wireless sensor network
WWAN	Wireless wide Area Network

NOMENCLATURE

$\dot{q}_{thompson}$	Heat flux due to the Thomson effect
A	Area of the small-scale generator
A_c	Cross sectional area
A_p	Area of the plates of the capacitor
C	Capacitance of the capacitor
C_{bat}	Capacity of the battery
C_{cap}	Capacity of the capacitor
C_{var}	Capacitor variable
D	Distance between plates in capacitors
E	Electrical field in thermoelectric device
E_c	Stored energy of a capacitor
E_{max}	Maximum stored energy in supercapacitors and batteries
F	Electrostatic force in the capacitor
I	Electric current
I_{HARV}	Harvested electric current
J	Electrical current density
$\boldsymbol{j_{el}}$	Vector of electric current density
K_{th}	Thermal conductance of the thermoelectric device
L	Length of the leg of the p or n material
L^*	Lorenz factor
M	R_L/R_{th}
m^*	Mass effective of the carrier
M_p	M at maximum output power
M_η	M at maximum efficiency
N	Number of thermocouples in the thermoelectric device
n	Carrier concentration
P_{output}	Output power
$P_{outputmax}$	Maximum output power
Q	Heat flow in thermoelectric device
$\boldsymbol{q}$	Heat transfer rate per cross-sectional area
Q_c	Heat flow dissipated

Q_{cond}	Heat conduction
Q_h	Heat flow absorbed
Q_p	Q charge on the plate of the capacitor
R_L	Resistance of the load
R_m	Thermal resistance of the material
R_{th}	Resistance of the thermoelectric device
S	Value of u that maximizes the reduced efficiency
T	Temperature
T_1	Temperature of the cathode in thermionic harvester
T_2	Temperature of the anode in thermionic harvester
T_{amb}	Ambient temperature
T_c	Temperature of the cold side in the thermoelectric device
T_{CJ}	Temperature of the cold junction in the thermoelectric device
T_H	Temperature of the hot side in the thermoelectric device
T_{HJ}	Temperature of the hot junction in the thermoelectric device
T_m	$(T_h+T_c)/2$
U	Relative current density in the thermoelectric device
V	Voltage
V_{bat}	Battery voltage
V_{BAT}	Battery voltage to charge the capacitor in electrostatic harvesters
V_{cap}	Capacitor voltage
V_L	Voltage in the load
V_{th}	Voltage of the thermoelectric harvester
W	Potential dependent of the work function of the material in thermionic harvester
Z	Figure of merit of the thermoelectric generator
zT	Dimensionless figure of merit of the material in thermoelectric generator
α	Seebeck coefficient
ΔT	Temperature difference between hot and cold side
ε_0	Permittivity of the free space
η_{carnot}	Carnot efficiency
η_{max}	Maximum efficiency
η_r	Reduced efficiency in thermoelectric generator

K	Relative permittivity in the dielectric in the capacitor
κ	Specific thermal conductivity material in thermoelectric generators
κ_e	Thermal conductivity provided by free electrons
κ_l	Lattice component of the thermal conductivity
K_m	Thermal conductivity in thermoelectric harvesters
M	Thomson coefficient in thermoelectric harvesters
μ	Carrier mobility in thermoelectric harvesters
μ_2	Electrochemical equilibrium potential in thermionic harvester
Π	Peltier coefficient in thermoelectric harvesters
P	Density of the air
Σ	Electric conductivity

1 INTRODUCTION

Since the industrial revolution, energy generation has been based on non-renewable sources of energy such as oil, gas and coal. However, by the end of 1990, due to increasing awareness about the climate change, the Kyoto protocol was established. The Kyoto protocol is an agreement among the countries of the United Nations with the aim of reducing the emissions of greenhouse gases [1]. From this moment on, renewable energy began to be highly demanded. Sustainable energy sources to generate power were the future, such as solar energy, wind power, biomass, geothermal power and tidal energy. However, in 2009 the world energy consumption was distributed as shown in Figure 1, and only 12% of the sources of energy were renewable.

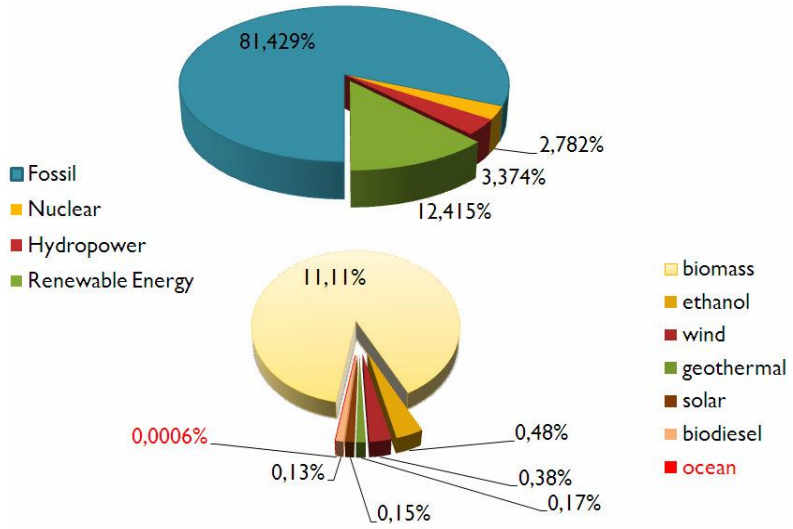

Figure 1: Renewable energy source share from the world energy consumption in 2009 [1]

In 2008 the European Union created the package called 20-20-20 [2], whose main objectives for 2020 were to:

- Reduce the greenhouse gas level by 20% (with respect to 1990 levels).
- Increase share of renewable energy to 20%.
- Reduce the energy consumption by 20%.

Thus, new sources of renewable energy have to be found. Wind energy and solar energy are well known and established. However, marine renewables sources are not widely used yet, despite 70% of the Earth being covered by water. The marine renewable energies that can be found are the following:

- Potential energy of the water mass driven by the tides. Dams are necessary.
- Kinetic energy provided by the tides. Turbines are required to make use of this energy source.
- Wave energy.
- Ocean thermal energy: It uses the temperature difference between the surface and the bottom water masses.
- Osmotic power: Energy is generated from the difference of salinity between two water masses.
- Offshore wind power: Wind turbines installed offshore.
- Marine Biomass: Energy from the biofuel (microalgae).

Tidal energy converts the kinetic energy from the tides into electricity. As tides are predictable (more predictable than wind or solar energies), tidal energy has enough power to be the energy source of the future [3]. It is believed that 3% of the 20% of the renewable energy required for 2020, in UK, will be provided by tidal energy [4]. Although, they have the potential of providing 15-20% of the energy needs of UK. 80% of the tidal potential of Europe can be provided by the UK's sea water [3]. Figure 2 shows the tidal potential in UK waters.

Due to this boom in the tidal energy and with the aid of the UK government, many projects of tidal turbines have been developed, including that by DeltaStream and focus of this thesis.

Tidal turbines are placed on the seabed, and as other machine or structure, it is necessary to ensure its correct operation. Thus, the monitoring of the condition of each component of the turbines is of great importance.

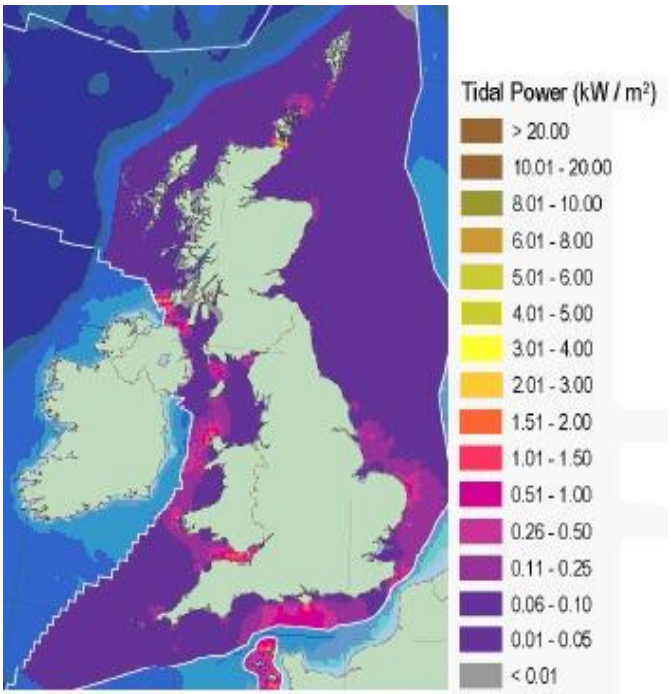

Figure 2: Map showing the tidal energy potential around UK

Today, condition monitoring is used in most of the maintenance plans of structures and machines. The objective of applying a condition monitoring strategy is to know and predict failures before they can occur or become catastrophic. For this reason, sensors are required in order to collect different kinds of data such as temperature, vibrations and pressure displacement. These data are sent to a base station where they are analysed to detect and diagnose possible failures.

Sensors can be connected to the base station using wires or wirelessly. From the beginning of condition-based maintenance, wired sensors have been used, but in recent years wireless sensors have started to become very popular in the market [5] (Figure 3). From 2003 to 2012 the growth of the wireless sensor market has been exponential.

With the use of wireless sensor nodes, the installation and maintenance of the wires are avoided and consequently, a reduction in costs is attained. Thus, they are very useful and convenient sensors for remote areas where the access is difficult and restricted.

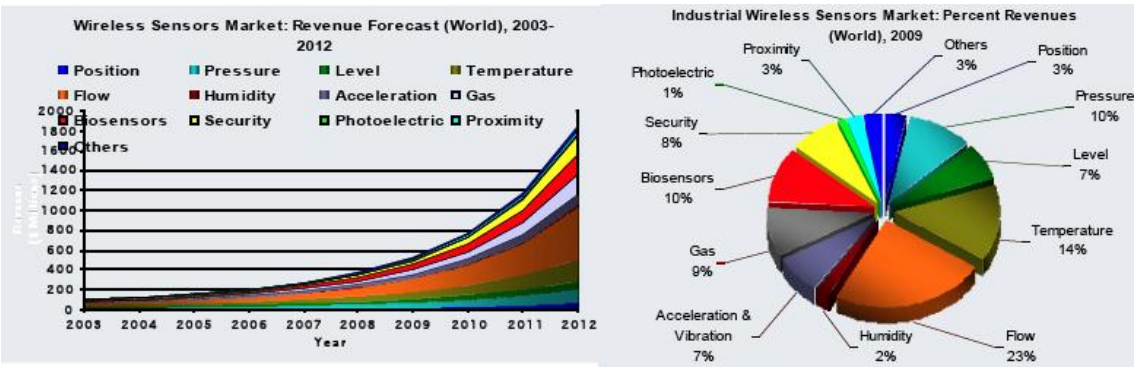

Figure 3: Worldwide wireless sensor market forecast from 2003-2012 [6]

Wireless sensor nodes are composed of three parts: sensing part (sensors that collect the data), processing unit (which treats the data from the sensing part) and transmitter unit (to send the information to the receiver). Moreover, they need a source of electrical energy to be able to work. Batteries are usually utilized for this purpose, but their main drawback is their limited lifetime and the necessity for regular replacement.

In order to solve the problem of the energy supply, other sources need to be considered. The environment provides numerous sources, such as vibrations, sunlight and temperature differences that can be converted into electricity. Devices that carry out this function are called energy harvesters. Large-scale energy harvesters are well known such as wind turbines, solar panels and tidal turbines However, for powering sensor nodes small-scale energy harvesters are needed.

In wind turbines, wireless sensors and energy harvesters are starting to be implemented [6], although slowly [5]. For tidal turbines, it is still a challenge due to the location of the turbines and the communication protocol.

The monitoring of the condition of different components in the tidal turbine is carried out by means of wired sensors. The location of the turbines in a remote area means that the installation and the maintenance of the wires are very costly. In order to be able to solve this problem, this project focuses on the possibility of using wireless sensor network in tidal turbines.

Tidal turbines are located below sea level [7], so batteries may be used as energy source for sensor nodes. However, batteries need to be replaced regularly, which would be an arduous and costly task in such a location. Among the possibilities that the environment in the turbine can offer, temperature differences have been selected as a source of energy for the different sensors, due to the high levels of energy potentially available.

Thermoelectric devices are energy harvesters that can transform temperature differences into electricity. In the nacelle of the tidal turbine, hot surfaces can be easily found such in the generator cover or gearbox casing. Thermoelectric harvesters are robust, inexpensive and have no moving parts. Hence, they are an ideal energy source for the sensors.

1.1 Aim and objectives

The aim of this project is to demonstrate the operation of a self-powered short range wireless sensor node for monitoring the condition of many components inside the nacelle of the turbine. In order to achieve this aim the following objectives have been defined:

1. Review of power requirements for typical sensors found in a DeltaStream tidal turbine and their distribution. Review of wireless transmission technologies and the energy harvesting capabilities in small scale harvester technologies.
2. Evaluate the available energy sources and environmental conditions found in tidal turbine nacelles.
3. Identification of the suitable pairing of sensor node, harvesting and transmission technologies.
4. Determine the power harvesting capability of thermoelectric devices under conditions found in tidal turbine nacelles.
5. Demonstrate and evaluate the operation of a self-powered short range wireless sensor node.
6. Demonstrate the proof of concept energy harvesting system and install it on a real machine to study its behaviour.

2 LITERATURE REVIEW

2.1 Condition monitoring

Since the development of structures and machines, maintenance programs have been required. These maintenance programs have evolved over the years. In the beginning, maintenance actions were carried out only when failures occurred in an approach termed breakdown maintenance. The costs attached to maintenance were extremely high due to the extensive damage caused to the system, the unplanned shutdowns and the safety issues.

Later, scheduled maintenance was implemented to prevent breakdown in machines and structures. However, many times, these scheduled actions were unnecessary. If the maintenance was performed too early, the remaining life of the components would be wasted. On the other hand, if the maintenance was carried out too late, the failure could occur before the maintenance was performed. Finally, predictive maintenance was introduced in order to achieve efficient, reliable and economic maintenance programs.

Condition based monitoring (CBM) is the main component of predictive maintenance. It consists of the collection and analysis of data from the structures and machines (such as vibrations, temperatures, displacements and so on), in order to detect the failures before they occur. A parameter, that indicates the condition of the machine, is selected and measured regularly. If a significant change in the parameter occurs, it indicates that a failure could have developed in the machine. The detection of possible failures and the prediction of the future problems allow engineers to carry out maintenance actions in the system before these failures can become catastrophic.

The implementation of condition based monitoring (CBM) has to be justified because, although it presents many advantages, the initial capital investment is extremely high. However, if it is efficiently implemented, the final maintenance can be reduced. Likewise, unexpected shutdowns due to failures and scheduled preventive maintenance will be reduced or eliminated.

The condition based monitoring is carried out by means of these steps [8]:

- Selection of the parameters to be measured: In order to monitor the condition of the machine, there are certain parameters which could be mainly affected by the failures. Thus, they should be the parameters to monitor.
- Selection and installation of the measuring instruments: When the parameters to be measured are selected, sensor nodes have to be carefully installed as well as the connection established.
- Data collection: The parameters measured by sensors are collected in order to obtain the necessary information to monitor the health of the structure.
- Data processing: In this step, the information collected in the step above is analysed. For instance, if the data taken are different from the data of healthy condition, a failure could be starting to occur.
- Decision-making step: According to the data analysed in the step before, the effective maintenance task must be carried out.

Once the steps to carry out condition monitoring are described, the second step (selection and installation of the sensor nodes and connections) is carefully explained.

It is assured that sensors are required in order to collect the data to be analysed. Sensors can be stand-alone or they can be part of a sensor network. In the latter case a base station, where the information is collected, is required. The sensor output can be sent to the station wirelessly or via cables.

Wired sensors have been used and are still being used in condition monitoring, but wireless sensor nodes are slowly imposing in this area [5]. Wired sensors are high costs due to the installation and the maintenance of the cables. Moreover, excessive time is spent in the arrangement of wired sensors incurring further costs. Wireless sensor nodes need low power, have light weight and small size, are robust and more suitable for condition based monitoring in remote areas where the access is too difficult and costly.

The main problem associated with wireless sensors is the necessity for an energy source to supply power, which in some instances is provided by batteries. These batteries have a limited life, so they have to be replaced after a certain period of time.

The change of batteries can be highly costly if the sensors are located in remote areas such as tidal turbines. In order to avoid these high costs, new sources of energy have been developed. Energy harvesters convert energy that can be obtained from the environment (such as vibrations, solar energy, air flow energy or temperature differences) into electrical power. A forecast noted that in 2011, the utilization of energy harvesters for wireless sensors would reach 1.6 million units, which equates 13.75 million dollars in sales [6]. For 2021 the sales would increase up to 4 billion dollars.

2.2 Tidal energy

2.2.1 Introduction to tides

Ocean tides are produced due to the action of the gravity of the Moon and the Sun. This causes the level of the water to increase and decrease predictably. According to the gravitation law of Newton, the gravity force between two bodies (A and B) can be expressed as follows (equation (2-1)):

$$\mathrm{F} = \mathrm{G} \cdot \frac{m_a \cdot m_b}{d^2} \quad \textbf{(2-1)}$$

Where m_a and m_b are the masses of the bodies, G the constant of gravitation ($6.6738\ 10^{-11}$ Nm^2/kg^2) and d the distance between them. Although the Sun and the Moon are both directly related to the generation of the tides, the Moon exerts a higher influence on them (see Figure 4). When the moon is aligned with the Sun, the range of the tide reaches its maximum, and is called spring tide. However, when the Moon is located 90º with respect to the Sun, part of the Sun's force, that creates the tides, is cancelled by the moon, so the range of the

tide reaches its minimum value (neap tide). In this manner, tides can be predicted and used to generate energy.

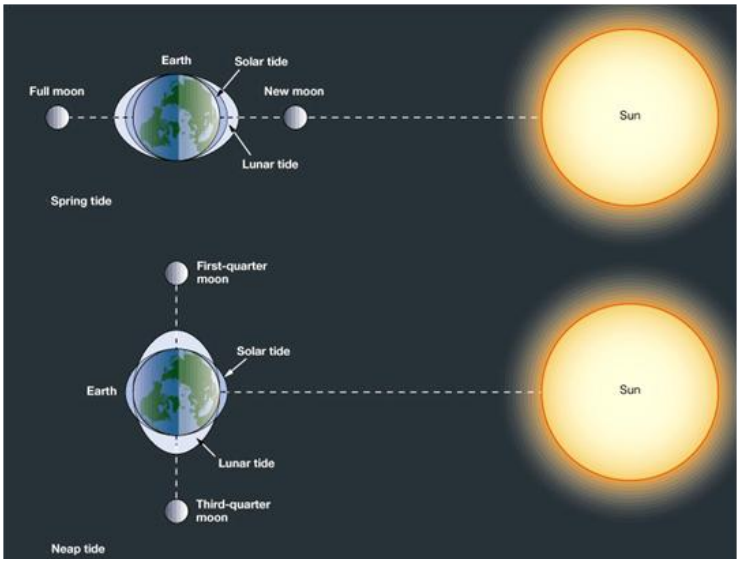

Figure 4: Behaviour of the tides depending on the situation of the moon [9]

2.2.2 Tidal energy

Energy from tides can generally be extracted by means of two ways. In the first way, dams are required, to store and release a large amount of water mass. However, in the second way, turbines are necessary in order to extract the power from the water flow.

The use of dams was the main energy source to generate electricity from tides. But, the required barriers or dams have many drawbacks. The main one is that it requires an enormous civil construction, with high costs and with dire consequences for the environment [9]. For this reason, interest in tidal turbines farms started to grow, as their environmental impact is lower and the installations are less costly. Here, the studies are focused on tidal turbines.

The basic principle of the extraction of energy by means of turbines is the conversion of kinetic energy into electrical energy. The kinetic energy of a body (E_k) with a certain mass (m [kg]) that moves with a speed v (m/s) can be depicted as follows (equation (2-2)):

$$E_k = \frac{1}{2}mv^2 \quad \textbf{(2-2)}$$

The power that can be available from a water mass with a speed v (m/s), the water flow ($\dot{m}$) in m/s through a unit area (A) is calculated:

$$\dot{m} = \rho \cdot \mathrm{A} \cdot v \quad \textbf{(2-3)}$$

where ρ is the density of the sea water.

Hence, the power available through the tidal flow is given by the following equation (2-4):

$$\mathrm{P}_{av} = \frac{1}{2}\dot{m}v^2 = \frac{1}{2}\rho \mathrm{A}v^3 \quad \textbf{(2-4)}$$

For turbines, the area (A) can be represented as the rotor area. If it has a radius r and the efficiency of the turbine is η, the power extracted by the turbine is depicted in equation (2-5).

$$\mathrm{P}_{ext} = \frac{1}{2}\eta\rho\pi r^2 v^3 \quad \textbf{(2-5)}$$

For wind turbines, η can reach a value of 50% [10].

2.2.3 Tidal turbines

Tidal turbines work using similar techniques to the techniques that wind turbines use. Tidal turbines can be mainly classified into four groups: Horizontal axis, vertical axis, venture based and cross flow. [11]

- **Horizontal axis**: These tidal turbines work in the same way as wind turbines do. These turbines are located on the seabed. The water stream is parallel to the seabed and also to the axis of the rotor of the turbine. The water flow moves the blades of the turbine producing energy by means of the generator.

  One example of this kind of turbine is that developed by SeaGen. It was connected in 2008 and it generates 1.2MW [12]. Each turbine is mounted in a two arm-like extension with a rotor diameter of 16 metres. The

maximum efficiency achieved is 89% [13]. DeltaStream project is another example of this type of turbines. It will be explained below.

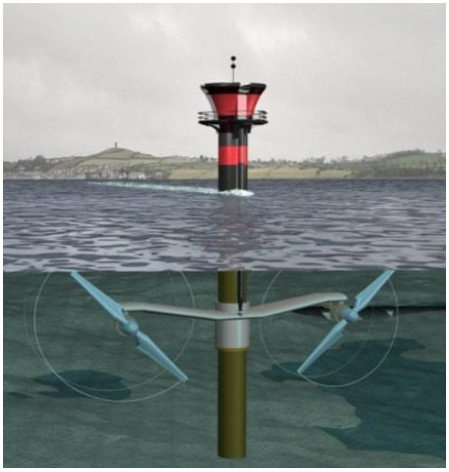

Figure 5: SeaGen turbine [14]

- **<u>Vertical axis:</u>** The axis of the turbine is orthogonal to the water flow and also to the seabed. The main advantage of these devices is that the blades can be enlarged horizontally, engaging with higher amounts of water flow [14]. The turbine developed by Kobold is an example. It has 3 vertical blades and with a 6 meters of diameter. At water flow of 2 m/s the power produced is approximately 25 – 30 kW [15] (Figure 6).

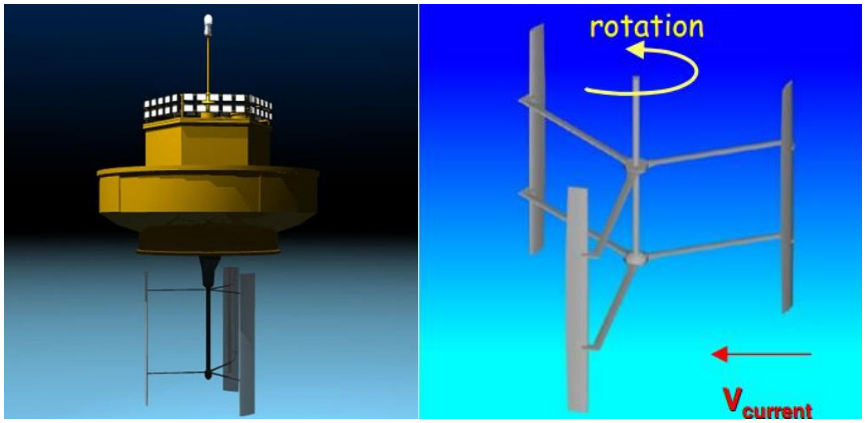

Figure 6: Kobold turbine (vertical axis) [15]

- **Venturi based turbine**: These turbines have a horizontal axis, but they present a venturi-shaped duct, whose function is to accelerate the water stream. Consequently, increasing the power extracted for a determined value of the radius of the rotor. Figure 7 shows the project of Lunar Energy Limited [16].

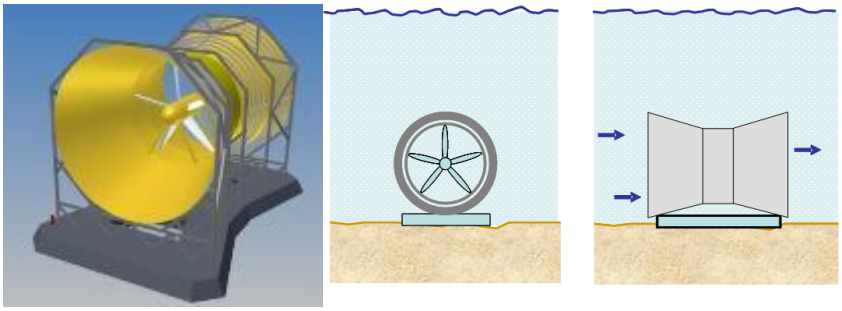

Figure 7: Venturi turbine by Lunar energy limited [17]

- **Cross flow turbine**: The axis is parallel to the seabed, but it is orthogonal to the water flow. Atlantisstrom has developed a model [17], although, it is mainly used in rivers (Figure 8).

Figure 8: Cross flow turbine by Atlantisstrom [18]

2.3 Horizontal axis tidal turbines

2.3.1 Turbine description

As explained above, in horizontal axis tidal turbines, the water stream is parallel to the seabed and to the axis of the rotor of the turbine.

One type of these turbines has been developed by DeltaStream. It works like a wind turbine, but it uses water flow instead wind flow. The water flow turns the blades of the turbine and electricity is obtained by means of the generator located in the nacelle. The electricity is transmitted to shore through submarine cables. The communication between the tidal turbines and shore is via submarine cables as well.

The power unit of the DeltaStream turbine is composed of three turbines connected in a triangular frame 30 meters wide and weighing 250 tons. They are located on the sea floor around 31.5 meters below the surface of the sea. The minimum distance from the tip rotor to the sea surface is approximately 10m at the lowest tide. Thereby, the turbine is under water for high and low tides. The rotor of each turbine is 15 meters in diameter and the nacelle of each turbine has a dimension of 2x 9 meters [7] (Figure 9). Each unit produces 1.2 Megawatts of power. They are located in Ramsey Sound, Pembrokeshire in Wales.

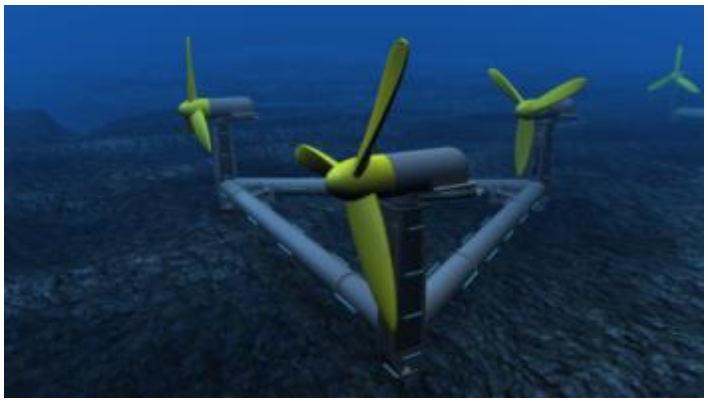

Figure 9: Delta Stream tidal turbines [18]

2.3.2 Sensor network in Delta Stream tidal turbine for condition monitoring

With the aim to know the distribution of the sensors in the different parts of the tidal turbine, typical power requirements and the location of sensors in the Delta Stream tidal turbines are shown in Table 1. In this particular configuration, each group of three turbines is connected to a base station where there is a cable junction box. From this base station the information is sent to the on-shore

base. Power needed by the sensors is provided by a shore base station using cables and through an auxiliary transformer enclosure [19]. This transformer is mounted in one of the vertical towers of the turbines. It provides energy for all auxiliary instruments and for the yaw system in the turbine.

Table 1: Types of sensors used in a Delta Stream tidal turbine

Turbine component	Type of sensor	Number of sensors	Function	Typical Power requirement per sensor	Location
Rotor	Strain gauge	18 connected every 6 to a router to transmit to the base station	Detection of defects or cracks	3mW-27mW (3-5V)	Blades
	Accelerometer	3 connected to a router to transmit to the base station	Detection of defects due to destructive vibration.	500μW - 50mW (3.6-5V)	Blades
Pintle	Strain gauge	8	Detection of defects	27mW (3-5V)	
Gearbox	Acceleration sensor	6	Detection of any failure in the component of the gearbox.	500μW - 50mW (3.6-5V)	Gearbox cover
	Aqua sensor	1	Monitoring of the oil quality, warning when it is degraded	-	Inside the lubrication oil system
	Torque sensor	1	Detection of overloading of the shaft in the gearbox	50mW-150mW (5V)	Gearbox shaft

Turbine component	Type of sensor	Number of sensors	Function	Typical Power requirement per sensor	Location
Gearbox	Metallic contamination sensor	1	Detection of the damage in the components of the gearbox	120mW-600mW	Inside de lubrication oil system
	Speed sensor	1	To monitor the rotating speed of the shaft	-	Shafts in the gearbox
Generator	Temperature sensor	5	To ensure the generator is working in the correct range of temperature	1.1 mW-2.75 mW (5.5V)	Generator
	Current sensor	1	To monitor the output power	0.4 W- 2.5W (10-15V)	Generator
Hydraulic system	Pressure sensor	10	To ensure the correct operated pressure, and to detect oil leakage.	560mW-700mW (5.5 V)	Hydraulic system
	Linear transducer	2	Detection of failures in actuators	6 W	Hydraulic actuators
Chassis	Leakage sensor	2	Detection of water	3 W	Inside the chassis

Turbine component	Type of sensor	Number of sensors	Function	Typical Power requirement per sensor	Location
Structure	Strain gauges	8	To monitor frame stresses	3mW-27mW (3-5 V)	In the frame where is expected high stress.
	Passive acoustics	3	To detect impact of marine animals	150mW	Around the frame
	CCTV	3	An underwater camera to monitor general condition	15W	In the frame
	ADCP (Acoustic Doppler current profile)	3	To record the current velocity to monitor the performance of the turbine	1.7W-2.2W	Water around the turbine
NUMBER OF DEVICES		78			

The structure is shared by the three turbines, thus, in total there are 200 sensors. Most of them are located in the nacelle. According to the number of sensors required, the quantity of wires needed is high. The installation and maintenance of them is extremely costly. Most of the sensors consume power on the order of miliwatts with a range of voltages from 3 to 5 V. Other sensors have higher power consumption with higher voltages.

2.4 Land and underwater wireless sensor nodes

Wired sensor nodes are well-known and well established. However, wireless sensor nodes are relatively new. Besides its installation, the connection and communication protocols are different from wired sensors. Moreover, depending on the location (underwater or land), the communication of wireless sensor nodes will also change. The difference and comparison of both wireless sensor nodes types are described.

A wireless sensor node is composed of three segments: sensing element, data processing unit and communication interface. The sensor node is connected wirelessly to a gateway which sends the data to the final user (computer). The power consumption of the sensor node depends mainly on the, communication protocols, the data sampling frequency and the time of synchronization. If more than one sensor is connected to the gateway, the power consumption depends also on the number and the distance of the sensors, and the topology of the WSN (Wireless sensor network). The topology of the sensors refers to the way in which multiple sensors are connected. Mainly, the topology of the wireless sensor can be star, tree or mesh (Figure 10).

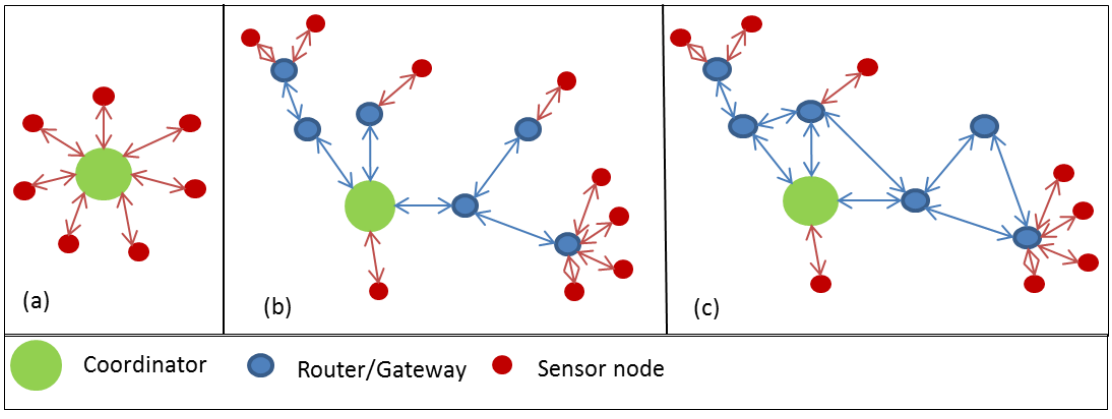

Figure 10: Topology of Wireless sensor nodes, (a) star, (b) tree, (c) mesh

As Figure 10 (a) shows, in star topology all the sensor nodes (end devices) are connected to one coordinator (computer). This coordinator organises and sends the instructions to the end nodes. However, in the tree and mesh topologies, the end devices are connected to one router that transmits the information to the

coordinator where it is analysed. The difference between mesh and tree is that in mesh all the routers are connected to each other, which allows any information to be transmitted to another end device.

The main differences between land and underwater communication are described in the next paragraph. The most important communication protocols in land and their characteristics are depicted in Table 2.

As shown in Table 2, for long range applications, Wi-Fi and WiMAX are the most common protocols, reaching a range of several kilometres. However, for short range communication, ZigBee, Bluetooth and Enocean protocols are more suitable. Besides their low power consumption, they are characterised by low cost and low complexity compared to other communication networks. Hence, for wireless sensor nodes where low power consumption is required, these protocols are appropriate. One example of a terrestrial wireless sensor network with ZigBee- Wi-Fi protocol and a mesh or tree topology is the kit developed by PrismaSense [20]. The coordinator (laptop or computer) is connected to the router (gateway) by Wi-Fi in order to reach long distance of communication. The end device (sensor node) is connected to the gateway by the Zigbee protocol, whose range is 30m indoor or 100m outdoor.

Apart from the technologies depicted in Table 2, GSM and GPRS technologies are commonly used. Instead of local or personal network area, these technologies use a global area. In GSM (Global System for Mobile communications) a channel is reserved for the data communication. The cost of this communication is proportional to the time that the line is utilized. However, in GPRS (General Packet Radio Service), data are sent as packets, the connection is made through internet and a network IP is required. The cost of the communication depends on the quantity of data transmitted. GPRS is much faster than GSM and has a reasonable cost. GSM is the system that mobile phones utilize and GPRS is used in the last technology mobile phones that use the internet.

Table 2: Wireless protocols of communication in land [21]

Standards	IEEE 802.15.4 (LP-WPAN)				IEEE 802.15.1 (WPAN)	IEEE 802.11 (WLAN)	IEEE 802.16 (WWAN)	ISO/IEC 14543-3-10 8 (WPAN)
	ZigBee	**6LoWPAN**	**WirelessHART**	**ISA 100.11 a**	**Bluetooth**	**WIFI**	**WiMAX**	**Enocean**
Range	30m indoor; 100m outdoor	50m	-	-	100m	5km	15km	30m indoor; 300 outdoor
Data rate	250 kbps	250Kbps	250Kbps	250Kbps	1 Kbps-3Kbps	1Mbps-450Mbps	75Mbps	125Kbps
Frequency	2.4 GHz	2.4 GHz	2.4 GHz	2.4 GHz	2.4 GHz	2.4 ,3.7 and 5 GHz	2.3 ,2.5 and 3.5 GHz	868MHz/315MHz
Topology	Star, mesh, Cluster tree	Star, mesh, Cluster tree	Star, mesh, Cluster tree	Star, mesh, Cluster tree	Star	Star, Tree, P2P	Star, Tree,P2P	Star
Applications	Wireless sensor (monitoring and control)	Wireless internet	Wireless process, monitoring and control applications	Wireless systems for automation	Wireless sensor (monitoring and control)	PC-based Data Acquisi-tion Mobile internet	Mobile Internet	Wireless sensor networks (building and industrial automation)

In order to build a wireless sensor network (WSN) in terrestrial applications, there is a wide range of protocols of communication, depending on the technology or the distance range that is required to cove WSN can be achieved in a low cost manner, due to the low prices of the sensor nodes, US$ 100 [22], and the low cost in the communications (Zigbee, Bluetooth or Enocean).

On the other hand, the application of land wireless technology in underwater systems presents extremely difficult challenges. Firstly, sensor nodes on land have low cost, however, commercial underwater nodes are very costly, such as 10k US$ [22]. Secondly, the high attenuation in the propagation of the electromagnetic waves under water limits the transmission distance. As the wave frequency increases the attenuation also increases. For frequencies such as 2.4 GHz (see Table 2) the communication underwater is almost impossible to maintain due to the high attenuation in water. For radio frequency waves, the propagation is limited to less than a few meters at very low frequencies (30-300 Hz) [23], requiring high power and large antennas to be able to send or receive the information between nodes [24]. The communication range would extend to few millimetres, if frequencies of 2.4 GHz were used underwater. Thus, communication underwater has to rely on other technologies like acoustic communication to be able to transmit over higher range.

In acoustic modems, the frequency utilized is much lower (kHz) (see Table 3), depending on the application target. It also has to be noted that the speed of acoustic waves is less than $1.5x10^3$ m/s, compared to the speed of RF in the air of $3.8x10^8$ m/s. Hence, the average of the data rate is also lower. As can be observed in Table 2, the data rate achieved on land is from kbps to Mbps. However, in acoustic communication the highest data rate achievable is 1000 bps [24].

Table 3: Frequencies in underwater acoustic communication [25]

Range	Bandwidth
Long (10-100Km)	2-5 kHz
Medium (1-10km)	10 kHz
Short (100m- 1 km)	20-50 kHz
Very short (<100m)	>100 kHz

Although acoustic modems are usually utilized for long range distances, they are bulky and expensive and they consume a lot of power. However, in the literature, acoustic modems for short ranges communication are also found, with the same characteristics (price, range, size and consumption) as land based wireless sensor nodes. This means that acoustic modems can attain low costs, small size and low-power consumption. Examples of applications of acoustic modems can be found in [26], [23], [27; 28] and [29]. The achieved ranges goes are from 4m to 4km, and the power consumption covers from 24 mW to more than 500mW to while receiving and from 12mW to more than 500mW while transmitting [29].

In order to create an effective underwater wireless sensor network (UWSN), two aspects must be considered. Data transmission under water has to be acoustic, and transmissions inside the nacelle through the air will be established using one of the protocols described in Table 2 depending on the distance between the transmitter and the receptor. For example sensor nodes can be connected in a cluster using two antennas, one acoustic antenna used when the data transmission is underwater and another antenna for transmitting by Wi-Fi or Zigbee in open air [30]. In a similar way, a strain gauge connected to an acoustic transducer was located on an underwater composite turbine blade where data collected from the blade was sent to the receiver (in a platform close to the shore) through acoustic waves [23], and this platform is connected to the land station by Bluetooth (see Figure 11). The energy supply used for the strain

gauge in this example and the transducer was a coin battery of 3 Volts that has to be replaced every two years.

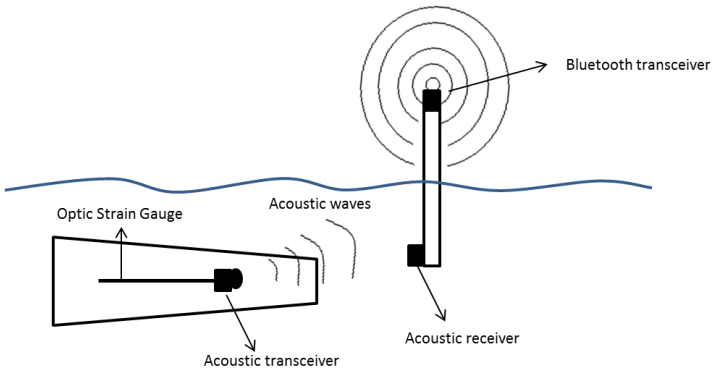

Figure 11: Schematic of the communication from a blade turbine to shore using both acoustic and electromagnetic transmission [23].

2.5 Small scale energy harvesting

2.5.1 Justification of energy harvesting technologies

As explained in the previously, sensors are used for monitoring the condition of machines. These sensors require power and batteries or wires connected to a source of energy that provide power. Batteries have a limited life time and they have to be replaced. On the other hand, wires need installation and a maintenance process. In places where the accessibility is not difficult, this may not be a significant problem. In remote areas with limited access the changing of batteries or the installation of wires can be costly. Thus, another solution has to be developed. One of these solutions are energy harvesters. They can transform the available energy in the environment such as movement, sunlight and temperature differences into electricity.

2.5.2 Types of small-scale energy harvesting devices

2.5.2.1 Mechanical Energy

Energy harvesters which use vibrations as a source of energy are well established and are widely utilized to supply energy to small-scale devices.

Vibration can frequently appear in environments such as car engines, helicopters, aircraft wings, or simply in the human body with the variation of pressure or when walking. Hence, mechanical harvesters take advantage of these movements to generate electricity.

There are three main mechanisms that use vibration movement: Piezoelectric, electromagnetic and electrostatic. They are depicted as follows:

Piezoelectric

Piezoelectric materials produce electricity when mechanical pressure is applied or they are deformed (direct effect), (Figure 12). The voltage produced is proportional to the strain applied. Furthermore, these materials deform when an electrical field is applied. This phenomenon is called the converse effect.

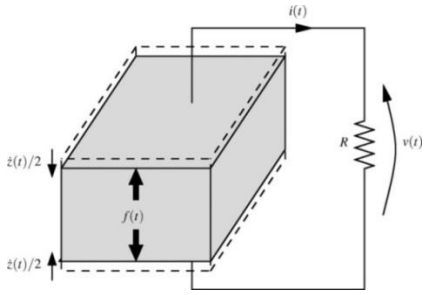

Figure 12: Schematic of the direct effect within a piezoelectric material [31].

Materials with piezoelectric properties can be found naturally such as cane sugar or quartz. Other synthetic piezoelectric materials used are polyvinylidene fluoride (PVDF) and the ceramic lead zirconate titanate (PZT). The latter is known for its high conversion efficiency and the most used [31].

To understand the behaviour of the piezoelectric materials, how the atoms are arranged in the crystal (lattice) has to be analysed. The smallest cell, where the atoms are place, is called ‘a unit cell’. In piezoelectric materials the unit cell is not symmetric. Within the piezoelectric materials can be distinguished pyroelectric and non-pyroelectric materials. Within the pyroelectric materials ferroelectric and non-ferroelectric materials are included (Figure 13).

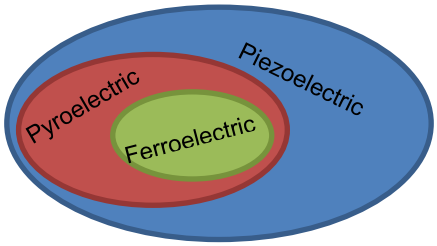

Figure 13: Classification of piezoelectric materials

In pyroelectric materials, permanent dipoles are present, which means that the average position of positive and negative charges does not coincide. Ferroelectric materials have permanent reversible polarisation. On the other hand, in non-pyroelectric materials, the average position of both charges coincides, but the dipole can be created when a mechanical pressure is applied.

Hence, when applying strain to the material, the material is deformed. The deformation results in the movement of the atoms in the crystals. In materials where dipoles exist, these move like the atoms, and in non-pyroelectric materials, the movement of the atoms generate the dipoles. The generation of dipoles, or their movement, create the polarization of the material, generating an electric field.

Electromagnetic (Inductive systems)

Inductive systems are based on Faraday's Law. The movement of a magnet in the presence of a round coil produces the variation of a magnetic flux that induces a voltage v(t) and thus, a current i(t) in the electric circuit. The mechanical movement of the magnet is caused by structural vibrations. The dimensions of the device are limited to the size of the coil, the spring attached to the mass in movement and the housing (see Figure 14). The power obtained reaches its maximum value when the resonance frequency is attained.

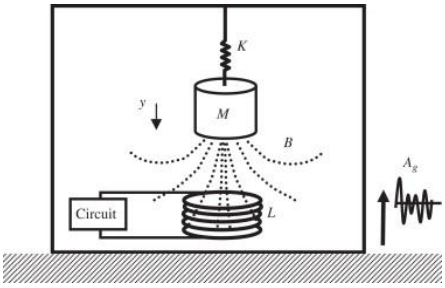

Figure 14: Schematic of a basic inductive system [32]

There are two ways to produces electromagnetism. The first involves a magnet is attached to the free side of a cantilever beam while the coil is fixed to the housing. In the second case, the coil is mounted on the beam and the magnetic mass is fixed. In the literature many electromagnetic devices are depicted [10; 31; 33-36], although the type of arrangement mostly utilized is the former, where the coil is fixed and the magnets are in movement. For instance, four-magnetic pole electromagnetic harvesters have been developed as energy source for sensor nodes for condition monitoring. The speed variation of the flux is the double, due to the presence of the four magnets. The generator, at 102Hz, produces 2.5 mW of power [36] (Figure 15). Another European project ("VIBES" [10]) developed a cantilever generator based on the same configuration producing 17.8 mW.

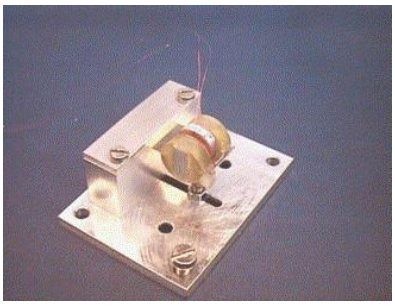

Figure 15: Electromagnetic generator based on four magnets in movement and coil fixed [36]

The advantage of this generator is the lack of mechanical parts in contact. Its reliability increases and the damping can be reduced. However, the miniaturizing to be able to integrate in MEMS is complicated. Firstly the electromagnetic materials, such as the coil, are too bulky. The larger the coil and magnet, the larger the power harvested. Moreover, when the device is

smaller, the resonant frequency is more difficult to achieve and lower power will be obtained [35].

Electrostatic (capacitive systems)

In capacitive systems, electrostatic energy is converted into electrical energy. Within a variable capacitor, the two plates are separated from each other by vacuum, air or another insulator. The vibration causes the distance or the overlap area between the plates to change. This vibration, in the presence of a fixed voltage or constant charge, produces electricity, as shown in Figure 16:

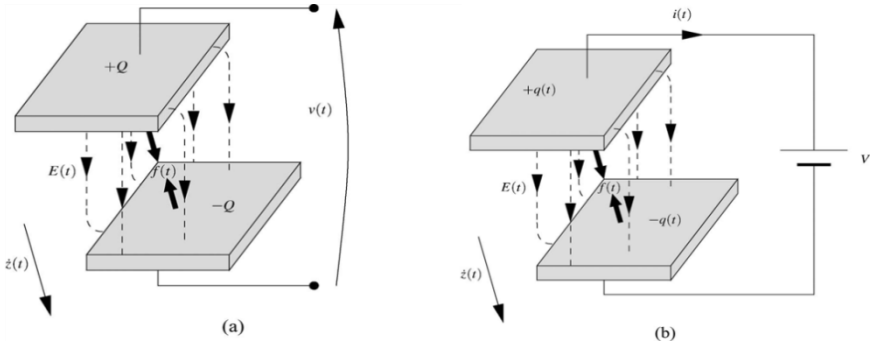

Figure 16: Principle of electrostatic harvester. (a) Fixed charge (b) Constant voltage [10]

Equation (2-6) governs the value of capacitor:

$$\mathrm{Q}_p = \mathrm{C} \cdot \mathrm{V} \tag{2-6}$$

where Q_p is the charge on the plate in Coulombs, V is the voltage in Volts and C is the capacitance in Faradays that can be expressed by equation (2-7).

$$C = \varepsilon_0 \kappa \cdot \frac{A_p}{d} \tag{2-7}$$

where ε_0 the permittivity of free space. It has a constant value of 8.854×10^{-12} $C^2/N\cdot m^2$ [37], κ is the relative permittivity of the dielectric material, A_p is the area of the plates in meters and d the separation between plates.

By considering the equation (2-6), when the charge is constant, if the capacitance increases the voltage decreases, and the stored energy (E_c) will be given by equation (2-8).

$$E_c = \frac{1}{2} C V^2 \tag{2-8}$$

In the first mode, the potential (V) is constant. When the mechanical vibrations appear and the capacitor is charged, the capacitor starts to discharge. A net charge is generated which induces a current $\mathrm{i(t)}$.

$$\mathrm{i(t)} = \frac{dQ}{dt} = V\frac{\partial C}{\partial t} \tag{2-9}$$

In Figure 17, a schematic of a pre-charge and current harvesting is shown when the voltage is fixed. V_{BAT} is the voltage necessary to charge the capacitor C_{var}. Once the capacitor is charged, the process of harvesting electric current (I_{Harv}) starts, until the capacitance of C_{var} reaches its minimum value. Thus, V_{BAT} charges again the capacitor to begin the cycle again.

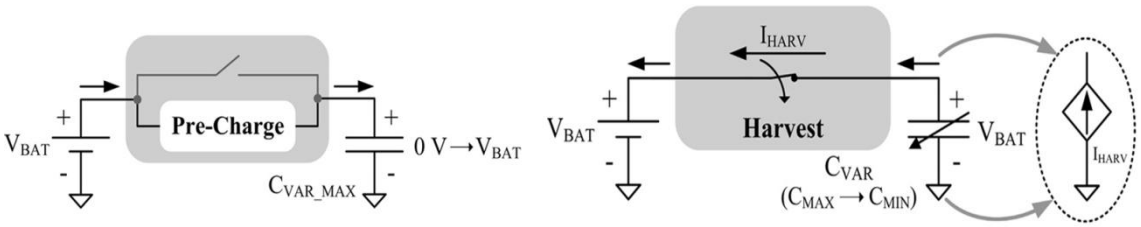

Figure 17: Schematic of pre-charge and current harvesting at constant voltage [38].

The electrostatic force in the direction of z is given by equation (2-10):

$$\mathrm{F} = \frac{1}{2} V^2 \frac{dC}{dz} \tag{2-10}$$

When the charge is constant, peaks of voltage are very high, up to 200V [38] and only a few enormously expensive materials can support these high voltages. However, if the voltage is fixed, voltages are lower, but another source of electricity is initially required (Figure 17). Although one solution for this problem is to use an electret, which is a dielectric material with permanent electric charge, its process of assembly is very complicated [10].

Alternatively, another source of electricity, such as a battery, is required for the device to start to work. Besides the necessity of other sources of energy, another drawback is found. In order to increase the capacitance of the capacitor, the distance between the plates has to decrease. Thus, reducing the distance between plates without touching each other in the presence of vibrations is extremely difficult.

The main advantage of electrostatic devices is that they can be miniaturized to be able to be used in MEMS scale. At small-scale, electrostatic devices can be of three types: In-plane overlap, in-plane gap closing and out of plane gap closing [34] (Figure 18).

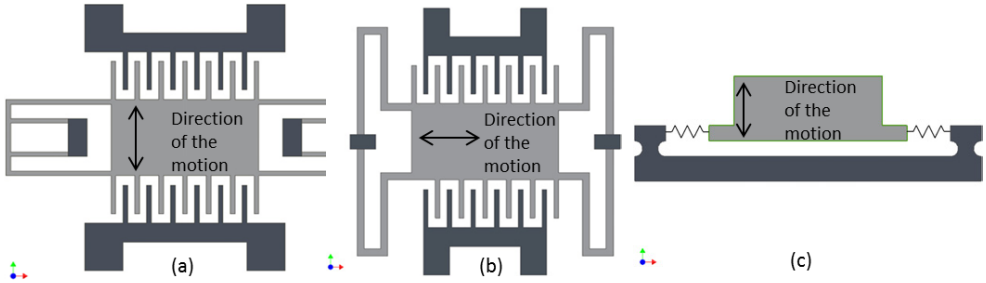

Figure 18: Schematic of electrostatic harvesters. (a) In-plane overlap (b) In-plane gap closing (c) out of plane gap closing

2.5.2.2 Solar energy

In order to convert solar energy into electricity, photovoltaic cells are frequently used. The most typical device make used of semiconductor (p-type and n-type) junctions made of silicon. Two types of cells, depending on the materials, are used: mono-crystalline silicon and polycrystalline silicon. In mono-crystalline silicon, the efficiency reached is around 20%, while in polycrystalline silicon is approximately 16% [39].

The principle of the solar energy harvesting can be described as follows: Solar cells are formed by p-type material, which has an excess of positive charges (holes) and an n-type material, which is electrically negative (electrons). P-type and n-type materials are linked through a silicon junction. When the sunlight

reaches the silicon junction, this absorbs the energy of the photons of the sunlight. The energy is transmitted to the electrons of the valence band in n-type material, causing their diffusion. Electrons will start to move from the n-type material to the p-type material, where there is an excess of positive charge. The movement of the electrons creates a net charge, producing electricity (Figure 19):

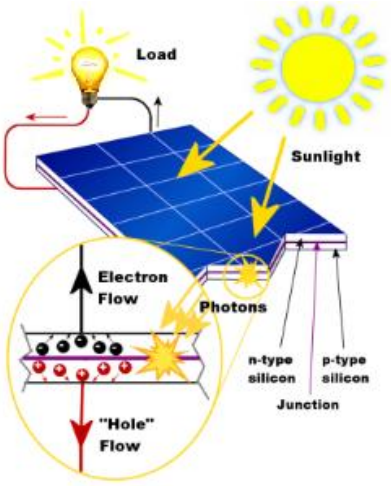

Figure 19: Schematic of the PV cell

Although solar light is commonly used by photovoltaic cells and a power density of 100 mW/cm^2 can be attained, indoor light from the illumination of the offices and buildings can be converted into electricity as well. However, the power density will decrease to 10-100μW/cm^2 [33].

Solar devices are frequently used at large-size as to the energy supply depends on the dimension of the photovoltaic cells. However, several solar harvesters for small- size devices have been developed. For instance, solar harvesters called "helimotes" are being developed at the University of California [31], not only to supply energy to the sensor nodes, but also charge their batteries.

Another very important aspect is that these harvesters can be combined with other harvesters, such as thermoelectric generators. The light is absorbed by a black surface, warming the bottom part of it. This part is used as the hot side in the thermoelectric harvester, increasing the temperature difference. With an ambient temperature of 34ºC, the PV cell reached 61ºC [40]. The power

generated by the thermoelectric increased because of the increase in the temperature at the hot side.

The advantages of the solar generators are:

- They are very well established
- Low cost
- Easy to implement to provide energy,
- No mobile parts are presented, hence, no noise appears and they are more reliable.
- Sunlight is an abundant source of energy and the longevity of the PV is quite long (several decades).

The main drawback is that sunlight is not always available. Thus, the scavenged energy from the light is not constant. For this reason, batteries to accumulate the energy or another source of energy are required for shortage periods.

2.5.2.3 Air flow energy

Wind turbines convert kinetic energy from the wind into electricity. Large-scale wind turbines can attain an efficiency of 50% [10]. However, when the miniaturization of wind generator is desirable, problems start to emerge. At small-scale, mobile parts have low efficiency, due to the large drag at low Reynolds numbers. Energy is also wasted on friction of the bearings.

The power obtained from air flow can be represented by equation (2-11):

$$P_{output} = \frac{1}{2} C_P \rho A U^3 \quad \textbf{(2-11)}$$

Where A is the area of the generator, ρ is the density of the air, C_P is the power coefficient. The power coefficient is always less than 1 and it has a maximum value (Betz limit) of 16/27= 0.593 [10].

Devices of several centimetres can produce enough energy to supply energy for a wireless sensor, from air-conditioning ducts, car engines and the environment. Several small-scale devices have been developed [10] but the most prominent for wireless sensors is shown in Figure 20. It can generate 1mW with a pressure drop of 8.4 mbar.

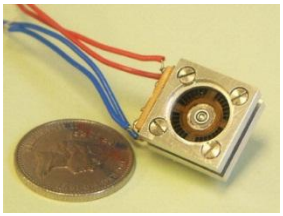

Figure 20: Air flow energy harvester compared to 10 pence coin [10]

Devices that have mobile parts at small-scale are not very reliable. They can be substituted by vibrating elements. Moreover, with the combination of piezoelectric materials, energy can be harvested. For instance, a piezoelectric cantilever can be used to obtain energy from the wind [41]. The vibrations required for the piezoelectric harvester are attained by the Karman's vortex street of the air flow. The vortex street produces an oscillating movement necessary for harvesting energy.

Another device (Microbelt) developed by Humdinger Wind Energy LLC is called is showing in Figure 21. The principle of the Microbelt is the phenomenon of aeroelastic flutter. The membrane is subjected to a flutter oscillation and produces energy via the piezoelectric effect.

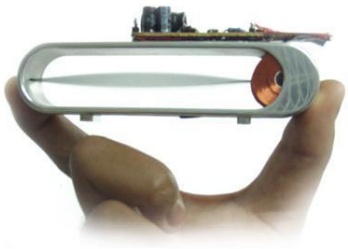

Figure 21: Microbelt (air flow harvester) [42]

2.5.2.4 Thermal energy

The basic principle of the thermal energy harvesters is to produce energy from temperature differences that can appear in the environment. Heat is present in many places, for instance, human or animal skin, vehicles, engines and structures.

In thermal energy harvesters, two parameters have to be taken into account: difference of temperature and heat flow.

Heat flow provides the power required, and the temperature difference determines the energy efficiency. As in every process where the temperature differences are involved, efficiency of conversion is limited by the Carnot efficiency (equation(2-12)

$$\eta_{carnot} = \frac{T_H - T_C}{T_H} \quad \textbf{(2-12)}$$

where T_H is the temperature of the hot side and T_C is the temperature of the cold side. The higher temperature of the hot side, the higher efficiency (see Figure 22)

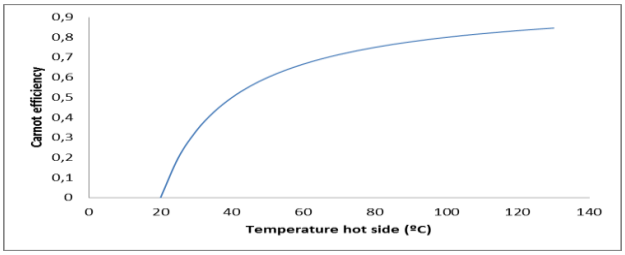

Figure 22: Variation of the Carnot efficiency with the temperature of the hot side (T_H). Temperature of the cold side is fixed (T_c=20ºC)

There are several kinds of thermal energy harvesting: thermionic, pyroelectric and thermoelectric energies.

Pyroelectric materials:

Pyroelectricity is created by a pyroelectric material when subjected to temperature fluctuations. In order to understand this phenomenon, how the atoms are located in the material has to be understood. (see section 2.5.2.1). In

the unit cell (smallest cells in the crystal) the average of the position of the positives and negatives charges does not coincide. Thus, dipoles appear. When a spontaneous change of temperature appears in these materials the atoms and dipoles start to move, creating an electric field. This means that pyroelectric materials need oscillation of temperature over time to generate the electric field.

Thermionic harvester:

Electricity in thermionic harvesters is produced by the temperature difference between two electrodes. Electrons are ejected from the hot electrode (anode) to the cold electrode (cathode) passing through a vacuum gap [40]. In order to produce the ejection, an energetic barrier has to be overcome (see Figure 23). When the thermionic harvester works as a generator ($T_1<T_2$), the energy of the electron has to be higher than the sum of μ_2 (electrochemical equilibrium potential (Fermi level at 0K)) V and W. μ_2+W+V is the energetic barrier and it is the minimum level of energy to be able create an electric field. V is the voltage between the anode and the cathode. W is the potential dependent on the work function of the material. W can be considered low in hetero-junctions or in junctions of p-n materials [43]

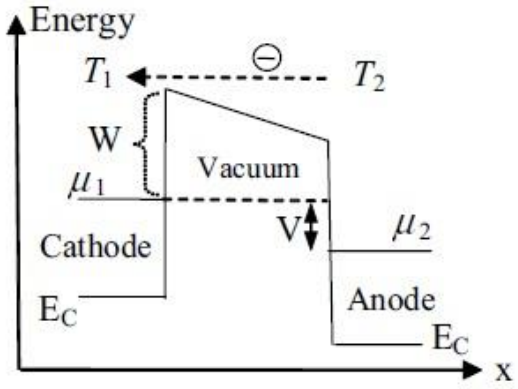

Figure 23: Schematic of energy levels required for thermionic electron emission [43]

This generator works effectively at high temperatures, more than 1500K [43], which is not suitable for many applications to provide energy to wireless sensors, due to the high temperatures. Although, the efficiencies attained are

higher than in thermoelectric harvesters. Thermionic generators were utilized in some space missions.

Thermoelectric generators:

Thermoelectric harvesters directly transform temperature difference into voltage by means of the Seebeck effect. They have been selected for this project and are described in greater detail in section.

2.6 Thermoelectric harvester

2.6.1 Description

Energy generated by a thermoelectric generator (TEG) is obtained by using thermopiles. Thermopiles are composed of several thermocouples, usually connected electrically in series and thermally in parallel [44]. As Figure 24 shows, many thermocouples are connected in series, but they are exposed at the same temperature difference ($T_{hotside}$-$T_{coldside}$), so thermally in parallel.

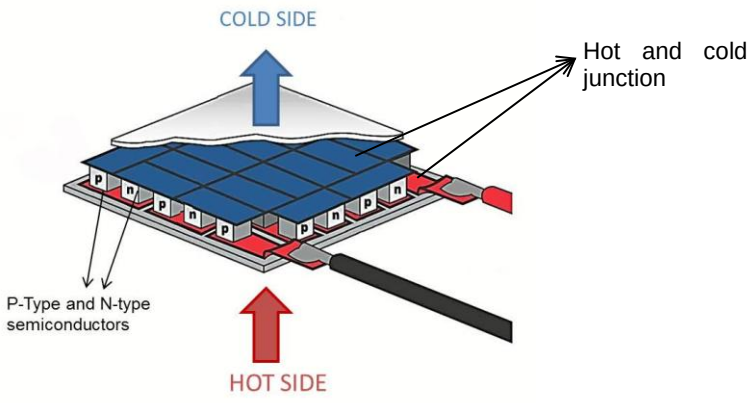

Figure 24: Schematic of a thermoelectric device [45]

The thermocouple consists of a p-type element, containing free “holes” (positive charges), because of its high energy level, and a n-type element that contains free electrons.

Thermoelectric working as an energy generator, a load is connected to the thermoelectric device (Figure 25). When the temperature of the hot side is

higher than the temperature of the cold side (heat sink), a temperature difference is present. As a result of this temperature difference, electrons from the hot end are excited and they begin to drift from the hotter side to the cooler end. This movement creates a net charge (negative for electrons and positive for the “holes”) in the cold side, producing voltage. The arrow in Figure 25 indicates the electric current direction, contrary to the electron movement.

It has to be noted that the temperature of the heat source is not the same temperature that exists at the hot junction of the n-type or p-type element (Figure 24) due to the presence of the ceramic that separates both sides. Ceramic is usually represented as a thermal resistance. The same phenomenon occurs in the cold side (heat sink).

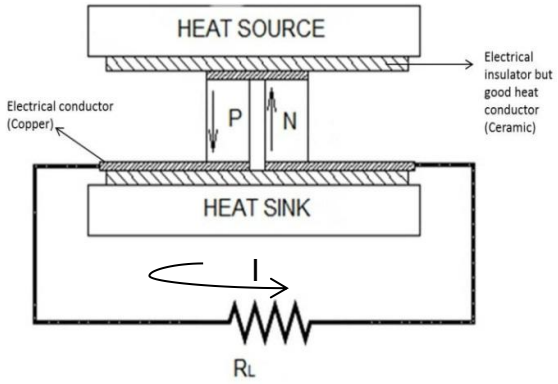

Figure 25: Thermoelectric device working as a generator (TEG)

Thermoelectric generators are based on the thermoelectric principles: “Seebeck effect” and “Peltier effect”.

2.6.2 Principles of thermoelectric harvesters

The first thermoelectric phenomenon explains how much voltage can be obtained from the temperature difference in a thermocouple. It is called **Seebeck effect**, as is given by equation (2-13):

$$\mathrm{V} = \alpha_{pn}\,\Delta T \qquad \textbf{(2-13)}$$

Where V is the voltage, $\alpha_{pn} = \alpha_p - \alpha_n$, being α the Seebeck coefficient of the material [V/K] for p-type and n-type respectively. ΔT is the temperature

difference between the hot junction and the hot junction (T_{hJ}-T_{CJ}). The Seebeck coefficient has a different value and sign for p-type and n-type materials. For p-type materials α is positive and negative in n-type materials. However, for calculations, it is usual to take the same value but different sign of p-type and n-type [45].

In thermoelectric harvesters, the temperatures difference generates potential difference. However, the electric current obtained also provides heat flow. This phenomenon is called **Peltier effect** (how much heat passes through a material for a given electrical current) as equation (2-14) shows:

$$\mathrm{Q} = \pi I \tag{2-14}$$

In which Q is the heat flow [W], I the current [A] and π is the Peltier coefficient [V].

In addition to these two effects (Seebeck and Peltier), another phenomenon was discovered by William **Thomson** or Lord Kelvin in 1851 [46]: Any current carried by a conductor also subject to a temperature difference absorbs or emits heat, depending on the material. The heat rate generated is proportional to the electrical current and also to the thermal gradient [47] :

$$\dot{q}_{thomson} = -\mu J \nabla T \tag{2-15}$$

Where $\dot{q}_{thomson}$ is the heat flux or the heat rate (although most of the time for simplicity the dot is omitted) due to the Thomson effect, J is the electrical current density that passes through a homogenous conductor and μ is the Thomson coefficient which can be expressed by equation (2-16):

$$\mu = T \frac{d\alpha}{dT} \tag{2-16}$$

In this equation α is Seebeck coefficient. Furthermore, Lord Kelvin discovered the relationship between Seebeck coefficient (α) and Peltier coefficient (π):

$$\pi = T\alpha \tag{2-17}$$

where T is the temperature of the material.

2.6.3 Power output and efficiency

Once the phenomena that occur in thermoelectric generators have been depicted, the electric current density ($\boldsymbol{j_{el}}$) and the heat flux ($\mathbf{q}$) (heat transfer rate per cross-sectional area) can be expressed as follows [48]:

$$\boldsymbol{j_{el}} = \sigma\mathbf{E} - \sigma\alpha\nabla\mathrm{T} \tag{2-18}$$

$$\mathbf{q} = \alpha\mathrm{T}\boldsymbol{j_{el}} - \kappa\nabla\mathrm{T} \tag{2-19}$$

Where σ is the electrical conductivity [$(\Omega m)^{-1}$], which is inversely proportional to the resistivity (ρ). α is the Seebeck coefficient [V/K], T the mean temperature [K], κ the thermal conductivity of the material [$\frac{W}{mK}$] and $\mathbf{E}$ the electric field [V/m].

The equations above can be simplified (see equation (2-20) and (2-21)) if the below conditions are imposed:

- α, σ and π are independent of the temperature.
- Steady-state conditions are assumed.
- The conservation of the energy and charge is used [46] .

$$\nabla \cdot \boldsymbol{j_{el}} = 0 \tag{2-20}$$

$$\nabla \cdot \mathbf{q} = \boldsymbol{j}_{\mathbf{el}} \cdot \mathbf{E} \tag{2-21}$$

From equation (2-20), if a one-dimensional model is chosen, it is deduced that $\boldsymbol{j}_{\mathbf{el}} = J\ \mathbf{e_x}$. $\mathbf{e_x}$ is the direction of the current from the hot side to the cold side through a constant cross sectional area A_c.

With the result obtained above and substituting equation (2-18), equation (2-22) is obtained:

$$\mathbf{E} = \left(\frac{J}{\sigma} + \alpha\frac{\partial T}{\partial x}\right)\boldsymbol{e_x} \tag{2-22}$$

combining equations (2-18), (2-21), (2-22) and with the simplifications defined previously, the equation (2-23) is attained:

$$-\kappa \frac{\partial^2 T}{\partial x^2} = \frac{J^2}{\sigma} \quad \textbf{(2-23)}$$

Thus, the temperature profile is parabolic, given by equation (2-24):

$$\mathrm{T(x)} = \frac{A}{2}x^2 + Bx + C \quad \textbf{(2-24)}$$

with $A = -\frac{J^2}{\sigma\kappa}$. The necessary boundary conditions to determine B and C for the thermoelectric device are temperature at the hot and the cold junction:

$$\mathrm{T}(0) = T_{hj}; \quad T(L) = T_{cj} \quad \textbf{(2-25)}$$

where L is the leg length of the material p or n (Figure 26).

Finally, the profile of the temperature in the junction is known. $\Delta T = T_{hj} - T_{cj}$, temperature difference between the hot and the cold junction:

$$T = \frac{J^2}{2\sigma\kappa}x^2 - \left(\frac{\Delta T}{L} - \frac{J^2}{2\sigma\kappa}\right)x - T_{hj} \quad \textbf{(2-26)}$$

In order to determine the heat flow absorbed by the hot side (Q_h) and the thermal power dissipated by the cold side (Q_c), eq. (2-19) and (2-26) are required. Given that the heat flow is $Q = q \cdot A_C$, assuming that heat flux is constant in the transversal area and I is the electrical current through the material ($I = J \cdot A_C$), the heat flow in the cold and in the hot junction can be expressed by:

$$Q_h = \alpha T_{hj} I + \frac{\kappa}{L}A_c \Delta T_j - \frac{I^2 L}{2\sigma A_c} \quad \textbf{(2-27)}$$

$$Q_c = \alpha T_{cj} I + \frac{\kappa}{L}A_c \Delta T_j + \frac{I^2 L}{2\sigma A_c} \quad \textbf{(2-28)}$$

In these equations the thermal conductance of the material p or n is $K_m = \frac{\kappa}{L}A_c$ and the internal resistance of the material p or n is $R_m = \frac{L}{\sigma A_c}$. A schematic of the p type material operation is shown in Figure 26.

The electrical **power attained** (P_{output} in equation (2-29)) in a thermoelectric material is the difference between the heat flow absorbed and the heat flow dissipated. Using equations (2-27) and (2-28) equation (2-29) is given. Where $\Delta T = T_{hj} - T_{cj}$.

$$P_{output} = Q_h - Q_c = \alpha I \Delta T - \frac{I^2 L}{\sigma A_c} \quad \textbf{(2-29)}$$

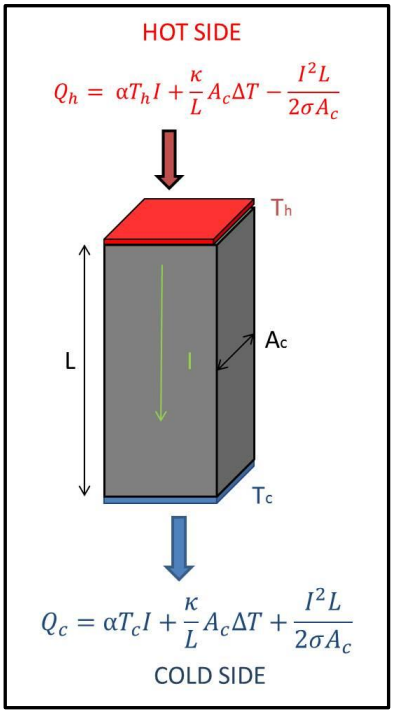

Figure 26: Schematic of p-type element

The **efficiency** of the TEG is the relation between the output power and the input thermal power which is the heat flow from the hot side (see equation (2-30))

$$\eta = \frac{P_{output}}{Q_h} = \eta_{carnot} \cdot \eta_r \quad \textbf{(2-30)}$$

with η_{carnot}, the Carnot efficiency and η_r the reduced efficiency. From equations (2-12), (2-27), (2-28) and (2-29), the reduced efficiency is deduced as equation (2-31) shows:

$$\eta_r = \frac{1 - \frac{L}{\sigma A_c}\frac{I}{\alpha \Delta T}}{1 + \kappa \frac{A_c}{L}\frac{\Delta T}{\alpha T_h I} - \frac{IL}{2\sigma A_c \alpha T_h}} \quad \textbf{(2-31)}$$

The equation above refers to one type of leg (n or p material) of the thermocouple. For thermocouples connected electrically in series and thermally in parallel, the total efficiency can be calculated as [47]:

$$\eta_{np} = \frac{\eta_p Q_{hp} + \eta_n Q_{hn}}{Q_{hp} + Q_{hn}} \quad \textbf{(2-32)}$$

where subscript p is for the p-type material and n is for the n-type material.

The equations depicted above are referred to one type of material. However, the thermoelectric harvester is composed of several thermocouples (p and n type material) connected thermally in parallel and electrically in series. Thus, the equations will be modified as equations (2-33) (2-34) and (2-35) show:

$$V_{th} = N(\alpha_p - \alpha_n)\Delta T \quad \textbf{(2-33)}$$

$$R_{th} = 2N\frac{L}{\sigma A_c} \quad \textbf{(2-34)}$$

$$K_{th} = 2N\frac{kA_c}{L} \quad \textbf{(2-35)}$$

with N the number of thermocouples in the thermoelectric device, $\alpha_p - \alpha_n$ the Seebeck coefficient, ΔT the temperature difference, R_{th} and $V_{th}$the internal resistance of the thermoelectric device and the voltage generated by the thermoelectric device respectively. K_{th} the thermal conductance of the thermoelectric generator, L length of the leg of the thermocouples of the thermoelectric generator and σ and k, the electrical conductivity and k the thermal conductivity of the material respectively.

When a thermoelectric generator (TEG) is to be utilized as power source for another device, such as a wireless sensor node, it can be represented as a

resistance (R_L), (Figure 25). The voltage in the load (V_L) and the current of the circuit (I) are shown in equations (2-36) and (2-37):

$$V_L = V_{th}\frac{R_L}{R_{th}+R_L} \tag{2-36}$$

$$I = \frac{V_{th}}{R_{th}+R_L} \tag{2-37}$$

Then, by calling $M = \frac{R_L}{R_{th}}$, the output power (P_{output}) due to the load (R_L) will be obtained as equation (2-38) shows:

$$P_{output} = V_L I = \frac{V_{th}^2}{R_{th}}\frac{M}{(M+1)^2} \tag{2-38}$$

With V_{th} the voltage generated by the thermoelectric and R_{th} the internal resistance of the thermoelectric.

Using (2-30), (2-31) and (2-34), the efficiency of the thermoelectric device (η) is depicted in (2-39):

$$\eta = \frac{\Delta T}{T_h}\frac{M}{M+1+\frac{(M+1)^2}{ZT_h}-\frac{1}{2}\frac{\Delta T}{T_h}} \tag{2-39}$$

Where η_{carnot} is the first term of the equation (2-39) and the second term is $\eta_{r.}$ $Z = \frac{\alpha^2}{R_{th}K_{th}}$ in equation (2-39) is the figure of merit of the TEG with dimensions. The figure of merit is an indicator of the performance of the thermoelectric device.

By deriving the efficiency and output power with respect to M, the maximum efficiency (η_{max}) and maximum output power ($P_{outputmax}$) can be obtained as equations (2-40) and (2-41) show:

$$\eta_{max} = \frac{\Delta T}{T_h}\frac{\sqrt{1+ZT_m}-1}{\sqrt{1+ZT_m}+\frac{T_c}{T_h}} \tag{2-40}$$

$$P_{outputmax} = \frac{V_{th}^2}{4R_{th}} \quad \textbf{(2-41)}$$

With $T_m = \frac{T_c+T_h}{2}$, $\Delta T = T_h + T_c$ the temperature difference between the hot side (T_h) and the cold side of the thermoelectric (T_h) of the thermoelectric device. Z the figure of merit of the thermoelectric generator, V_{th} the voltage provided by the thermoelectric device and R_{th} the internal resistance of the thermoelectric module.

The values of M for maximum efficiency and for maximum power respectively are: $M_\eta = \sqrt{1 + ZT_m}$ and $M_p = 1$. These two values are different, but in order to attain the optimum design of the TEG, the maximum efficiency will be considered. The parameter Z is related to the characteristics of the material. But, in order to obtain the maximum power, two parameters are involved: the load resistance connected (R_{th}) to the TEG and the physical characteristics of the legs.

2.6.4 Parameters of the TEG manufacturing

By having depicted the phenomena and the equations of the TEG, the considerations for manufacturing a thermoelectric device are described in this section. The ambient conditions, the material of the thermocouples and the dimension of the thermocouples are the most important parameters

1. **Ambient conditions**

As mentioned above, Carnot efficiency (equations (2-42) and (2-43)) has the main role in processes where temperature differences are involved, for instance in thermoelectric harvesters.

$$\eta = \eta_{carnot} \cdot \eta_r \quad \textbf{(2-42)}$$

$$\eta_{carnot} = \frac{T_H - T_C}{T_H} \quad \textbf{(2-43)}$$

Considering that the highest temperature (T_H) that can be achieved is fixed, in a warmer environment, the Carnot efficiency decreases, likewise, in a colder ambient, Carnot efficiency increases. This is due to the temperature difference is lower and higher respectively. Therefore, the location of the thermoelectric generator has to be taken into account.

2. Materials

The target, since the thermoelectric materials were discovered, is to attain the highest thermoelectric efficiency. The earliest designs had very low efficiency and they were too expensive. Nevertheless, nowadays, high-efficiency materials can be achieved with the use of complex materials [49].

In order to determine the efficiency of a thermoelectric harvester, the dimensionless figure of merit (ZT) of the TEG has to be maximized. It must be clarified that ZT is the figure of merit of the TEG, not the figure of merit of the material (zT) (equation (2-44)). For the maximum efficiency, the figure of merit of the material must be the figure of merit of the device to optimize its operation, although this is a complicated issue [49].

$$zT = \frac{\alpha^2 T \sigma}{\kappa} \quad \textbf{(2-44)}$$

In this dimensionless equation, α is the Seebeck coefficient, T the temperature of the material, σ the electrical conductivity and κ thermal conductivity. To attain the maximum figure of merit of the material, low thermal conductivity, high electrical conductivity and high Seebeck coefficient are needed.

The Seebeck coefficient (α) can be expressed by the equation (2-45) for metals and semiconductors [49]:

$$\alpha = \frac{8\pi^2 k_B^2}{3eh^2} m^* T \left(\frac{\pi}{3n}\right)^{2/3} \quad \textbf{(2-45)}$$

This equation depends generally on n, that is the carrier concentration, and m^*, that is the effective mass of the carrier. The lower the carrier concentration (the

lower is chemical potential), the higher the Seebeck effect. However, electrical conductivity increases with n (equation (2-46)):

$$\sigma = ne\mu \quad \textbf{(2-46)}$$

where μ is the carrier mobility. Thus, an optimum value of the carrier concentration has to be obtained to satisfy a maximum efficiency. This value of n is achieved between 10^{19} and 10^{21} per cm^3 [49] and it can be encountered in doped semiconductors.

Moreover, if the effective mass of the carrier m^* is higher (i.e. heavy carriers), the carrier mobility decreases as does the electrical conductivity. Newly, a compromise is shown between Seebeck coefficient and electrical conductivity. Although for the value of n, a range of values is found as an optimum, in the case of m^*, it is not easy to find. Thermoelectric materials as conductors (oxides) have high m^*, and thermoelectric materials as semiconductors (GaAs, SiGe) have high mobility and low m^*,.

In reference to κ (thermal conductivity), two sources of heat have to be taken into account. The first one is when electrons and positive charges (holes) are moving, they transport heat. The second source is the movement of the phonon through the lattice. Phonons are the sinusoidal disturbance in the position of the atoms. When the temperature increases the vibrations of the atoms grow and the number of the phonons increase. The lattice refers to the position of the atoms themselves.

Thermal conductivity can be represented as equation (2-47):

$$\kappa = \kappa_e + \kappa_1 \quad \textbf{(2-47)}$$

κ_e is the thermal conductivity provided by the free electrons, and κ_1 (lattice component) is provided by the movement of the phonons. On the other hand, κ_e can be expressed as equation (2-48):

$$\kappa_e = L^* \sigma T \quad \textbf{(2-48)}$$

In which equation L^* is the Lorenz factor (2.4 10^{-8} $\frac{J^2}{K^2C^2}$) [49] for free electrons.

For materials with high electrical conductivity, the thermal conductivity, due to the free electrons, is also elevated. Thus, κ_1 must be low, in order to achieve the best compromise between thermal and electrical conductivity to achieve higher figure of merit (zT). Although glasses have a low thermal energy provided by the phonons, the electrical conductivity is much more reduced. So, the materials that best suit with the characteristic of the thermoelectric harvesters are crystalline semiconductors, such as SiGe, Bi_2Te_3 and PbTe.

Material compatibility

If high values of figure of merit of the material are achieved, high efficiency should be attained. However, another factor, thermoelectric compatibility, has to be taken into consideration [50]. This means that when two materials are in contact, incompatibility between these two can occur, and their optimum behaviour may not coincide with their single average behaviour.

By taking a look into the reduced efficiency, see (2-31), considering the geometry of the thermoelectric device ($\frac{A_c}{L}$) is fixed, equating heat conduction (Q_{con}) to $\kappa \Delta T \frac{A_c}{L}$ and introducing the figure of merit with dimensions z, the reduced efficiency can be written as equation (2-49):

$$\eta_r = \frac{\frac{I}{Q_{con}}\frac{\kappa}{\alpha\sigma}\left(1-\frac{I}{Q_{con}}\frac{\kappa}{\alpha\sigma}\right)}{\frac{I}{Q_{con}}\frac{\kappa}{\alpha\sigma}\left(1-\frac{I}{Q_{con}}\frac{\kappa}{\alpha\sigma}\frac{\Delta T}{2T_h}\right)+\frac{1}{zT_h}} \quad \textbf{(2-49)}$$

If ΔT is very small compared to T_h and $u = \frac{I}{Q_{con}}$ (relative current density) the equation above is reduced to equation (2-50):

$$\eta_r = \frac{u\frac{\kappa}{\alpha\sigma}\left(1-u\frac{\kappa}{\alpha\sigma}\right)}{u\frac{\kappa}{\alpha\sigma}+\frac{1}{zT_h}} \quad \textbf{(2-50)}$$

In this equation the dimension of the thermoelectric device leg does not appear. In the leg of the thermoelectric harvester, "u" is almost constant. Each leg can be composed of one material or different materials, but they are usually connected electrically and thermally in series (segmented materials).

The thermoelectric compatibility factor is the value of u that maximizes the reduced efficiency and it is called "s" and it does not depend on the geometry of the leg (equation (2-51)):

$$u_\eta = s = \frac{\sqrt{1+zT} \pm 1}{\alpha T} \quad \textbf{(2-51)}$$

In the equation (2-51), the negative sign is for thermoelectric device that generates power and the positive sign is for cooling [49].

If the material is working at a determinate temperature and with a determinate value of u, and this value of u is totally different from the value of s, this will mean that the material does not convert the heat into electricity in an effective way.

In segmented materials (electrically and thermally in series), the value of s has to be as close as possible in the materials (not more than two order of magnitude difference) to be compatible. For example, in Table 4, SiGe will be clearly incompatible with any other p or n type materials. Nevertheless, the temperature range must also be taken into consideration, due to their behaviour changes with the temperature.

At low temperatures BiSb, is used for n-type and $(BiSb)_2$ $(TeSe)_3$ for p-type. Most of thermoelectric materials used nowadays at room temperature are Bi_2Te_3 and Sb_2Te_3. Nevertheless, p-type and n-type materials are different from each other. For temperatures between 500-900K PbTe, GeTe and SnTe are commonly utilized. Finally, for high temperatures silicon-germanium alloys are used [49].

Table 4: Values of s for different materials for n-type and p-type [50]

	Material	T_c(K)	T_h(K)	s
P-Type	Bi_2Te_3	300	451	2.900
	Zn_4Sb_3	451	677	2.119
	$CeFe_4Sb_{12}$	677	973	1.558
	SiGe	973	1300	0.4116
N-Type	Bi_2Te_3	300	433	1.624
	PbTe	433	728	1.374
	$CoSb_3$	728	973	1.093
	SiGe	973	1300	0.6603

3. **Dimension of the thermopiles**.

The maximum efficiency is optimized by the characteristics of the material; however, the output power is going to be optimized by the dimension of the TEG. The maximum output power is given by equation (2-52):

$$P_{outputmax} = \frac{A_c \sigma}{L} \frac{N^2 \alpha^2 \Delta T^2}{4} \quad \textbf{(2-52)}$$

It can be seen that the maximum power obtained is directly proportional to the square of the voltage ($V_{th} = \alpha \Delta T$) and the ratio $\frac{A_c}{L}$. The voltage depends on the number of thermocouples that are connected in series, so by increasing the number of thermocouples the output power will rise. In reference to the ratio $\frac{A_c}{L}$, large areas and short length of the legs are required. However, miniaturized devices are the goal to provide electricity to small-size sensors, thus, the optimum ratio $\frac{A_c}{L}$ must be achieved. For bulk materials lengths of legs can be tens of millimetres [44] and according to the literature, for thin materials, thickness of several of tens μm can be reached [45]. With a size smaller than 10 μm, it is difficult to obtain good results.

2.7 Selection of the energy harvester

In order to supply energy from the environment, different types of energy are considered: Mechanical, solar, air flow and thermal. Obviously, there is no sunlight and the air flow inside the nacelle is too low. In addition, mobile parts are not reliable in this situation.

Mechanical and thermal harvesters are the most suitable for this application, due to the presence of vibrations and temperature differences in the nacelle. In relation to the mechanical harvesters, the drawbacks of each one are going to be analysed. Piezoelectric materials are highly brittle and they can fail due to fatigue. In the case of electrostatic generators, another source of voltage is needed to charge the capacitor. Eventually, inductive systems are very complicated to construct (many small parts have to be assembled). In this case robust materials, simply construction and minimum maintenance are necessary due to the location of the turbines. Thus, mechanical harvesters are not suitable for this application.

Parts of the tidal turbines such as generator, gearbox or the blade can achieve different temperature levels relative to the ambient temperature, generating a temperature difference. Hence, it seems to be that thermal harvesters are the perfect ones for this purpose. However, thermionic generators work at very high temperatures (1500K) and in the nacelle, this temperature is not achievable. Pyroelectric generators need temperature changes, which are not characteristic of these parts.

Finally, thermoelectric generators can take advantage of these temperature differences to generate electricity. Despite their drawbacks, thermoelectric devices are ideal candidates as an energy source for sensors inside the nacelle of tidal turbines. They have the advantages described below:

- They have no moving parts. Moving parts are complicated to design and work for devices at small scale.
- Silent, reliable and robust.

- Ideal to construct in small-scale caused by its simple construction, so, to supply sensors in condition monitoring are suitable.
- Temperature differences are readily available in the environment (generator, gearbox…)
- Low price.

These are the drawbacks as well:

- Efficiency of the harvester is limited by the Carnot efficiency (equation (2-12)). The efficiency attained is not very high.
- At meso-scale, the temperature differences tend to be smaller, so less energy could be supplied.

Supplied energy depends on the thermal resistance of the heat source and the sink.

2.8 Summary

In this section, the first objective of the project is presented. Firstly, the distribution of the sensors and its power consumption in the tidal turbine were discussed. Subsequently, the review of different small-scale energy harvesters and the types of wireless communication were reviewed.

In section 2.3.2, Table 1 depicts different sensors placed in a DeltaStream tidal turbine. These sensors are located on all the components of the tidal turbine, such as generator, gearbox, pintle, nacelle, hydraulic system and structure. The structure of the unit is shared by three turbines, thus, the number of sensors, in the whole unit, is approximately 200. Most of the sensors are located inside the nacelle, where the gearbox and generator are placed. The power consumption of the sensors goes from 500μW at 3V in accelerometers to several Watts in leakage sensors. All the sensors and auxiliary systems are connected via cable to an auxiliary transformer using power from the shore to supply power to them. Likewise, the communication is performed by means of cables.

Section 2.4 studies wireless sensor communication as a substitute to wired communication. Thus, land communication protocols and underwater communications protocols are studied. Land protocols can be separated in long range distance and short range distance (Table 2). Within the short range protocols, there are protocols such as Zigbee, Bluetooth or Enocean, that besides, they consume low power. However, in underwater communication, acoustic waves are used, mainly, because electromagnetic waves are dissipated in water and the communication is restricted to a few centimetres. For very long distance underwater communication acoustic transmitters are extremely expensive and they have high power consumption. Nevertheless, for short distance, on the order of tens of meters, the power consumption and the cost can be reduced.

Hence, communication between sensors from the tidal turbine to shore will be established as follows: Inside the nacelle, where there is no water present, the communication will use a land protocol. It is the communication between the sensor and one or two gateways, depending of the number of sensors. The gateway, inside the nacelle, will transmit the data to an acoustic transceiver. The transceiver will send the information to a platform receiver on the sea surface by means of acoustic waves. From the acoustic receiver in the platform, the information will be sent (by wires) to a transceiver that will sent the data via Wi-Fi, GPS, GPRS to land. This will permit to not only have the information at the shore base station, but also in others locations.

By regarding all the communications, this project is going to focus on the communication inside the nacelle using a land protocol (Zigbee) with low power consumption.

Finally, the energy harvester selected for this application is the thermoelectric generator, using the waste heat to supply energy to the sensors located in the nacelle. See section 2.7.

3 STUDY OF A THERMOELECTRIC GENERATOR

3.1 Introduction

In section 2.7, it was concluded that the thermoelectric device is the most suitable small-scale energy harvester to power the sensors inside the nacelle. For this reason, the behaviour of a real thermoelectric generator is analysed. In order to study the range of use of the thermoelectric harvester, the temperature of the different components of the tidal turbine is analysed, along with the temperature of the environment where they are located. In the second part of this section the power capabilities of a commercial thermoelectric generator are studied.

3.2 Temperature of the turbine components and environment

In order to determine how much power can be extracted from the environment through the thermoelectric generators, the available temperature differentials have to be estimated.

The tidal turbine used for this study is located in Ramsey Sound (Pembrokeshire) in Wales. The temperature profile of the sea is shown in Figure 28a:

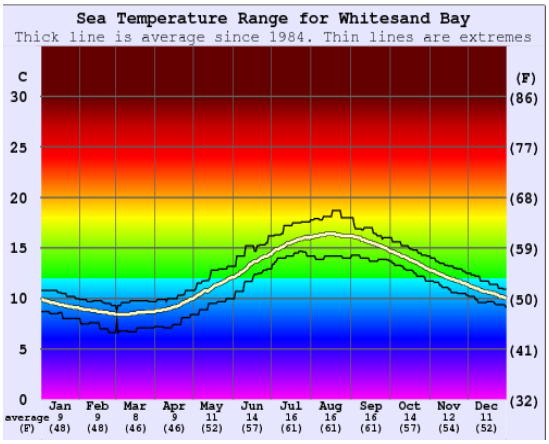

Figure 28a: Profile temperature in Ramsey Sound [74]

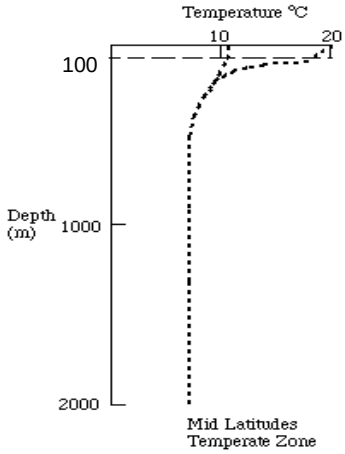

Figure 28b: Variation of the sea temperature with the depth

The sea surface temperature, where the turbines are placed, varies from 8ºC in February to 17ºC in August. Furthermore, temperature of the sea is dependent on the depth, for mid latitude oceans (Figure 28b).

The DeltaStream tidal turbine will be situated at a depth of 31.5 meters [7] below the sea level. Thus, the temperature will still be similar to the surface temperature according to Figure 28b.

Temperatures of the different “hot” components of a wind turbine are shown in Table 5. For tidal turbines, similar values are expected as the components are similar in construction and operation.

Table 5: Typical temperatures found in the different components of wind turbines

Parts	**Temperature (^{0}C)**		
	T_{min} (ºC)	**T_{max} (ºC)**	**T_{mean} (ºC)**
Generator			
Bearing driven end	4	78	41
Bearing not driven end	8	85	46.5
Windings	50	90	70
Gearbox			
Oil	15	50	32.5
Shaft bearing	7	66	36.5

Minimum and maximum temperatures achieved in each element depend on the ambient temperature. Higher temperatures will be reached in summer and lower temperatures in winter. Figure 29 shows a schematic of the nacelle of the turbine and the different sensors located in the turbine.

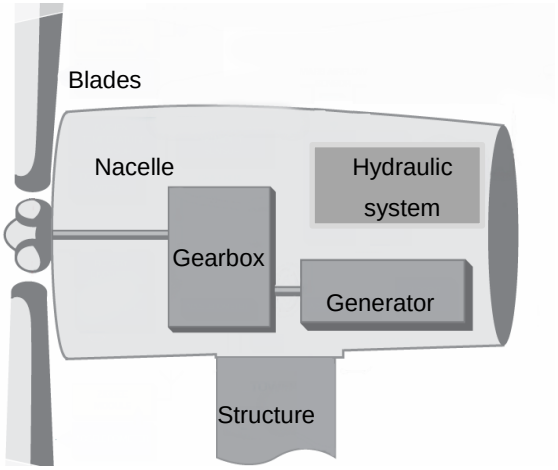

Location	Sensors
Blades	Strain gauge
	Accelerometer
Gearbox	Acceleration sensor
	Aqua sensor
	Torque sensor
	Metallic contamination senor
	Speed sensor
Generator	Temperature sensor
	Current sensor
Hydraulic system	Pressure sensor
	Linear transducer
Nacelle	Leakage sensor
Structure	Strain gauges
	Passive acoustics
	CCTV
	ADCP (Acoustic Doppler current profile)

Figure 29: Schematic of the tidal turbine nacelle and list of sensors in each component

By considering the data shown in Table 5 and by observing (Figure 29) that most of the sensors are located in the gearbox, the best position to place the thermoelectric device would be on the gearbox case or the generator case where highest temperatures are found. The bottom part of the gearbox will exhibit higher temperatures because of the contact of the case with the hot oil inside. In the generator, the casing close to the windings will reach the maximum temperature. Thus, these two locations would be ideal places to locate the thermoelectric generator.

3.3 Power harvesting capabilities of a thermoelectric device

3.3.1 Method

Once the locations of the thermoelectric generator are defined and the principles, the amount of power to be extracted can be determined. A conventional commercial thermoelectric device “ET-127-14-11-RS” was chosen, and the characteristics provided by the manufacturer are shown in Figure 30.

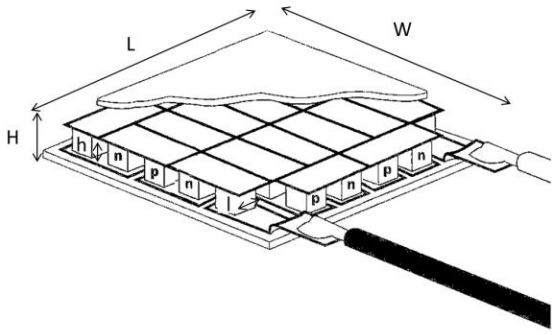

ET-127-14-11-RS	
N.Couples	127
L (mm)	40
W (mm)	40
H (mm)	3.8
l (mm)	1.4
h (mm)	1.1

Figure 30: Schematic of the thermoelectric device and table of characteristics of the thermoelectric generator used [51].

After the thermoelectric device is selected, two experiments were carried out. The first experiment consisted of measuring the voltage generated by the thermoelectric device when the hot side was heated to different temperatures. In the latter, with the aim of determining the maximum power achieved, a potentiometer was connected to the thermoelectric generator and the voltage and the current were measured under different load conditions.

3.3.1.1 Equipment

The equipment used to carry out the experiments included:

- A hot plate with a thermostat to control the temperature of the hot side.
- A K-type thermocouple connected to a thermometer (RS13-14 Thermometer) in order to measure the temperature of the cold side.
- A multimeter “Agilent 34401a” [51]. It was used to measure the voltage of the thermoelectric generator and across the potentiometer.

3.3.1.2 Procedure

The hot side of the thermoelectric device was placed on a temperature controlled hot plate. The temperature of the cold side was not controlled, but a heat sink was utilized to keep the cold side as cold as possible. The heat sink used was a copper plate attached to four tubes of copper and plastic with water inside with the aim of refrigeration (Figure 31). If a heat sink was not used, the

heat flow, created by the hot plate, would also heat the cold side of the thermoelectric generator. Consequently, the temperature of the cold side would be very similar to the temperature of the hot side, thus, no temperature difference would be achieved and no power would be generated.

Figure 31: Heat sink used to dissipate heat from the cold side of the thermoelectric device during trials.

A thermocouple was used to measure the temperature at the cold side (see 3.3.1.1). A non-silicone conducting paste that permits the heat transfer was placed between the thermoelectric device surfaces, the heat sink surface and the hot plate.

Once the thermoelectric generator was mounted, the two experiments were carried out:

1. Measurement of the voltage across the thermoelectric generator (open circuit conditions) for different temperature differences. To determine the maximum voltage generated by the thermoelectric generator.
2. Measurement of the voltage across a potentiometer, whose maximum nominal value is 15Ω, connected to the thermoelectric device. The aim of this second experiment was to determine the maximum power achieved by the thermoelectric harvester.

   The temperatures of the hot side selected were the different temperatures reached in each part of the turbine [32ºC, 37ºC, 41ºC, 47ºC, 50ºC, 66ºC,78ºC] (Table 5). When the temperature of the cold side was steady, the resistance of the potentiometer was varied [0.8Ω, 3.3 Ω, 5.7 Ω, 7.9 Ω, 10.6 Ω, 13.3 Ω, 15.4 Ω] and the voltage was measured.

With this measurement the current and the power generated by the thermoelectric device was calculated.

3.3.2 Results and discussion

As the temperature of the cold side was not controlled, the temperature that the cold side achieved was dependent on the hot side temperature. Moreover, it also depended on the ambient temperature. The temperatures of the hot and the cold side, at steady state, with the heat sink in place, are depicted in Figure 32.

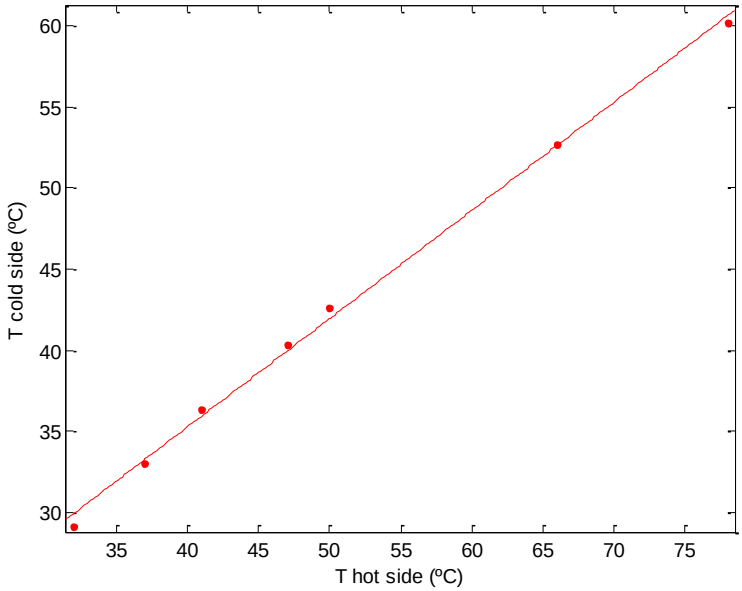

Figure 32: Variation of the temperature of the cold side with the temperature of the hot side of the thermoelectric device (Tamb= 20.9 ºC).

<u>Experiment 1: Open circuit conditions (thermoelectric device without load connected):</u>

Figure 33 shows the variation of the voltage generated by the thermoelectric device as while the temperature difference is varied. As seen in section 2.6.2, the output voltage (V_{th}) of the thermoelectric generator under open circuit conditions is a function of temperature difference (ΔT). By studying the equation (3-1), see below, and the data represented in Figure 33, where $V_{th} = 31.33 \cdot \Delta T$,

$\alpha_{pn} = (\alpha_p - \alpha_n)$ can be obtained using linear regression. If N (number of couples) is 127, the value of α_{pn} is 243.9 $\mu V/K$.

$$V_{th} = N(\alpha_p - \alpha_n)\Delta T \quad \textbf{(3-1)}$$

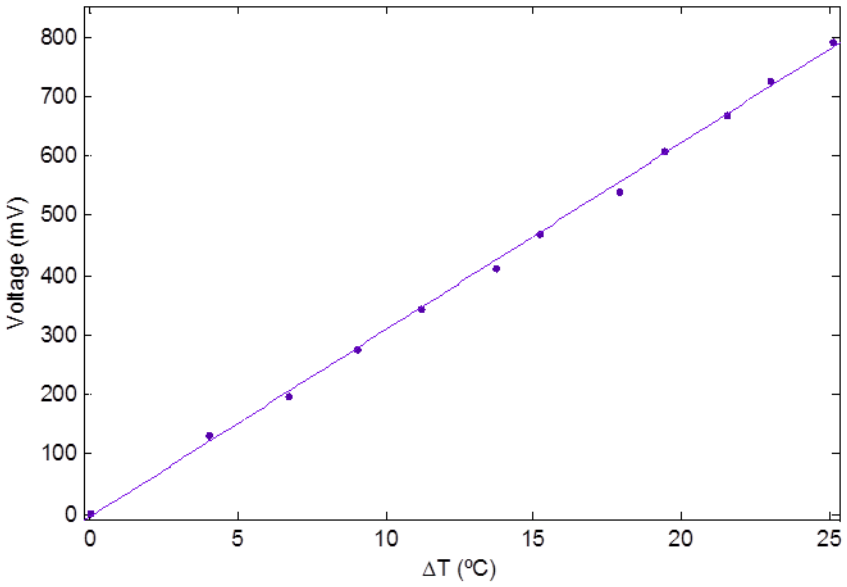

Figure 33: Voltage as a function of the temperature difference under open circuit conditions for a thermoelectric generator (Tamb=20ºC)

The maximum voltage attained using the thermoelectric device "ET-127-14-11-RS" was 784mV at a temperature difference of 25ºC.

Experiment 2: Potentiometer and thermoelectric generator

The voltage and current generated for different values of load are shown in Figure 34 and Figure 35. A table of the results is detailed in Appendix A.

Each line of the graph represents the voltage and the current for each temperature difference measured. The temperatures of the hot side selected were set at 32ºC, 37ºC, 41 ºC, 47ºC, 50ºC, 66ºC and 78ºC. Temperatures at the cold side, using the heat sink described above, are not controlled. Thereby, the temperatures measured at the cold side are shown in Figure 32 and also in Appendix A.

In Figure 34, it can be observed that the voltage follows the behaviour described by equation (3-2).

$$V_L = V_{th}\frac{R_L}{R_{th} + R_L} \quad \textbf{(3-2)}$$

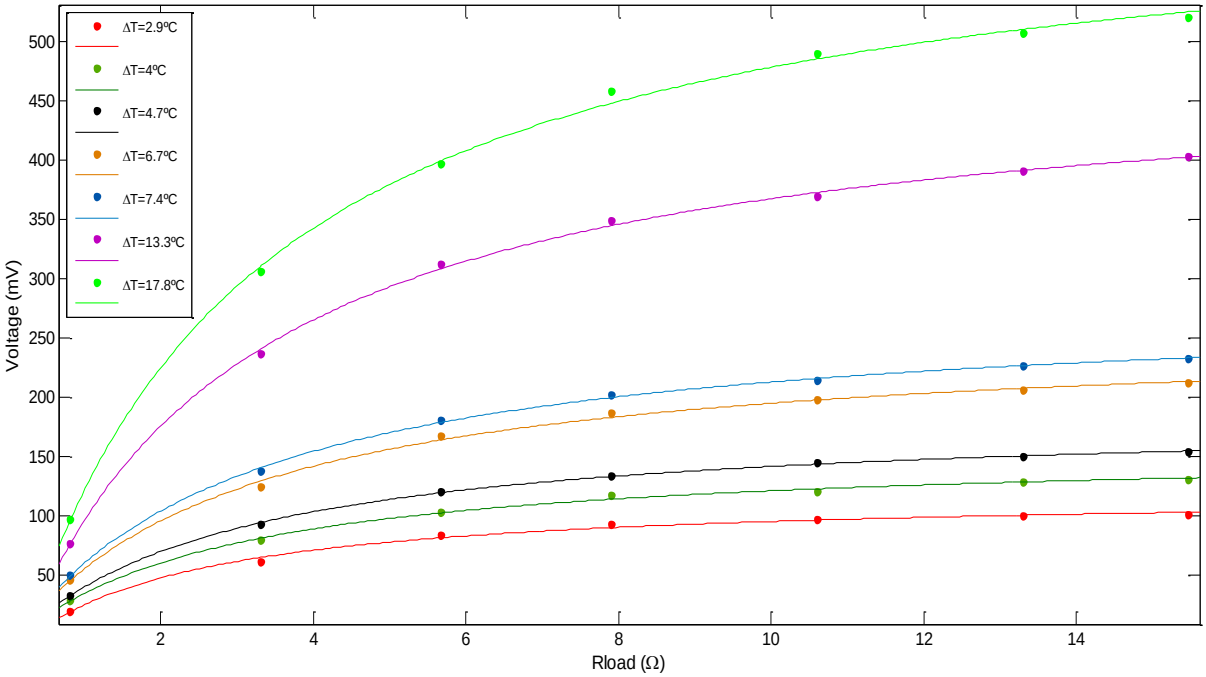

Figure 34: Voltage generated by the TEG as a function of load resistance and temperature difference

When the load connected is higher the voltage obtained is also higher. As the voltage with the load connected is directly proportional to the theoretical voltage generated by the thermoelectric device (V_{th}) and V_{th} is proportional to the temperature difference (ΔT), the voltage will increase when the temperature difference rises.

From equation (3-3) and Figure 35, current is inversely proportional to the load connected and proportional to the temperature difference. The higher the temperature, the higher the current and the voltage.

$$I = \frac{V_{th}}{R_{th} + R_L} \quad \textbf{(3-3)}$$

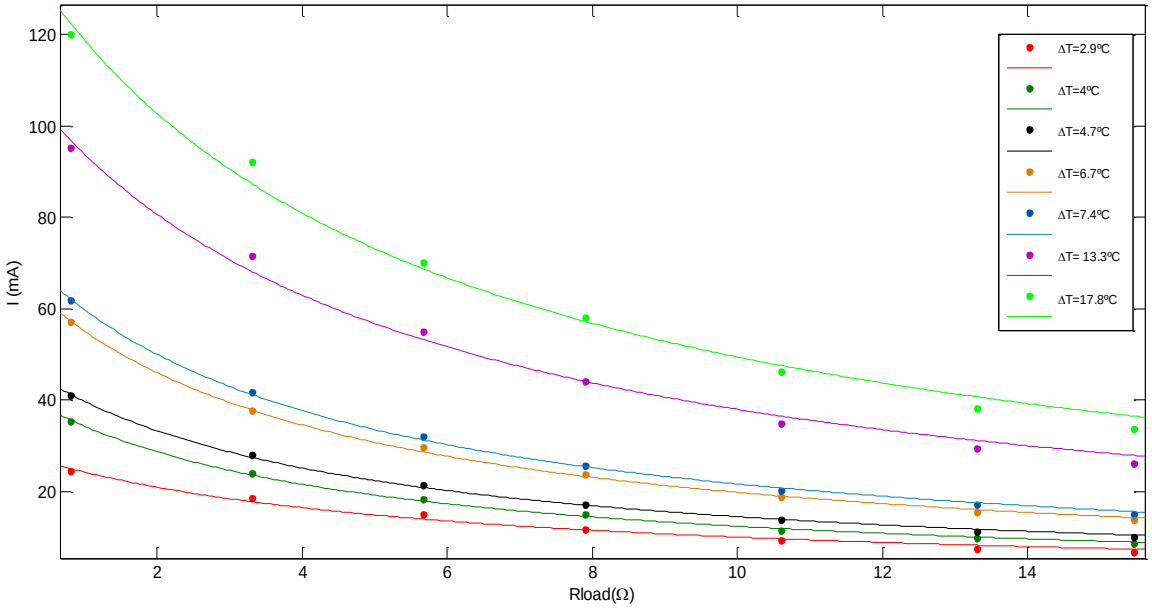

Figure 35: Current generated by the TEG as a function of load resistance and temperature difference.

As the figures show, a maximum voltage of 520mV at 15 Ω and maximum current of 120 mA at 0.81Ω were attained for a ΔT=17.8ºC.

The power obtained is shown in Figure 36 and its behaviour is depicted in equation (3-4). All the graphs show a maximum power point. It is the point where R_L (load resistance) coincides with R_{th} (internal resistance of the thermoelectric generator).

$$P_{output} = V_L I = \frac{V_{th}^2}{R_{th}} \frac{M}{(M+1)^2} \quad \textbf{(3-4)}$$

The value obtained is 4.4 ± 0.3Ω (see section 2.6.3). For this reason the maximum nominal value of the potentiometer connected is 15 Ω, as the internal resistance of the thermoelectric generator is usually of a few ohms. Thus, it is important to achieve a high temperature at the hot side, but at the same time maintain the large temperature difference.

The maximum power obtained for ΔT=17.8ºC is 29mW. However for temperature differences up to 7ºC the maximum power is lower than 5 mW. The power obtained varies with the square of the temperature (see equation (3-5)).

This trend is observed in Figure 37 which shows the variation of the maximum power as a function of different temperature differences.

$$P_{outputmax} = \frac{V_{th}^2}{4R_{th}} = \frac{\alpha^2 \cdot \Delta T^2}{4R_{th}} \quad \textbf{(3-5)}$$

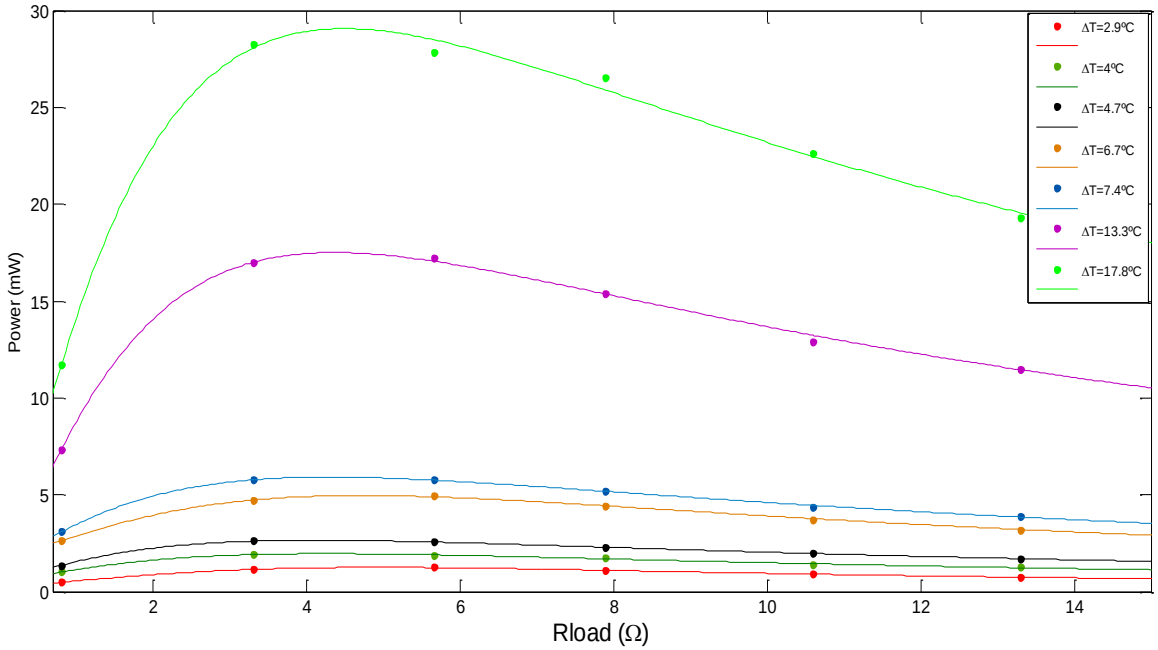

Figure 36: Power generated by the TEG as a function of load resistance and temperature difference.

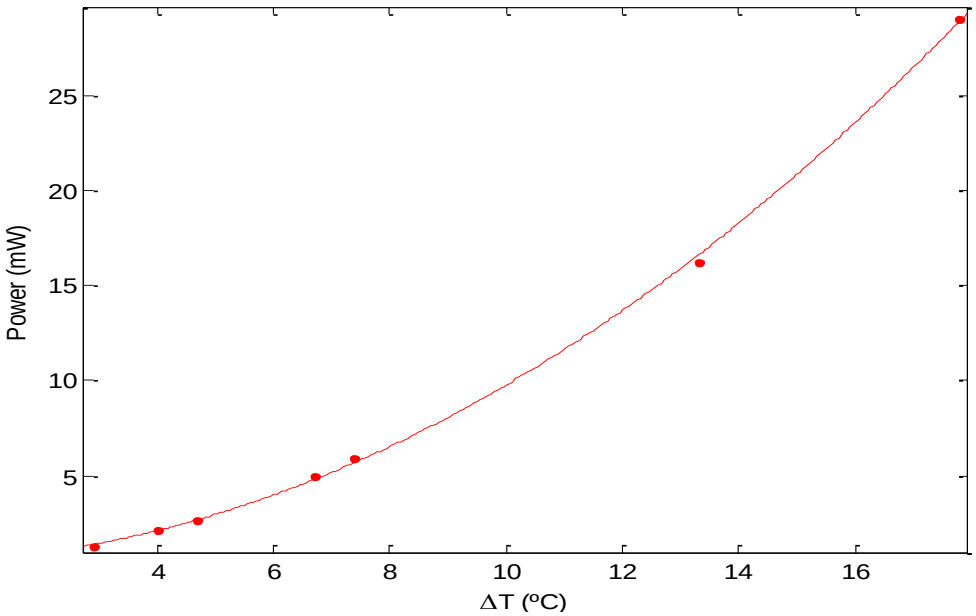

Figure 37: Variation of the maximum power with the temperature difference produced by a TEG

3.4 Summary

In this chapter, the behaviour of a thermoelectric generator was analysed. Initially, the voltage without load connected and secondly, the power achieved with a load connected was examined. The maximum voltage obtained with the load connected is 520mV and the maximum power generated was approximately 30 mW for a temperature difference of 17.8ºC.

To power a sensor node a minimum voltage of 3V was required (see Table 1, section 2.3.2), however a single thermoelectric device does not generate enough voltage to meet the needs required by the sensor node. Multiple thermoelectric generators could be connected together in series to achieve the desired voltage for the application. This solution would involve an increase in the area used and the voltage would be variable because of the variation in the temperature. The second option is to use a DC/DC converter that raises the voltage up to the voltage of the application. The voltage would be approximately constant despite the variation of the temperature. The power consumption will depend on the specific sensor as well as the time of transmission of the data.

4 STUDY OF THE SENSOR NODES

4.1 Introduction

This section analyses the operation of the wireless sensor nodes chosen for this project, which are connected to the thermoelectric generator. In the first subsection, the sensor nodes chosen are described, and in the below subsections the study of the energy consumption is completed.

4.2 Characterization of the sensor nodes

The development kit provided by PrismaSense [20] is consisted of 3 sensor nodes and 2 gateways (one Wi-Fi gate and one GPRS gate). Appendix B shows the technical specifications of the sensor nodes and the Wi-Fi gateway.

Each module (wireless sensor node) is composed of a sensing unit, a processing unit, and a transmitting unit. The sensing unit in the nodes ("Quax MS" F36 and EF2) is comprised of temperature, light and humidity sensors and one accelerometer (see Figure 38). However, no sensors are embedded in the "Quax DT 198" node, but a temperature sensor can be attached to it as Figure 39 shows.

The processing unit for all the nodes is the MPS430F1611 processor from Texas Instruments [52]. Finally, the Zigbee protocol is used by the transmitter unit to communicate with the gateway.

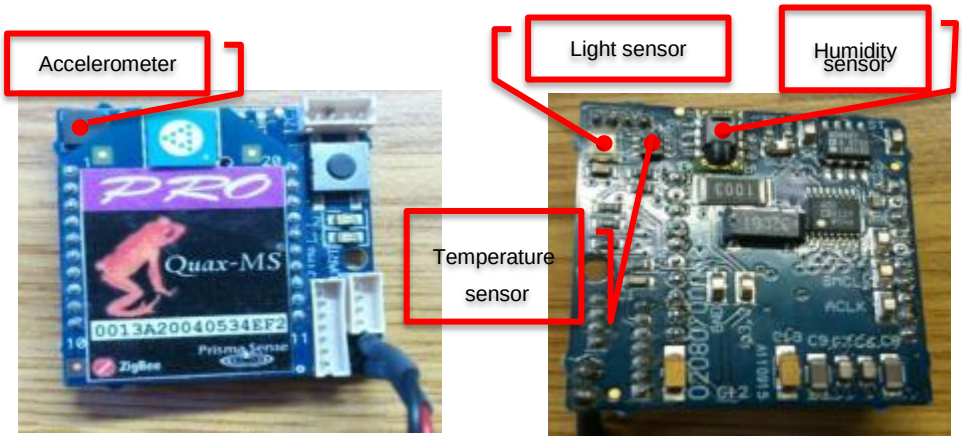

Figure 38: "Quax MS" (F36 and EF2) sensor node (front part and bottom part)

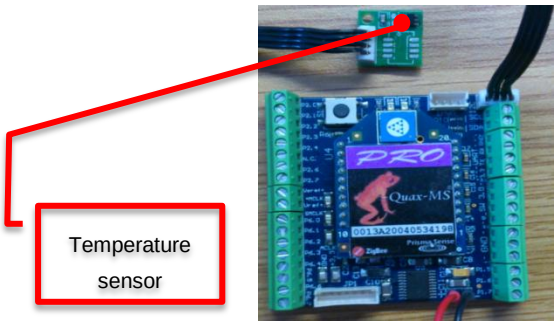

Figure 39: "Quax DT" (198) sensor node with temperature sensor

There are two gateways available in the development kit. The first gateway uses Wi-Fi connection to transmit the data to the laptop or computer. The second gateway operates with GPRS connection, for this reason, a SIM card is needed. The function of the gateway is the connection between the sensor nodes and the final user or coordinator. Thus, it utilizes two different protocols. The communication with the sensor nodes is established by Zigbee protocol, in order to reduce the power consumption of the nodes. However, the communication with the computer (user) can be established by means of cables (Ethernet) or via wireless (Wi-Fi or GPRS). The power consumption of the latter protocols is higher but the communication range is also higher (see section 2.2). A schematic of the operation of the whole system (gateways, sensor nodes, and their transmission with the computer) can be observed in Figure 40.

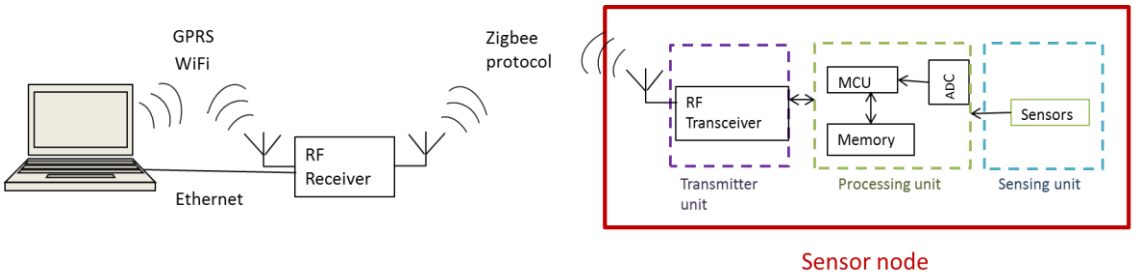

Figure 40: Schematic of the communication between the wireless sensor node, the gateway and the coordinator (computer) in PrismaSense nodes.

4.3 Configuration of the sensor nodes

In order to use the sensor nodes and the gateways, they have to be configured. For the gateways in this project, Wi-Fi protocol was chosen. Consequently, an ad-hoc wireless network was created. An ad-hoc wireless network is a kind of network where two or more devices can be connected. These two devices (gateway and laptop) are prepared to use wireless communication. However, the difference with the conventional Wi-Fi is that they can be connected between each other without the necessity of using a router.

Once the ad-hoc wireless network was established, a virtual port had to be created with the aim of connecting the gateway with the laptop. The program “CPR Manager” associates the IP of the gateway, which in this case is dynamic, with the laptop (see Figure 41).

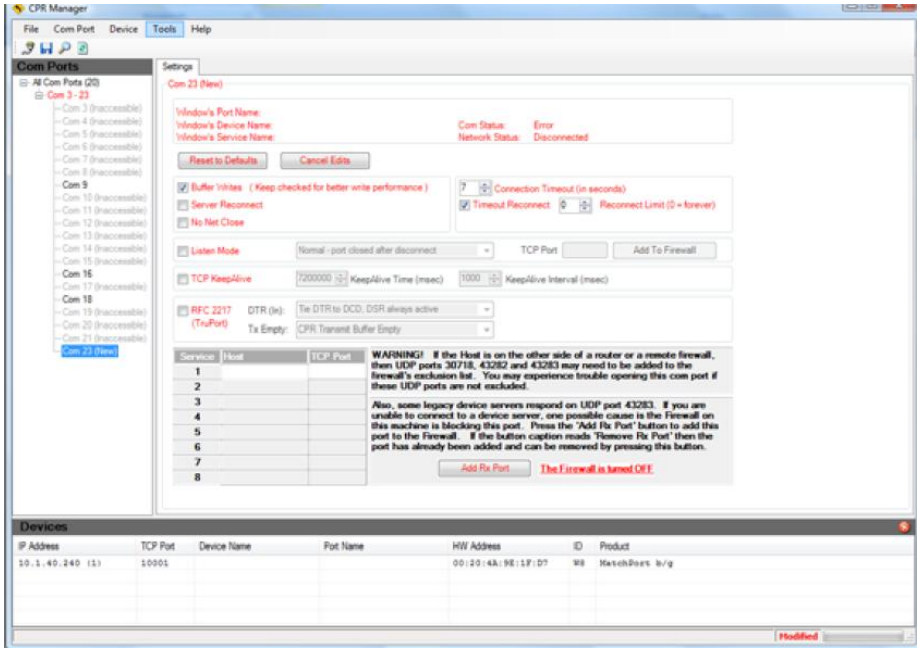

Figure 41: "CPR Manager" interface

Likewise, the nodes were programed with C++ and they were connected to the gateway. “Code Composer Essential 2.0” from Texas Instruments was the program utilized.

In this case, temperature sensors and accelerometers were used. For different experiments, sampling frequency of the data between the sensor nodes, the gateway and coordinator was modified in both sensor nodes (“Quax DT” and “Quax MS”) (Figure 42).

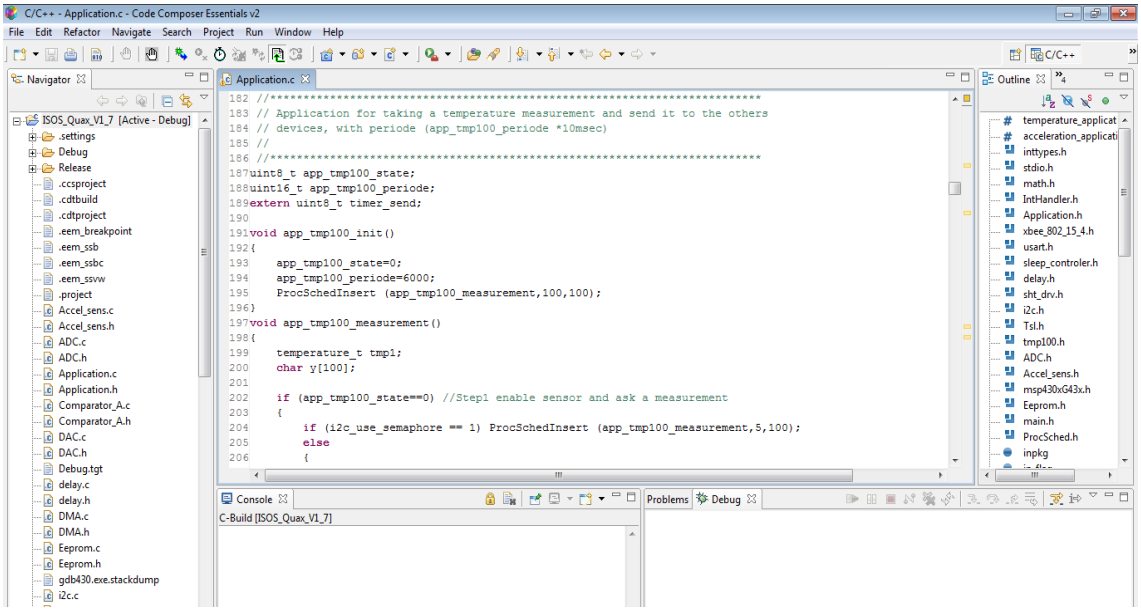

Figure 42: Code Composer v2 interface to configure the nodes

Data from the nodes (temperature and acceleration) were collected by means of excel associated to the “PS_Server Data Manipulation” program. It receives the data from the gateway that are sent from the sensor node. Figure 43 shows the interface of the program. The three sensor nodes are active (green colour) and connected to the gateway (see lines between sensor nodes and gateway (Figure 43)).

Figure 43: Connection between wireless sensor nodes and gateway. The lines indicate Zigbee connection

4.4 Power consumption of the sensor nodes

4.4.1 Method

The quoted (PrismaSense) power consumption of the sensors while sleeping is approximately 7 mW, however, if they are transmitting the power consumption is less than 200mW and the transmission of the data lasts 50ms.

This was confirmed by undertaking the following measurements. The sensor node was connected to the batteries (2AA of 1.5V each) and a 1 Ω resistance in series. A multimeter was connected across the resistor to measure the voltage, hence, the current needed by the sensor node [53] (Figure 45). The voltage measured across the sensor node was 2.8 V. Thus, by knowing the current across the resistor and the voltage across the sensor node, power of the sensor node can be calculated.

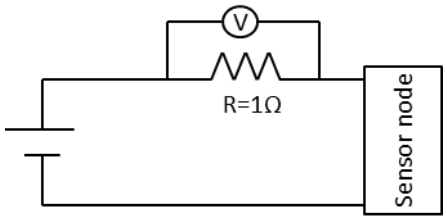

Figure 45: Schematic of the current measurement circuit for the sensor node

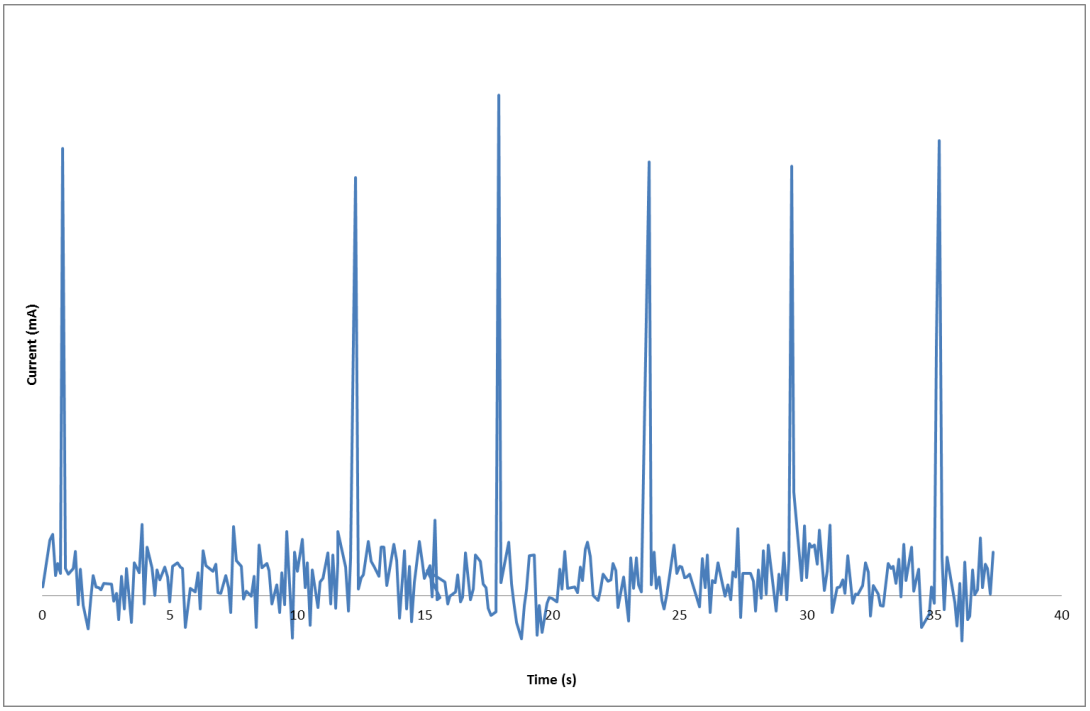

Figure 44: Profile of the current measured with Agilent 34410

In order to measure the voltage, an “Agilent 34410a” multimeter was used, whose internal impedance is 10Mohm ± 1%. The multimeter was connected to the computer by means of Excel interface. Samples were taken every 0.1s (100ms), which was the maximum resolution value. Thus, if the transmission lasts 50 ms, the multimeter has insufficient resolution to measure the whole transmission of the sensor node. The graphic profile obtained with the sensor node transmitting every 5 seconds is shown in Figure 44.

Hence, the multimeter can only be used to measure the power during sleeping time. The results obtained showed that for the “Quax DT” sensor node (temperature sensor “198”) the sleeping current measured was 1 mA at 2.8V (2.8mW) and for the “Quax MS” sensor node with the accelerometer sensor embedded (“F36” sensor), it was 1.8mA at 2.6V (5.04 mW).

For measurements of the transmissions, an oscilloscope (ISO-TECH IDS 710) was utilized. Figure 46 shows one of the graphs obtained during the transmission. The first peak (1) is the power consumption of the green led when the transmission starts. The higher peaks are those of the transmissions. The reason for the appearance of two peaks in the transmission could be that the accelerometer sensor sends two measurements (acceleration across x-axis and y-axis). In this case the values are 99mW and 114mW. Peaks 3 and 4 could be the power consumption of the sensor when it verifies if the node is connected to the gateway. Their value does not achieve the value during the communication, although it is significant (approximately 27mW).

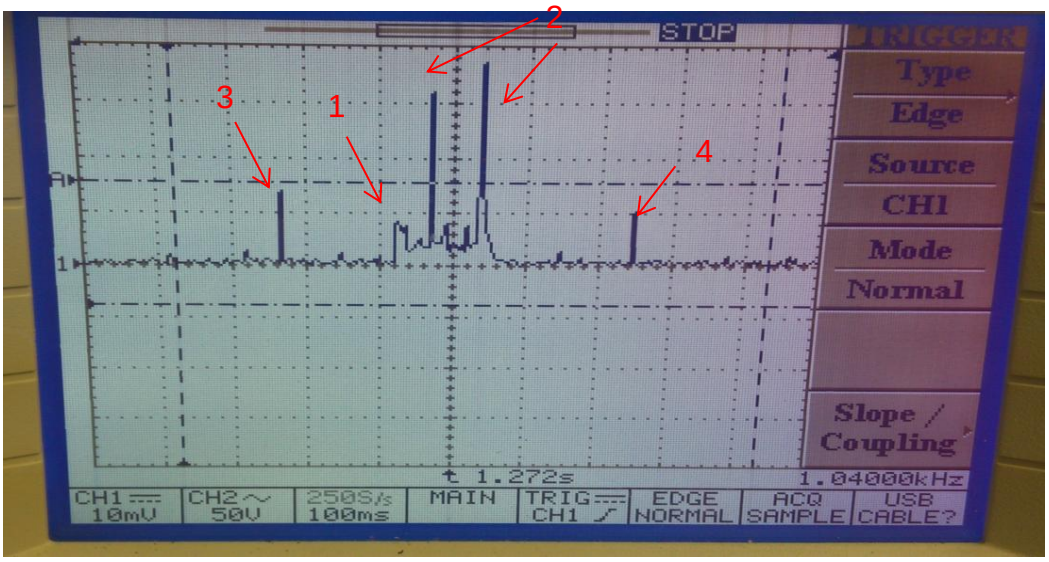

Figure 46: Peaks of transmission for accelerometer “Quax MS” sensor node measured by the oscilloscope

The shape of the data obtained from different peaks for different transmissions was very similar, although the value of the highest peaks varied as can be seen in Figure 46. Thus, it can be deduced from the measurements taken that the

power consumption during transmission also varied. The data transmission duration, as shown by oscilloscope, was approximately 100 ms.

For the “Quax DT” sensor node (temperature sensor), the profile obtained during the transmission is shown in Figure 47, the power consumption is much lower than the accelerometer (50mW), although, different peaks appear as well. The first two peaks are due to the red and green LEDs and the last peak the transmission.

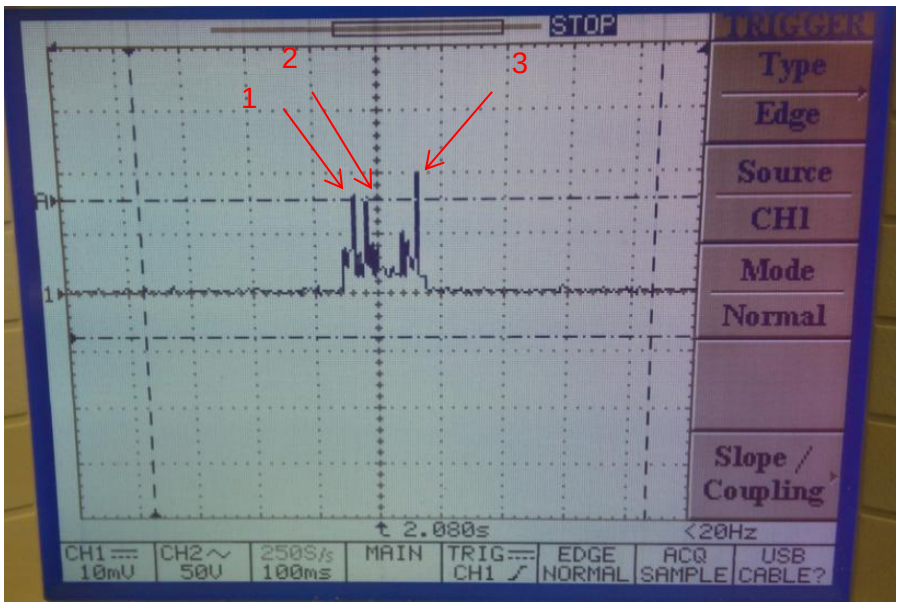

Figure 47: Peaks of transmission for temperature “Quax DT” sensor node measured by the oscilloscope

4.5 Another approach

The data obtained from the measurements are of the same order of magnitude of the data provided by PrismaSense, however, the measurements indicate that the power consumption is lower and the power consumption is relatively different from one transmission to another.

To check the difference in the power consumption, another experiment was undertaken. A capacitor of 10 F, whose maximum voltage is 2.7V, was charged up to 2.65V. The temperature sensor node The “Quax DT” node was connected to the capacitor and the capacitor discharge time was measured. “Quax DT” node was configured to send measurements every 5 seconds (Figure 48).

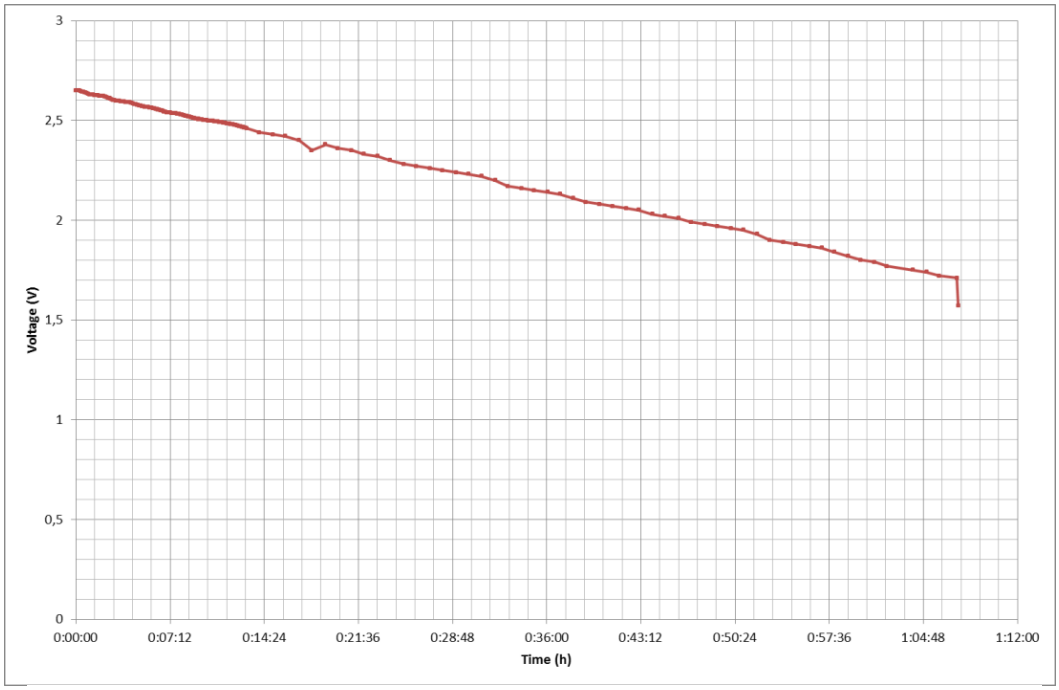

Figure 48: Capacitor voltage as a function of the time with “Quax DT” sensor node (temperature sensor) connected. Data transmission was every 5 seconds

The sensor node operated for 1 hour and 7 minutes, from a voltage of 2.65V (full charged) to 1.71V.

The average current (I_{av}) for a sensor node for a determinate period of time (T_{period}) is given by equation (4-1):

$$I_{av} = \frac{(I_{sleep} \cdot T_{sleep} + I_{awake} \cdot T_{awake})}{T_{period}} \quad \textbf{(4-1)}$$

with I_{sleep} the current when the sensor node is sleeping and I_{awake} the current when the sensor is transmitting. T_{sleep} and $T_{awake} = T_{period} - T_{sleep}$ are the periods of time sleeping and transmitting, respectively.

The discharge of the capacitor with I_{av} is depicted by the equation (4-2):

$$t = \frac{C \cdot (V_i - V_f)}{I_{av}} \quad \textbf{(4-2)}$$

Being t the capacitor discharge time, V_i the initial voltage, V_f the final voltage and C the capacitance of the capacitor.

As $I_{sleep} = 1mA$ and t (capacitor discharge time) is 1 hour and 7 minutes. In this case $V_f =$ 1.71 V, $V_i =$2.65V and $C = 10F$. The awake current (I_{awake}) is calculated from equation (4-1) and equation (4-2). Taking the sensor node transmitting every 5 seconds (Figure 48) and $T_{awake} = 300ms$ and $T_{period} = 14s$, I_{awake} obtained is $63.1mA$.

The result of I_{awake} calculated from the formula above differs from the values measured in the previous section. The power consumption calculated for the transmission is 176.7 mW. Thus, besides the transmission and sleeping modes, there is another contribution in the power consumption, as explained above, due to the sensor is verifying if the connection is correct between the sensor node and the gateway.

In order to compare these data, with different transmission frequency (15s, 30s, 1 min, 5 min), the “Quax DT” sensor was connected to the management circuit developed below and the behaviour of the capacitor was analysed. The discharge of the capacitor is represented in Figure 49.

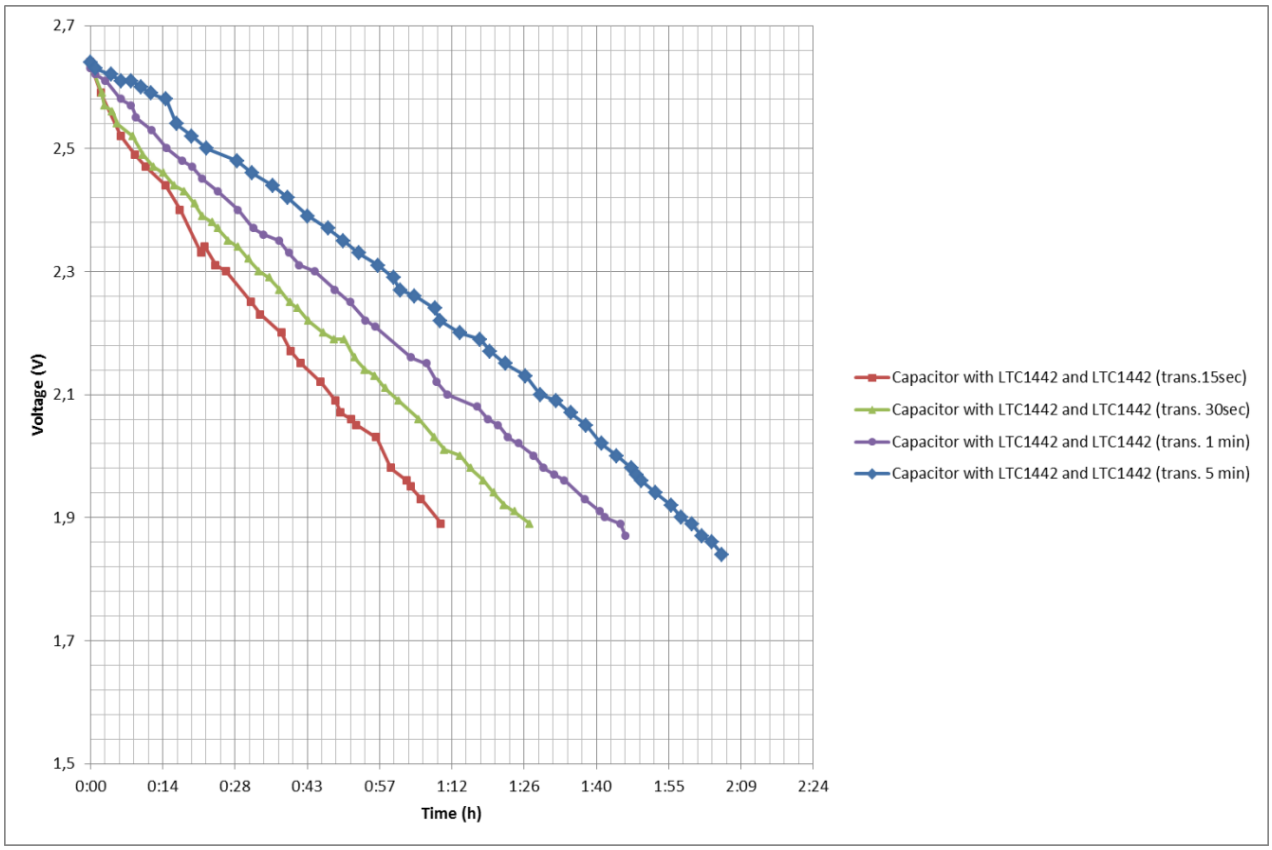

Figure 49: Capacitor voltage as a function of the time (with power management unit). "Quax DT" sensor node connected for different transmission frequencies.

Figure 49 shows that for this sensor node ("Quax DT") the data transmission frequency is not the main variable that affects the power consumption. If the unique variable is the transmission frequency, the discharge time of the capacitor when the sensor is transmitting every 15 seconds (square-shaped markers "Capacitor with LTC1442" (trans. 15sec)") should be 20 times the discharge time of the capacitor when the sensor is transmitting every 5 min (rhombus-shaped markers "Capacitor with LTC1442" (trans. 5 min)"), but this does not occur. Thus, there is another parameter independent of the data transmission, increasing the power consumption. The sensor node is always checking if the connection between the node and the gateway is correct.

4.6 Summary

In this chapter the PrismaSense sensor nodes used in the project are analysed. Two wireless sensor nodes were tested, Quax MS and Quax DT. The sensing unit for the first node was an accelerometer and a temperature sensor and a temperature sensor for the second node. The sensor nodes sent the information to a gateway via Zigbee protocol and from the gateway to the final receiver (laptop) the information was sent via WiFi.

In order to calculate the power consumption of the sensor nodes several methods were carried out. The first approach was to connect a 1 Ω resistor in series with the sensor node and the batteries. The multimeter “Agilent 34410a” was connected across the resistance. The multimeter did not have enough resolution to measure the whole transmission of the sensor node. Thus, the multimeter could only measure the power during the sleeping mode. For the “Quax DT” the power consumption during sleeping mode was 2.8 mW and for the “Quax MS” approximately 5 mW.

Regarding the power consumption during the transmission mode an oscilloscope was used. Another approach was to measure a 10F capacitor discharge time for the “Quax DT” node. It was calculated that for the transmission mode the power consumption was 176.6 mW, a value relatively high compared to other sensors with the same characteristics.

Therefore, although it is ensured that thermoelectric generator can supply enough power to the sensor during the sleeping mode, an energy support must be provided during the transmission period.

5 ENERGY HARVESTING CIRCUIT

5.1 Introduction

In the previous sections, thermoelectric generators and sensor nodes have been described and studied. Sensor nodes are powered by two 1.5V AA batteries. In order to replace these batteries with the thermoelectric generator similar outputs need to be achieved and require an energy harvesting circuit.

The first aspect to be taken into account is the temperature differences. Temperature differences present in the environment are not constant over time, thus the voltage provided is also not steady. However, sensor nodes like other electronic devices need a stable voltage. A DC/DC converter is required in order to adapt the low voltage generated by the thermoelectric generator to the sensor node and to keep it constant (Figure 50). Important requirements for the system are robustness and reliability. Namely, sensors should keep working although the temperature difference is not high enough to power the sensor. Consequently a storage element is needed. When the temperature difference is sufficient to supply energy to the sensor, the excess power generated by the thermoelectric device is used to charge the storage element.

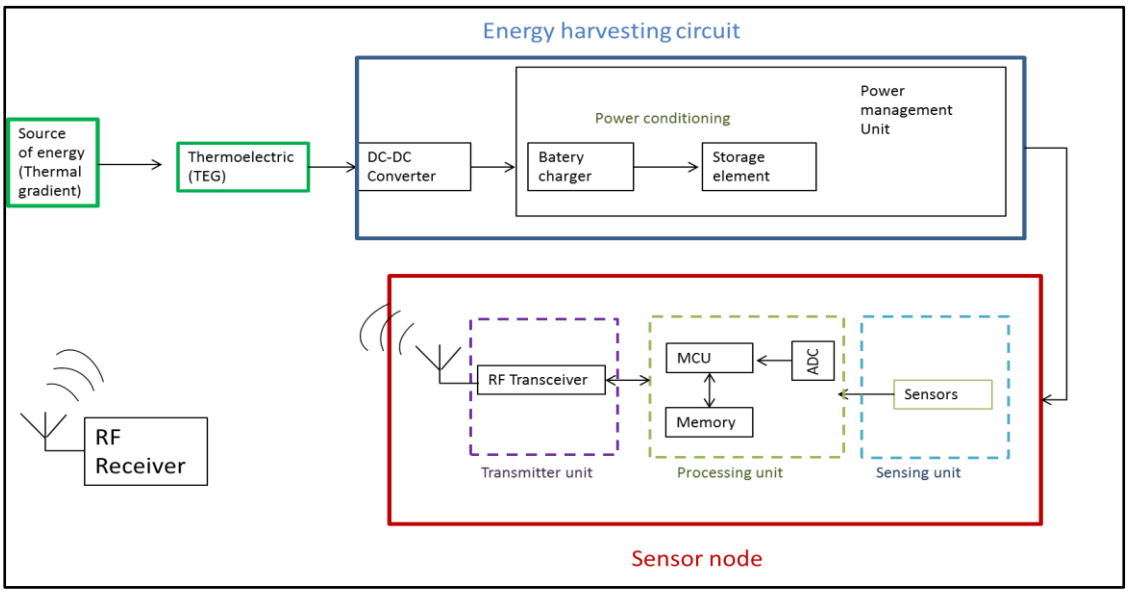

Figure 50: Schematic of the connection of the energy harvesting circuit and sensor node.

Additionally, a power management unit is required to distribute the energy efficiently to the storage element and to the sensor node. The schematic of the whole system (energy harvesting circuit and sensor node) is represented in Figure 50. With a temperature difference, through the thermoelectric device, electricity is generated. The energy harvesting circuit, where the DC/DC converter and power management unit are included, adapts the voltage from the thermoelectric generator to the sensor node voltage, charges the storage element and distributes the energy. The node takes the measurements required (e.g. acceleration and temperature), processes the signal and sends the information via wireless to the receptor.

5.2 Design and selection of the components of the energy harvesting circuit

5.2.1 DC/DC converter

Several types of DC/DC converters exist in the market. For example, charge pumps, buck/boost converters and linear regulators [54]. Charge pumps and buck/boost converters have high efficiency but their main drawback is the noise generation during their operation. However, linear regulators are less efficient but the noise generation is smaller.

Charge pumps and boost/buck converters are commonly used with thermoelectric generators [55-58]. The most important difference between buck/boost converters and charge pumps is that in buck/boost converters, an inductor is required. Consequently, their miniaturization is more difficult, although the efficiency (relation between output power and input power) is higher, as well as the conversion factor (relation between V_{output} and V_{input}) [59]. In charge pumps only capacitors are required which makes easier to integrate them in small or nano devices.

However, enough space is available for sensor nodes in tidal turbines, so, the use of an inductor is not a drawback because larger devices can be constructed.

There are two kinds of DC/DC converters depending on the input voltage and the output voltage. DC/DC converters will be step-up (if the voltage required is higher than the voltage supplied by the harvester) or step- down (if the voltage required is lower than the voltage supplied by the harvester).

The maximum voltage supplied by the thermoelectric generator measured in the lab was 800mV at 25ºC for open circuit conditions, but with a load connected at 17.8ºC, this is approximately 520 mV (see section 3.3.2). The sensor node requires a voltage of 3.3V, thus, a step-up converter is required. Another characteristic of the DC/DC converter to be taken into consideration is its start-up voltage. In this case a low start-up voltage is very appropriate. The boost converter chosen was LTC3105 [60] by Linear Technologies with a start-up voltage of 250 mV. Input voltage admitted varies from 250mV to 5V and the output voltage varies from 1.5 V to 5V (Figure 51).

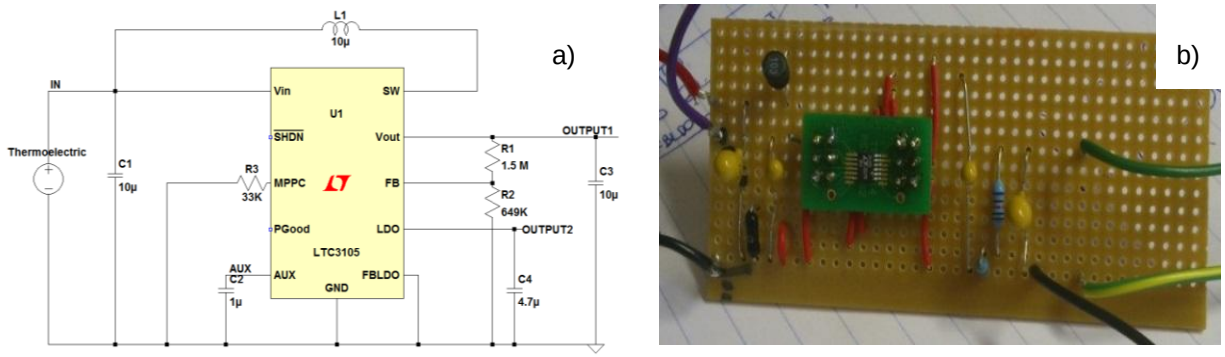

Figure 51: a) Circuit diagram and b) photograph of LTC3105 boost converter

The LTC3105 boost converter has two voltage output, “Vout” and “LDO”. The latter can provide a maximum current of 6mA. In order to start-up the circuit, V_{in} or V_{aux} (Figure 51) have to be above 1.4V. However, V_{in} does not usually reach 1.4V as the maximum value measured in the lab was 800mV, so Vaux will reach the 1.4 V with the aid of 1µF capacitor. Figure 52 shows a simulation of the behaviour of LTC3105 for an input voltage of 520mV using the program LTSpice IV. It can be explained as follows: During the start-up, the capacitor of the AUX pin is charged until the voltage in this capacitor is 1.4V. From this point, it enters in the normal operation. When the voltage in LDO (second

voltage output) is steady, V_{aux} starts to charge the output V_{out} (Figure 52). If V_{aux} falls too low, current is redirected to the “aux output” instead of being used to charge V_{out}. When V_{out} increases, V_{aux} and V_{out} are connected to the same output. The resistors R1 and R2 were chosen to achieve 3.3V in the V_{out} pin. The value of 3.3V was selected because it is optimum working point in the sensor. LDO is the second output whose voltage attained is 2.2V and the maximum current is 6 mA. This output was not used due to its low current value.

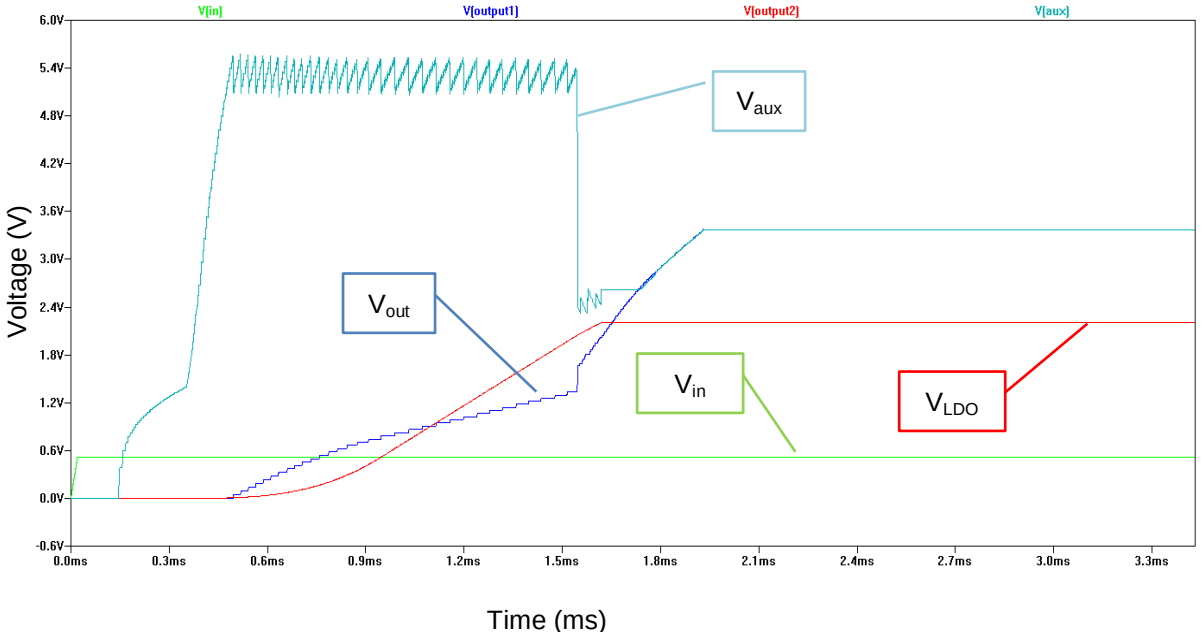

Figure 52: LTSpice IV simulation of LTC3105 converter for V_{in}=520mV

The pin MPPC (Maximum Power Point Control) (Figure 51) controls the input voltage from the energy harvester in order to work in the point of the maximum power (MPP). It will depend on the energy harvester used. For the thermoelectric device “ET-127-14-11-RS”, the ESR (Equivalent series resistance) is fixed at 4.4 Ω (calculated in section 3.3.2). For this value of resistance connected, the power achieves its maximum value and the voltage will depend on the temperature difference. For the maximum temperature difference of 17.8ºC, voltage for closed circuit conditions is approximately 350 mV. The current in the MPPC is 10µA, for this reason, 33kΩ was chosen. As in

most of the measurements taken in the lab the temperature difference was lower, the resistance selected was 33kΩ. If the temperature difference decreases the voltage also decreases, approaching to the maximum power point.

5.2.2 Storage unit

Once the DC/DC converter was chosen, the storage unit and the power management unit were considered.

Regarding the storage unit, there are two kinds of storage units that can be used:

- Short term storage: They are small capacitors. They are used to supply energy in the very short term spikes. The charge and discharge of the capacitors are very fast.
- Long term storage: These storage elements provide energy for long periods, when a shortage of energy exists. Rechargeable batteries, supercapacitors or ultracapacitors are used as long term storage.

In order to supply energy to the sensor, when the temperature difference is not high enough to start-up the DC/DC converter or to power the sensor, long term storage was chosen.

Differences between the rechargeable batteries and supercapacitors are explained below. A comparison of several rechargeable batteries and supercapacitors are described in Table 6 and Table 7. Figure 53 shows the Ragone chart, which compares different storage units. The vertical axis represents the energy density in Wh/kg, namely, the amount of energy available. The horizontal axis represents the power density (W/kg), the speed that this energy can be delivered. The diagonal lines represent the lines of discharge.

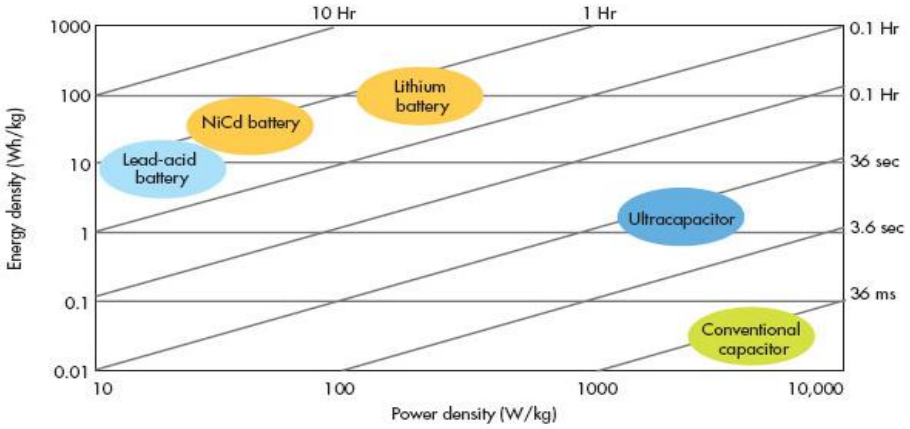

Figure 53: The Ragone chart for batteries and capacitors

By considering Table 6 and Table 7, the following characteristics can be compared. The voltage of the rechargeable batteries is fixed in each battery and depends on the chemistry of the battery. Battery voltages vary from 1.2 V to 3.6V, while the voltage of the supercapacitors varies from 2.7V to 5V.

The number of the rechargeable cycles that the rechargeable batteries can sustain is on the order of a few thousand times, but it is relatively low if they are compared to supercapacitors, which may reach millions of cycles. Consequently, the lifetime of the batteries is lower.

Batteries are more sensitive to the period of charge and discharge. For example, Lithium-Ion batteries require a constant current and voltage charging arrangement, otherwise they may explode. For Ni-MH (Nickel Metal Hydride) batteries the range of charging current is wider and much safer. Nevertheless, they require a complex algorithm in order to charge them, as the overcharge cannot be controlled with only setting a maximum charge voltage. Batteries are more sensitive to overcharge and undercharge, thus, they need a set control for maximum and minimum voltage and current. However, supercapacitors can be recharged from 0V to its maximum voltage value, without the necessity of using complex algorithms.

The more drastic difference between supercapacitors and batteries is the maximum stored energy (E_{max}). For capacitors and for batteries, E_{max} is represented by the equation (5-1) and equation (5-2), respectively.

$$E_{max} = \frac{1}{2} \cdot C_{cap} \cdot V_{cap}^2 \quad \textbf{(5-1)}$$

$$E_{max} = V_{bat} \cdot C_{bat} \cdot 3600 \quad \textbf{(5-2)}$$

Where C_{cap} is the capacity of the capacitor (in F), C_{bat} is the capacity of the battery (in Ah). V_{cap} and V_{bat} are the value of the maximum voltage reached for capacitors and batteries respectively (in V).

The maximum energy stored in batteries is roughly 31000 Ws (see Table 7), however, for a supercapacitor, the maximum energy stored is on the order of 1000 Ws for 350F (see Table 6). Thus, the selection of the storage unit will depend on the duration of the periods of shortage of temperatures differences and the charge time.

For energy harvesters such as solar panels, batteries are required due to the lack of sun during the night and during cloudy days. However, temperature differences are present during the operation of the parts to be monitored. Thus, the period of the shortage of temperature difference is likely to be very short when the parts are working. If the parts stop working the temperature differences will disappear but the monitoring of the condition will also not be necessary. In addition, the charge and discharge cycles for batteries are too strict or too complex. For these two reasons supercapacitors were chosen for this work. The current to charge the capacitor can vary from Amperes to mA.

A 10F Cooper Bussmann supercapacitor was chosen for this application [61]. As sensors are powered by two 1.5V batteries (3 volts in total) and the voltage range of the sensor nodes varies from 1.8 to 3.6V, the 2.7V capacitor was selected, because there was not supercapacitor in the market with 3.3 V of voltage. The 2.7 V supercapacitor was the most similar to this voltage.

Table 6: Comparison of performance for different supercapacitors [61-65]

	Maxwell BCAP350	COOPER BUSSMANN	MAXWELL PC10	CORNELL DUBILIER - EDLHW226D2R 3R	PANASONIC - EECHW0D506	PB-5R0V-R
Storage type	350F Supercapacitor	10F Supercapacitor	10F Supercapacitor	22F Supercapacitor	50F Supercapacitor	1F Supercapacitor
Cycles	500000	500000	500000	500000	500000	500000
Nominal voltage (V)	2.5	2.7	2.5	2.3	2.3	5
Lifetime	10-20 years	-	10 years	15 years	-	-
Leakage current (mA)	0.3	0.026	0.04	0.004	-	0.012
Weight (g)	60	20	6.3	9	14	3.5
Size	D size	60 height x ϕ18	29.6mmx23.6mmx 4.8mm	35 height x ϕ18	40 height x ϕ18	8.5 x 16.8 x 21.5 mm
Operating temperature	-40^0C to 65^0C	-40^0C to 65^0C	-40^0C to 70^0C	-25^0C to 85^0C	-25^0C to 60^0C	-25^0C to 70^0C
Emax (J=Ws)	1094	36.45	31	58	132	12.5
Cost	$20	2.4£	10$	9£	5.5£	
Self-discharge	< 30% month	< 30% month	< 30% month	< 30% month	< 30% month	< 30% month
ESR (Ω)	-	0.01	0.18	0.1	0.3	0.5

Table 7: Comparison of performance for different AA rechargeable batteries [66-69]

	Panasonic HHR210AA/B	TADIRAN BATTERIES - SL360S	YUASA BATTERY, NICD	Panasonic BR-AG
Storage type	NiMH	Lithium-Ion (Li-$SOCl_2$)	Ni-Cd	Lithium
Cycles	300	500	1000	1000
Nominal voltage (V)	1.2	3.6	1.7	3
Capacity (mAh)	2000	2400	1000	2200
Lifetime	< 3 years	<3 years	<3 years	10-20 years
Leakage current (mA)	400	20	-	2.5
Weight (g)	29	18	-	18
Size	AA	AA	AA	AA
Operating temperature	-10^0C to 65^0C	-55^0C to 85^0C	-	-40^0C to 85^0C
Emax (J=Ws)	8640	31104	6120	23760
Cost	3$	5$	6$	10$
Self-discharge	<30% month	<10% month	10% month	<1% month
ESR (Ω)	0.025	-	-	-

5.2.3 Power management unit

5.2.3.1 Description of the system

The power management unit distributes the power through the whole system. In the literature review, different kinds of power management were considered, depending on the application, the energy harvester used and the simplicity of the system [70-74]

For each power management unit, different types can be selected as they are described as follows:

- Using a microprocessor: A MCU (microcontroller unit) can be used to manage the power efficiently, it requires high power. Another option is to insert the routine to the microprocessor of the sensor node, although, like the first option, the power required is high. Moreover, PrismaSense node has high power consumption itself, so, if more operations are added to the sensor node, the power consumption will be extremely high.
- Analog circuit: In these circuits, only analog components are utilized. They can be used to save power consumption, that is very important for energy harvesters, or to construct simple and effective circuits.

For this project, a simple and effective circuit was chosen, in order to operate between the thermoelectric harvester and the sensor node. Furthermore, because the power provided by the thermoelectric generator is not very high, the distribution of the power will be very strict. A microprocessor would consume too much power. Due to this other reason, the analog circuit was selected.

A schematic of the circuit designed and constructed is depicted in Figure 54, along with all the system. The thermoelectric harvester, with a temperature difference, is capable of generating a certain voltage. The voltage generated is not high enough to power the sensor, thus, this voltage is transformed by the DC/DC converter to 3.3V. Although the voltage is set at 3.3V, higher measurements were taken in the lab in the output of DC/DC converter until the

voltage was stabilized. However, the voltage of 2.2V in the pin LDO (see section 5.2.1) was never exceeded.

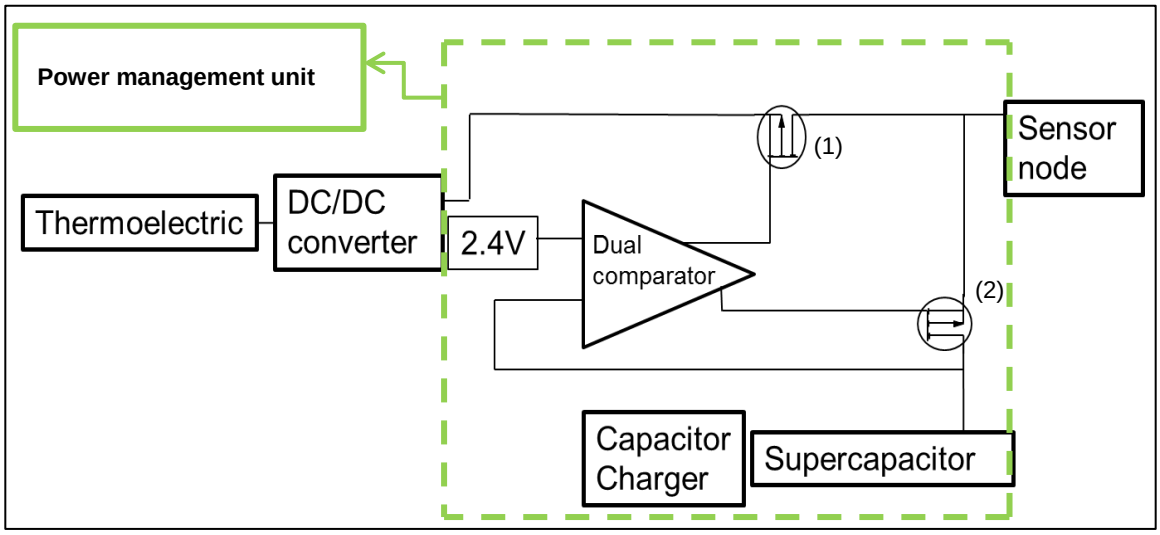

Figure 54: Schematic of the whole system (power management unit inside dotted line)

The circuit is controlled by a dual comparator (LTC1442 by Linear Technologies). It is an integrated circuit with two outputs and a reference voltage established by the resistors connected. See Appendix C. If the input voltage is lower than the reference voltage, one output will be high (the current will pass by this output) and the second output will be low (the current will not pass by this output). If the output voltage is higher than the reference, then the first output will be low and the second output will be low. It works as a switch.

Therefore, the dual comparator regulates the two p- channel mosfet transistors, numbered as (1) and (2) in Figure 54. If the voltage of the capacitor is lower than 2.4V, the transistor allows the current to flow between the thermoelectric device and the load (sensor node), while the thermoelectric generator is also charging the supercapacitor. When the supercapacitor reaches 2.4V, the thermoelectric harvester only powers the sensor through the capacitor. Hence, when the voltage is approximately 2.38V transistor (1) is deactivated and transistor (2) is activated. Likewise, the supercapacitor powers the sensor node, at the same time the thermoelectric generator charges the supercapacitor.

As the supercapacitor does not need strict measures regarding to the current or voltage charge, the current charge is not required to be constant. Nevertheless, the capacitor has a maximum voltage that must not be exceeded. Hence, a maximum voltage adjustment is required, which is the capacitor charger. As the maximum capacitor voltage is 2.7V, the maximum value will be established at a value of 2.65V.

5.2.3.2 Selection of the components of the power management circuit

The elements used in the power management circuit are shown in Figure 55.

The dual comparator controls two transistors. Both transistors selected are NDP6020P (TO-220) from Fairchild semiconductor [75], they are P-channel enhancement mode mosfets. In these transistors, the drain and the source of the transistor are connected through a Zener diode. If the voltage through the gate is low, the current passes from the source to the drain and vice versa. The gate threshold voltage in these transistors is low (0.7V), namely, below this value the transistor does not work. This value was selected because it is lower than the minimum voltage where the sensor node starts to work (1.8V).

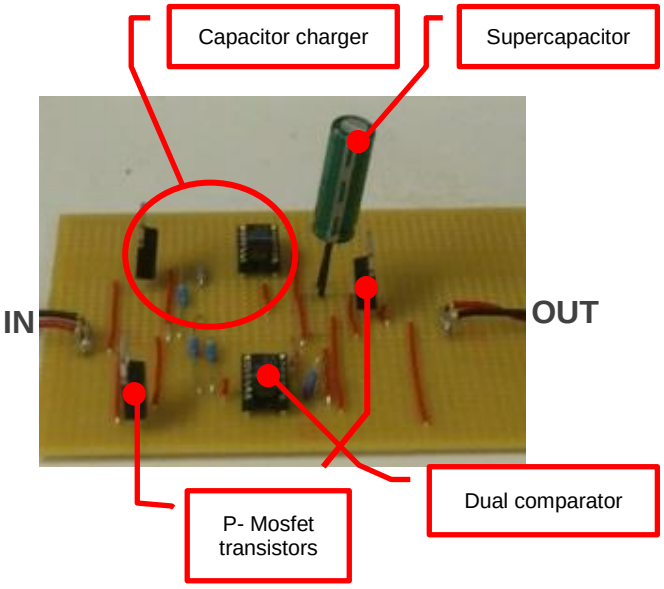

Figure 55: Power management unit with the commercial components

LTC1442 from Linear Technologies [76] is the dual comparator with reference used. If the voltage is lower than 2.4V the output connected to the first transistor is low and the transistor 1 is on and transistor 2 is off. However, if the voltage is higher than 2.4V, transistor 1 is off and transistor 2 is on. Namely, the current only flows from the capacitor to the sensor node, the first transistor does not allow the current to flow directly from the thermoelectric to the sensor node.

The supercapacitor charger is used to avoid the capacitor voltage to exceed its maximum value, which in this case is 2.7V. For this reason another dual comparator “LTC1442” was used together with a transistor NDP6020P (TO-220). When the supercapacitor reaches 2.65V, the transistor is in mode off, preventing the overcharge of the supercapacitor. If the charge of the capacitor is lower than 2.65 V the transistor allows the current to flow from the thermoelectric device to the capacitor, charging it. The dual comparator, using only one channel, was used instead of a single comparator.

In the first step of the design, a single comparator LTC1440 [76] from Linear Technology was used. The drawback was that it stopped working when the voltage was lower than 2.2V. If the sensor works up to a minimum value of 1.8V and LTC1440 works with a minimum value of 2.2V, the system does not take advantage of all the voltage available. The discharge of the capacitor was measured using these two ICs (Figure 56). By using LTC1440 the system stopped working, from the full charge value of the capacitor (2.65 V), after 43 min (2.2V). Nevertheless, by using LTC1442 the system was working during 1hour and 12 min (1.89V).

The schematic with all the components used in the final power management circuit and DC/DC converter is presented in Appendix C.

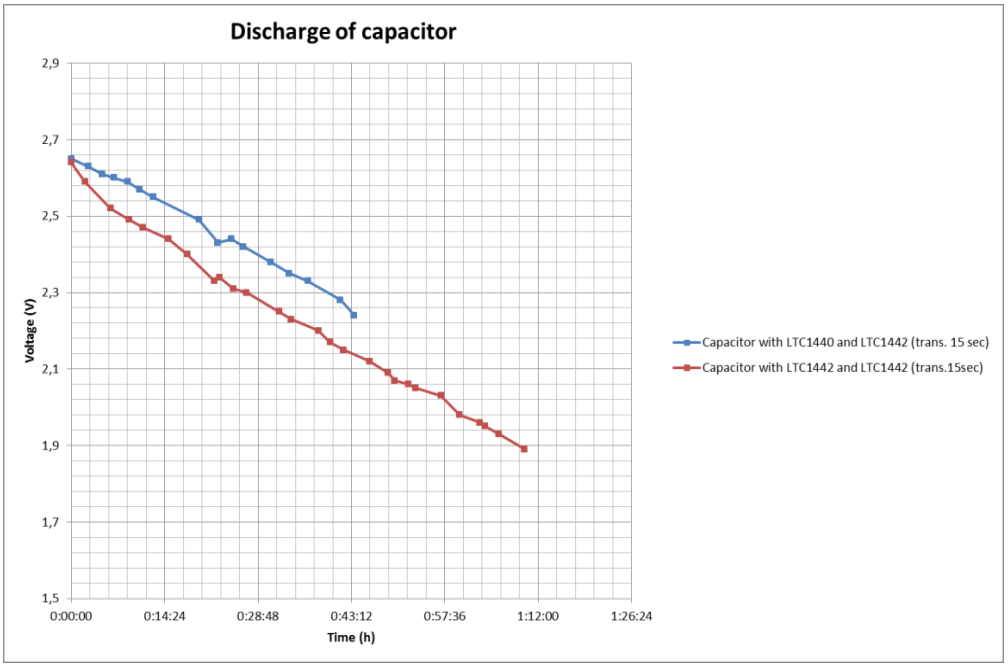

Figure 56: Discharge of the 10F capacitor using LTC1440 and LTC1442

5.3 Summary

This chapter is focused on the study, design and construction of the energy harvesting circuit that is necessary to connect the thermoelectric generator with the wireless sensor node.

In first place a boost DC/DC converter (LTC3105 by linear energy) was chosen in order to adapt the voltage from the thermoelectric generator (800mV) to 3.3 Volts, which is required by the PrismaSense wireless sensor node.

The power management unit used was an analog circuit with a 10F capacitor with a maximum voltage value of 2.7V. Thus, the energy harvesting unit basically worked as follow: The thermoelectric is connected to the DC/DC converter, charging the capacitor. If the capacitor voltage is lower than 2.4V, the thermoelectric generator feeds directly the sensor node, meanwhile the capacitor is charged. If the capacitor voltage is higher than 2.4V, the sensor node is powered via the capacitor. The transistor does not allow the current to flow directly from the thermoelectric device to the sensor node.

6 LAB BENCH CASE STUDY

6.1 Method

An overview of the configuration of the components is shown in Figure 57. The thermoelectric generator was placed on the hot plate to simulate a hot component within the turbine.

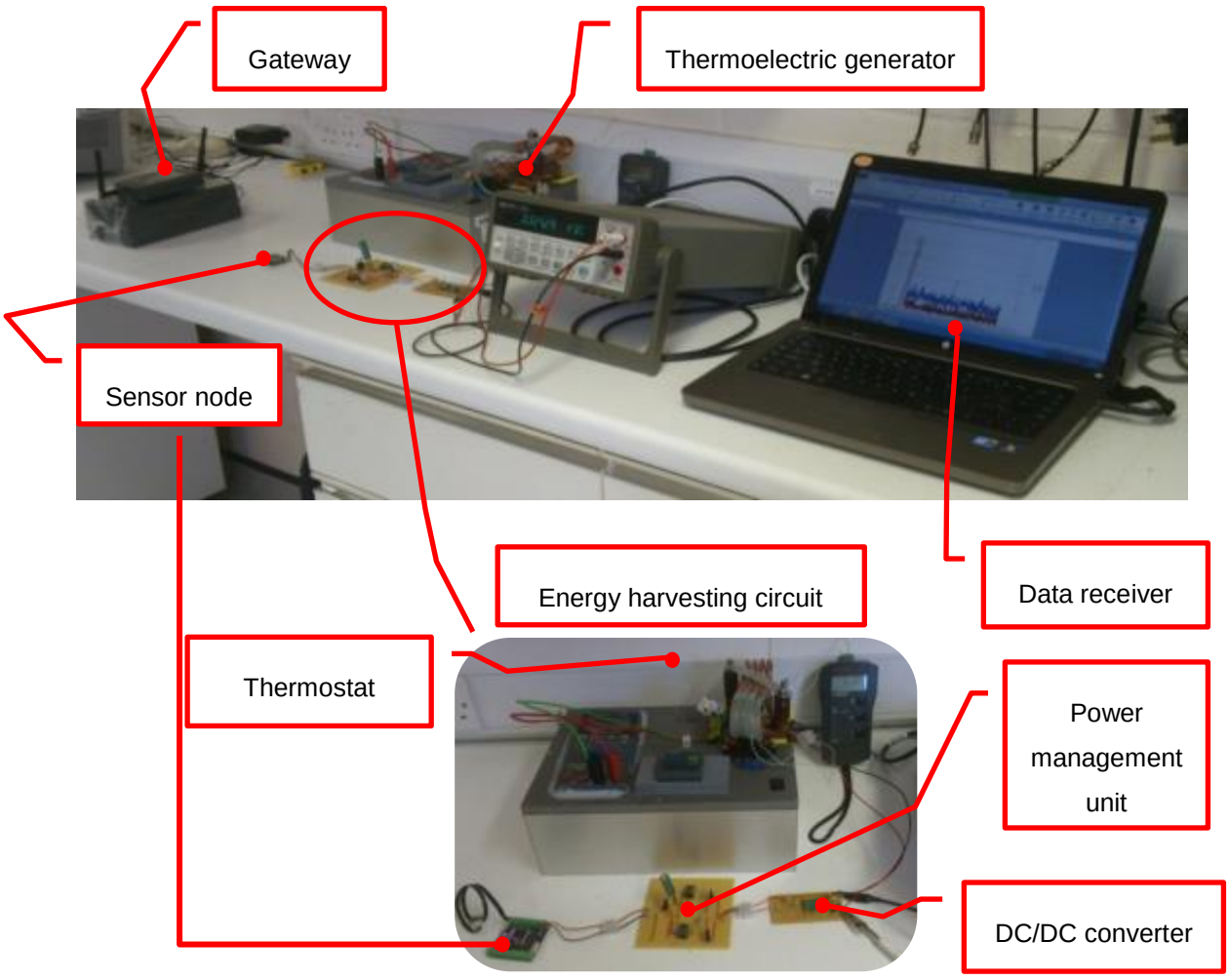

Figure 57: Harvesting system (thermoelectric generator, DC/DC converter, power management and sensor nodes)

The temperature of the hot side was measured by a thermocouple and controlled by a thermostat. The cold side of the thermoelectric device was

attached to the heat sink. The heat sink was composed of a cooper plate which was attached to 4 cooper tubes connected to 4 plastic tubes with water inside in order to dissipate the heat form the cold part of the thermoelectric device. As such, with the use of the heat sink, the temperature difference between the hot part and the cold side will increase as well as the voltage supplied by the thermoelectric generator. The temperature of the cold side was measured using a K-type thermocouple, attached to the heat sink and connected to a thermometer (RS13-14 Thermometer).

The thermoelectric generator was directly connected to the DC/DC converter which increased the voltage provided by the thermoelectric device to 3.3V through the main output. There is another output (LDO) (see section 5.2.1) that provides 2.2 V and a maximum current of 6 mA. The latter was not used due to the low power provided.

The DC/DC converter was connected to the thermoelectric generator through the power management circuit. The power management unit charged the capacitor and powered the sensor at the same time. The thermoelectric device stopped charging the capacitor when the voltage of the capacitor reaches 2.65V.

The sensor node, fed by the system described above (the thermoelectric generator, DC/DC converter and power management unit), measured temperature and/or acceleration and sent these measurements to the gateway. The communication protocol between the sensor node and the gateway used was Zigbee (see section 4).

Finally, the gateway sent the information to the laptop (data receiver in Figure 57). Moreover, the communication between the gateway and the laptop was established by means of ad-hoc Wi-Fi protocol. The data were collected with Excel interface by means of “PS_Server Data Manipulation” program (see section 4.3).

With the configuration described above the following experiments were carried out. The hot plate temperature was varied from 60ºC to 78ºC. When the

temperature of both sides (hot and cold side) was steady, the sensor was connected. The temperature of the cold side depends on the hot side temperature but it also depends on the room temperature.

Temperature and/or acceleration were the measurements taken during the experiments. Likewise, the data transmission frequency was a variable during the experiments. It was varied from 15 seconds to 5 minutes. The sensor nodes used were “Quax DT” node to measure the temperature and “Quax MS” node to measure the accelerations and/or temperatures.

In order to measure the voltage of the capacitor for different conditions an “Agilent 34401a” multimeter was used.

6.2 Results and discussion

6.2.1 “Quax DT” sensor node behaviour

The temperature of the hot side was initially fixed at 78ºC and the temperature of the cold side varied until steady state conditions were attained. For the data presented in Figure 58, the temperature of the cold side reached a temperature of approximately 60.3ºC. Thus, the temperature difference (ΔT) achieved was 17.7ºC.

For the temperature difference reached, the “Quax DT” sensor node was connected to the system. A temperature sensor was attached to “Quax DT” node (see section 4, Figure 39). Thus, the temperature measurements were sent to the gateway and finally to the laptop.

The different lines in Figure 58 show the capacitor charge for different periods of transmission of the sensor (15 seconds, 30 seconds and 1 minute) with a ΔT of approximately 17.7ºC.

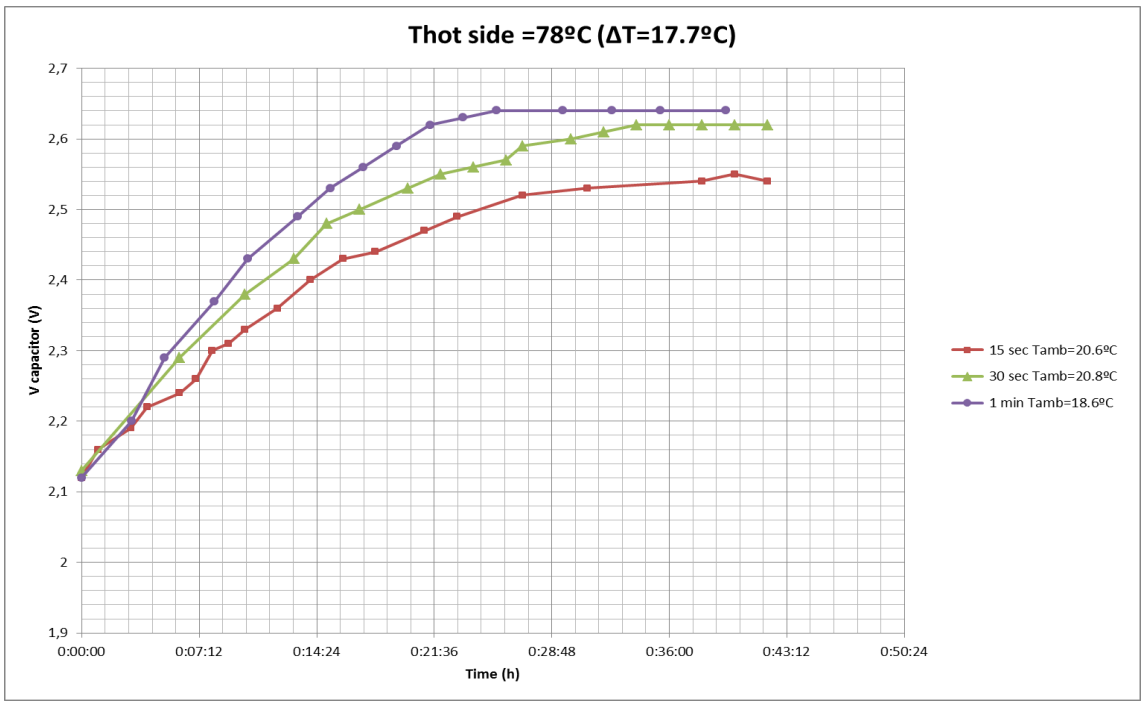

Figure 58: Voltage across the capacitor as a function of the time. Temperature sensor with the "Quax DT" node was used. Data transmission was every 15 seconds 30 seconds and 1min at T_{hot}=78ºC and ΔT= 17.7ºC

For the lowest transmission frequency, every 15 seconds (square-shaped markers from Figure 58), the power required by the sensor node was higher. Likewise, with the voltage supplied by the thermoelectric generator, the capacitor did not charge fully. It only achieved 2.55V despite a maximum voltage of 2.65V

When the data transmission frequency was lower, the charge of the capacitor increased. For a transmission interval of 30 sec, a value of 2.62V was achieved and for a transmission interval of 1 min, the capacitor was fully charge up to the maximum value, 2.64V. While the maximum voltage was reached in the capacitor, the maximum voltage measured in the main output of the DC/DC converter was 2.85V. The time of charge for the capacitor transmitting every 15 sec, 30 sec and 1 min were 25 min, 34 min and 40min, respectively, until the voltage reached the plateau.

Another interesting observation was that the difference of the capacitor charge time between cases where the transmission is every 30 second and 1 minute is not significantly. As was discussed in section 4.4, for the discharge of the capacitor, the same issue occurs here. It could be that apart from the transmission of the data, the sensor is always checking if the connection between the sensor node and the gateway is correct.

Figure 59 also shows the difference of the capacitor charge with the sensor node transmitting every 1 min and 5 min. In this case the temperature of the hot side was also 78ºC. However, the temperature of the cold side was 63.2ºC, thus, ΔT=14.8ºC. The voltage maximum was 2.55V for 5 minute transmission intervals compared to 2.39V for 1 minute transmission intervals. The temperature difference achieved was not as high as 17.7ºC due to the room temperature in this case was higher (22ºC) than for the data presented in Figure 58 (19.5ºC).

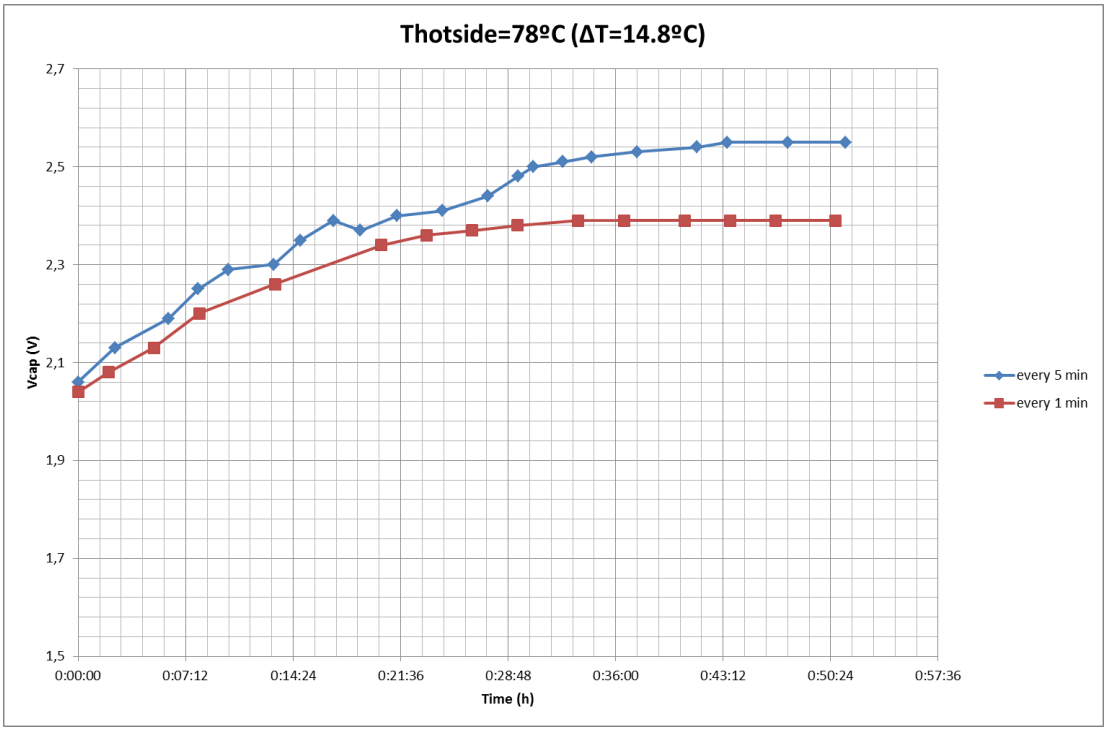

Figure 59: Voltage across the capacitor as a function of time. Temperature sensor with "Quax DT" node was used. Data transmission was every 1min and 5 min at T_{hot}=78ºC and ΔT= 14.8ºC

From this point forward, the data transmission was fixed every 1 min. The difference in power consumption between cases of transmission every 15 seconds and 5 minutes is not too large as shown in section 4.4 shown. Therefore, 1 min is a reasonable period of time for the transmission of the data and to demonstrate operation of a sensor node.

In Figure 60, the capacitor voltage as a function of temperature difference is shown with a data transmission interval of 1 min and the temperature difference using a “Quax DT” node (temperature sensor).

The graphs show the capacitor voltage for different temperature at the hot side 78ºC, 66ºC and 60ºC with a temperature difference of 15ºC and 17.8ºC for T_{hot}=78ºC and 12ºC and 9.5ºC for T_{hot}=66ºC and T_{hot}=60ºC, respectively. The higher temperature achieved the higher capacitor voltage.

For ΔT=9.5ºC (cross-shaped markers in Figure 60), the capacitor charges very slowly reaching a maximum voltage value of 2.05V. For ΔT=17.8ºC (rhombus-shaped markers in Figure 60) the voltage reaches its maximum value (2.65V).

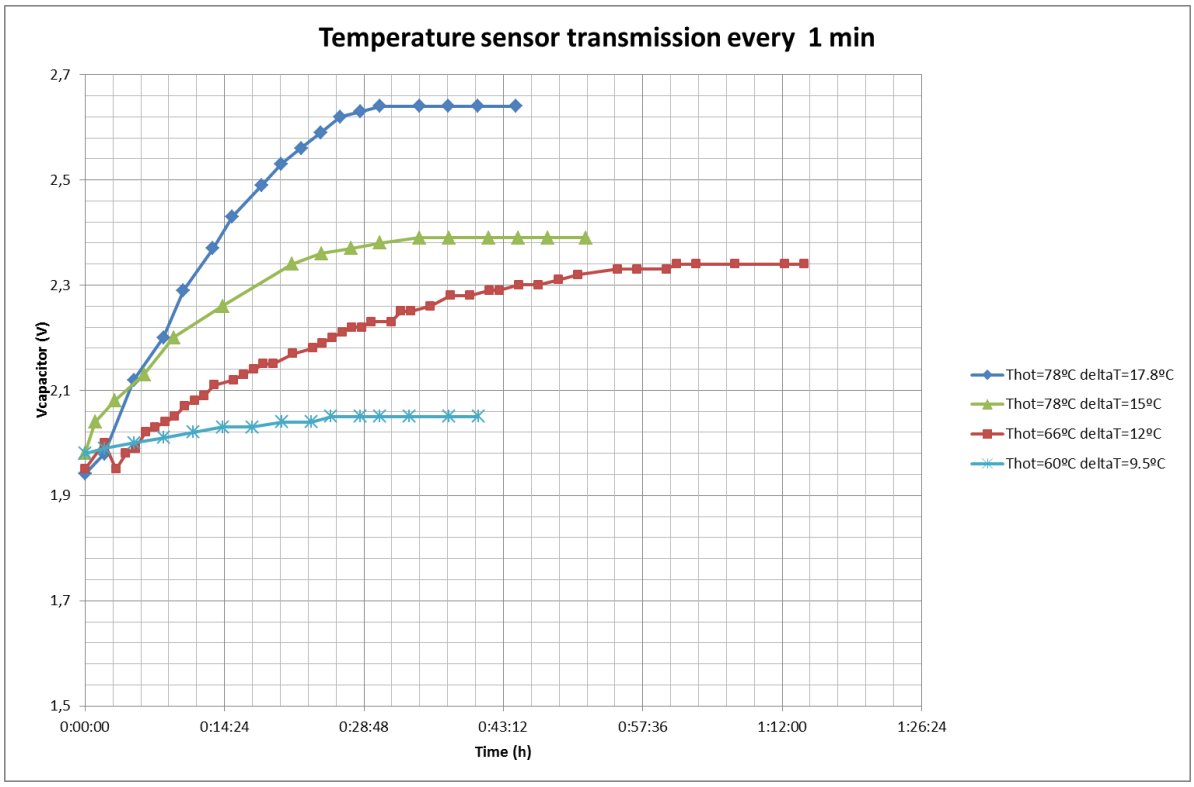

Figure 60: Capacitor voltage as a function of time. Temperature sensor with “Quax DT” node was used. Transmission period was every 1min at different temperature differences.

Therefore, for ΔT= 17.7ºC the supercapacitor was fully charged and the transmission between the sensor node and the gateway was successful, when the temperature difference was lower the maximum voltage reached by the supercapacitor was lower, as Figure 30 shows. However, the transmission of the information was still successful from ΔT= 17.7ºC to ΔT= 9.5ºC. For temperature differences lower than 9.5ºC the transmission of the data was not successful.

6.2.2 "Quax MS" sensor node behaviour

"Quax MS" node (accelerometer sensor) was also used to demonstrate the operation of the system.

The graphs obtained for different temperatures are shown in Figure 61. In this case, the temperatures of the hot side were 78ºC, 70ºC, 66ºC, 63ºC and 60ºC. When the temperature of the cold side was steady, the temperature differences (ΔT) achieved were 15.3ºC, 13ºC, 12ºC, 10.6ºC, 9.9ºC, respectively.

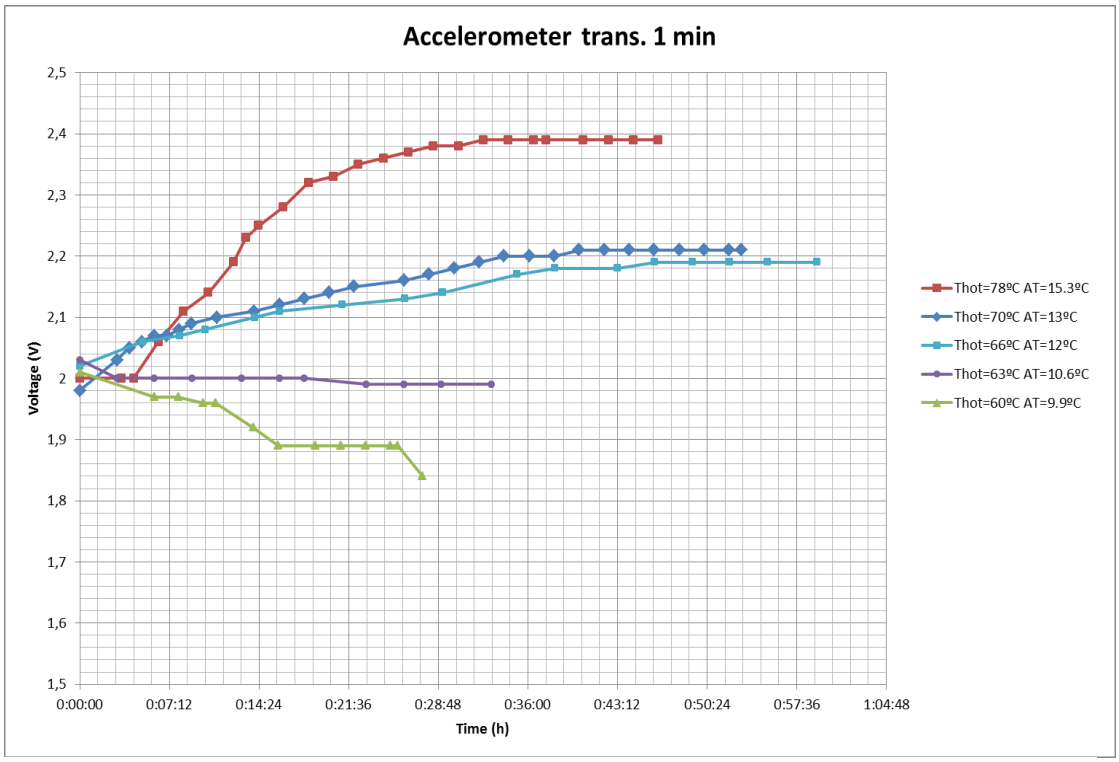

Figure 61: Capacitor voltage as a function of time using "Quax MS" node (accelerometer) transmitting every 1 min at different temperatures.

For ΔT=15.3ºC the capacitor was charged up to 2.4V. When the temperature difference decreases, the capacitor voltage also decreases. The capacitor voltage can be compared in Figure 60 and Figure 61, using “Quax DT” and “Quax MS” nodes. It can be noted that the “Quax MS” node, with the accelerometer consumes more power than the “Quax DT” node, with the temperature sensor. For instance, when ΔT=9.5ºC the capacitor keeps charging up to 2.06V (Figure 60), however for the “Quax MS” sensor with the accelerometer, when ΔT=9.9ºC, the capacitor is discharged very quickly. At ΔT=10.6 ºC, the capacitor seems to maintain the voltage, but it discharges slowly.

From ΔT=12ºC the capacitor starts to charge and the power is enough to transmit the acceleration data every 1 min.

Therefore, for temperature differences (ΔT) lower than 10.6ºC, the sensor node was not capable to send the acceleration data to the gateway, because the thermoelectric does not generate enough energy to charge the capacitor. It demonstrated that the accelerometer consumes more power than the temperature sensor. For ΔT= 9.5ºC, the temperature sensor was able to send the information, however the accelerometer was not able to send the data.

Figure 62 shows the comparison of the “Quax MS” sensor configured to transmit the acceleration only, or to transmit the acceleration and the temperature at the same time. When ΔT=15.3ºC with the sensor node transmitting acceleration only, the capacitor voltage reaches 2.4 V. However, when transmitting temperature and acceleration data, the voltage reached a value of 2.3V, because the power consumption was higher. For a temperature difference of 10ºC the energy generated by the thermoelectric device was not enough to charge the capacitor, thus, by using the “Quax DT” sensor node the capacitor discharged.

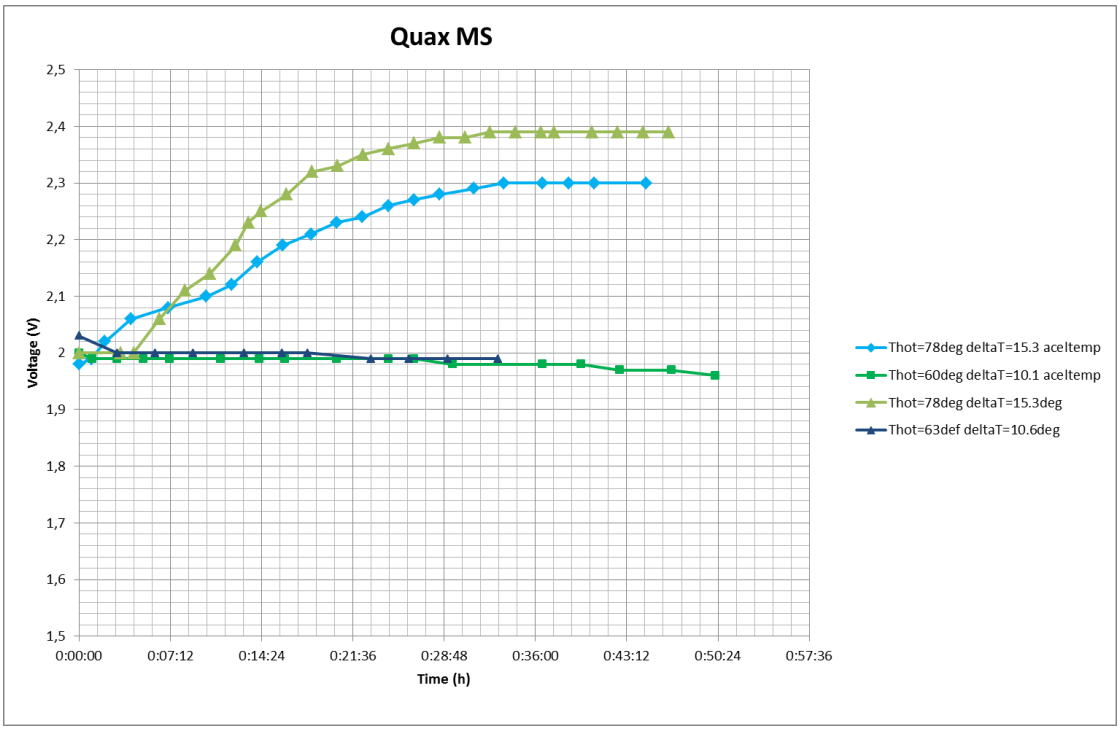

Figure 62: Comparison of the capacitor voltage as a function of time using "Quax MS" node, transmitting every 1 min accelerations, or acceleration and temperatures at different temperatures

6.3 Summary

The operation of the thermoelectric device with the energy harvesting unit connected to a wireless sensor node was studied. The "Quax MS" and "Quax DT" wireless sensors were also tested. Acceleration and temperature data were measured, and by means of the wireless ZigBee protocol were sent to the gateway and to the final user.

In order to check its operation, different temperature differences across the thermoelectric device were tested. The temperature of the hot side was varied and when the temperature of the cold side was constant, the energy harvesting circuit and the sensor node were connected. The interval between sending the data was another variable parameter.

It was noted that if the temperature difference was high enough the capacitor was charged while the sensor sent the data. The “Quax DT” sensor (temperature sensor) worked properly from ΔT=9.5ºC up to ΔT=17.8ºC, when sending data every 1 min. However, the “Quax MS” sensor (accelerometer and temperature sensor) when ΔT= 9.9ºC did not work. From ΔT=12ºC the capacitor started to charge and the sensor sent the acceleration and temperature data. This implies that “Quax MS” sensor has higher power consumption. The period between sending data was varied from 15 seconds to 5 minutes, although there was a difference in the power consumption between them, it was not very significant. Thus, it was concluded that the transmitting frequency was not the unique parameter that affects the power consumption. The sensor was constantly checking that the connection with the gateway was satisfactory.

In conclusion, it has been demonstrated that with a constant temperature difference, higher than 11ºC, the energy harvesting unit, using the thermoelectric device, is capable of powering the sensor node. The sensor node can send the information via wireless (Zigbee protocol) to the gateway and from the gateway to the final user using Wi-Fi.

.

7 TEST RIG CASE STUDY

7.1 Test rig

In this section, the whole system (thermoelectric generator, DC/DC converter, power management unit and sensor node) was tested on a test rig designed to simulate an operating gearbox. The waste heat, due to the friction between different parts, was harnessed from the hottest part of the machine by the thermoelectric generator. The power generated was used to feed the sensor node located in the machine. The installation of the thermoelectric device and the sensor node and the behaviour of the different parts will be studied.

The purpose of the test rig (Figure 63) is to test roller bearings by applying a radial force on the top (Figure 63 b). The test rig allows the rotor speed (rpm) and the applied radial load to be varied. The part where highest temperatures

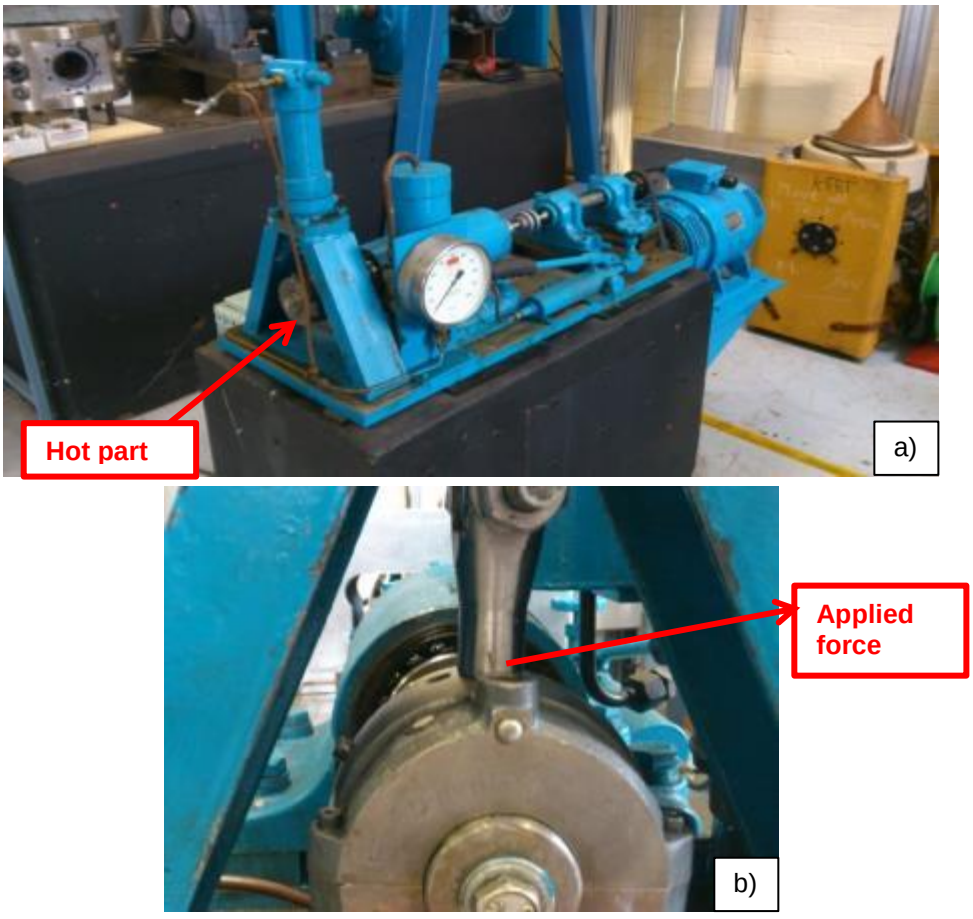

Figure 63: Test rig. a) Hot part of the test rig. Place where the thermoelectric device is located. b) Applied force to the bearings.

were reached is shown in Figure 63 a. Hence, this is the place where the thermoelectric device was placed.

7.2 Method

The place where the waste heat was greatest was first located (Figure 63 a), and thereby the thermoelectric generator was placed here. As Figure 63 a shows, it has cylindrical shape. Thus, the only part of the case where the thermoelectric device could be placed is the flat part. The rounded part is not viable since the thermoelectric harvester is flat and it needs to have as much contact as possible with the case to transmit the heat properly. The thermoelectric generator has dimensions of 40mm x 40mm. However, although the diameter of case is approximately 80mm, only 20 mm of the radium case were available for locating the thermoelectric device, due to the existence of the rotating element.

To overcome this problem, an aluminium plate was attached to the non-mobile part. A thermally insulating material was fixed to the rear part of the aluminium plate to avoid the dissipation of the heat through this part (Figure 64).

Figure 64: Plate attached to the non-mobile part of the bearing casing

The thermoelectric generator was joined to the aluminium plate and to the heat ink with the help of small clamps as shown in Figure 66. In order to cover the

possible air holes between the aluminium plate and the thermoelectric generator and with the heat sink, a non-silicone paste, which allows the heat transfer, was used.

Figure 66: Thermoelectric device and heat sink attached to the casing of the bearings

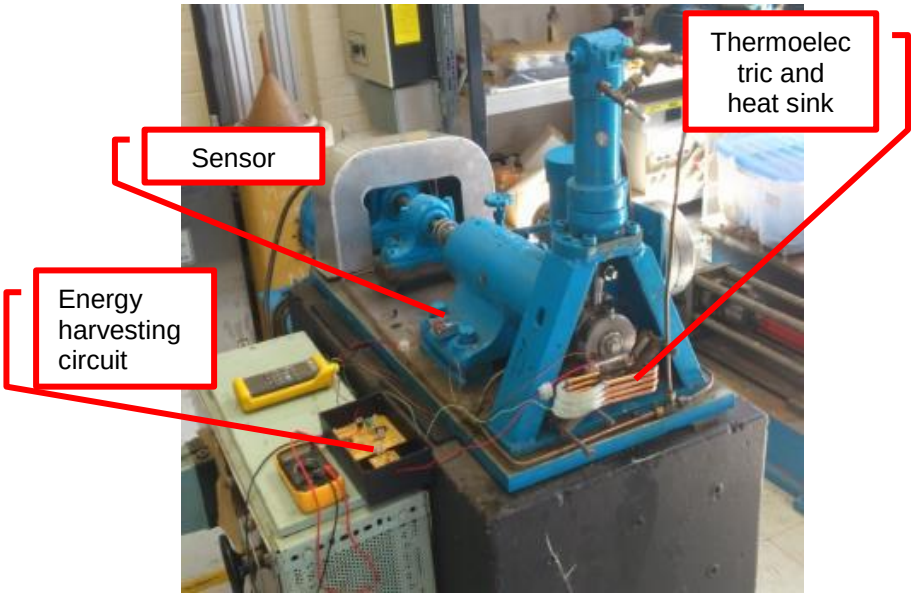

Figure 65: Energy harvester system connected to the sensor node mounted on the test rig.

Once the thermoelectric device was positioned, the “Quax MS” sensor node was attached to the structure to measure vibration and temperature data. Thereby, the connection between the thermoelectric device and the sensor node through the DC/DC converter and the power management unit was established (Figure 65). The “Quax MS” sensor was configured, firstly, to transmit only the acceleration, although, secondly, it was configured to transmit also the temperature.

7.2.1 Procedure

The waste heat harnessed by the thermoelectric device was evaluated for different rotor speeds and the applied load.

The temperatures reached in the bearing casing (hot side of the thermoelectric generator) and the temperatures of the heat sink (cold side) were measured by means of two K-type thermocouples located in both parts. The difference in the temperature between the casing and the aluminium plate was on the order of 1ºC.

The capacitor voltage was measured, by means of a “DIGIFLEX” multimeter, while the sensor was sending the data.

The data received was also recorded by means of the program “PS_Server Data Manipulation” with an excel interface. The data transmission was established as was explained earlier. The data from the sensor was sent to the gateway with Zigbee protocol of communication and from the gateway, the information was sent to the laptop (data receiver) via Wi-Fi (ad-hoc wireless network). Figure 67 shows the locations of the different elements during the experiments.

The experiments were carried out as follows: The machine was switched on with a rotor speed of 2800 rpm and an applied pressure of 3.45 MPa. When the bearing casing achieved a temperature of 95ºC, the machine was switched off in order to cool it down. When the temperature of the casing reached 50ºC, the

machine was turned on again (2000 rpm and 2.07 MPa) until the temperature of the casing was again 95ºC. Subsequently, the casing cooled down reaching 50ºC. Finally, the machine was turned on (2000 rpm, 0.76 MPa) when it achieved a temperature of 95ºC, it was turned off, letting the machine cool down. The temperature of 95ºC was chosen in order to avoid damage to the thermoelectric harvester. The heating and the cooling rate of the bearing are shown in Appendix D. During this time (approximately 3 hours), temperature and accelerations were measured and sent to the receiver (laptop).

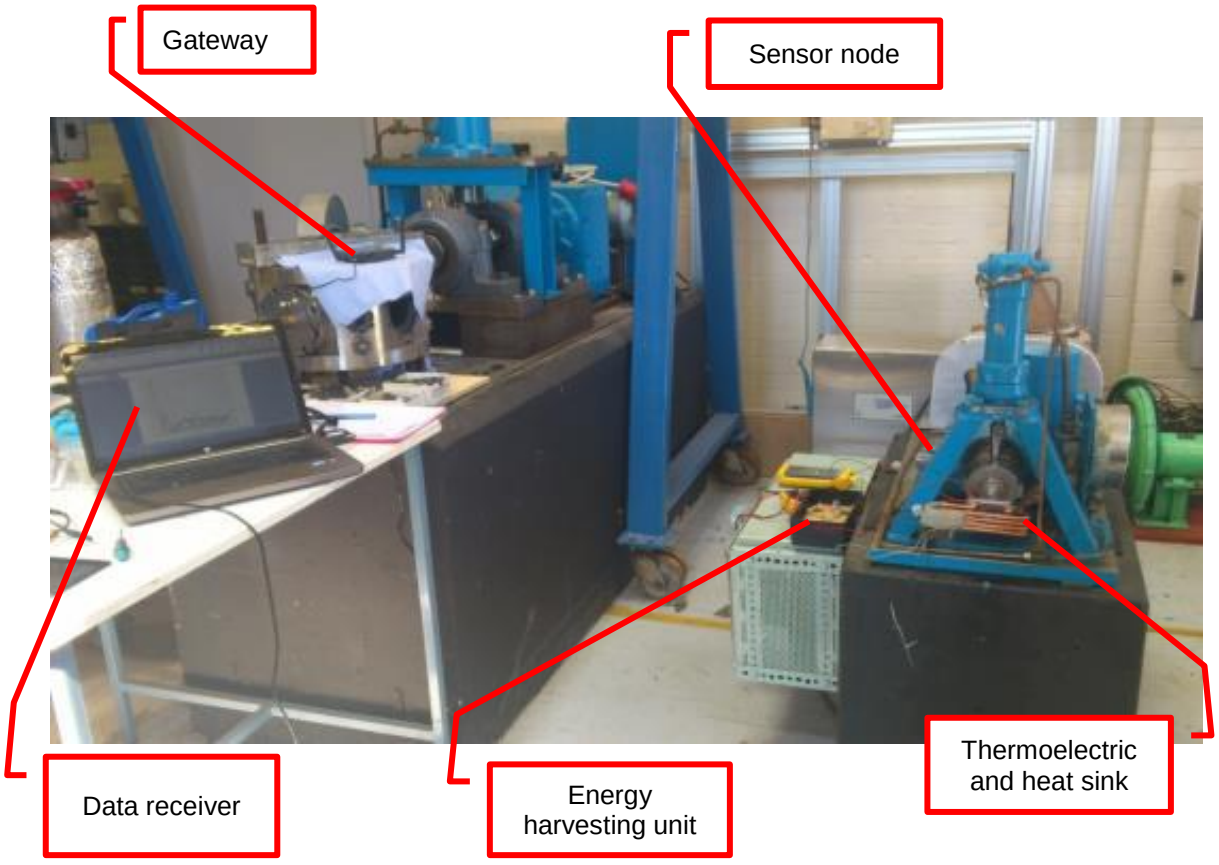

Figure 67: Overview of energy harvesting system utilising waste heat emitted from the casing of the bearing.

7.3 Results and discussion

In the first place, it is necessary to determine the temperatures reached in both sides of the thermoelectric device (hot side and cold side) during test runs.

Figure 68 shows the variation of the temperature of the hot side as a function of the temperature at the cold side, for the test rig (chapter 7) and for the lab bench test (chapter 0). The main difference between the lab bench test and test rig is that in lab bench test, the thermoelectric generator worked in a steady state, while in test rig, the steady state was never achieved. The temperature of the bearing casing was always increasing until it reached a temperature of 95ºC when it was turned off. Thus, the temperature difference experienced in the lab bench test (left line (rhombus-shaped markers) in Figure 68) was lower than the experiment in the test rig at different rotor speed and loads. The cold side did not have enough time to achieve the steady state conditions. For this reason, the temperature difference in the test rig was higher.

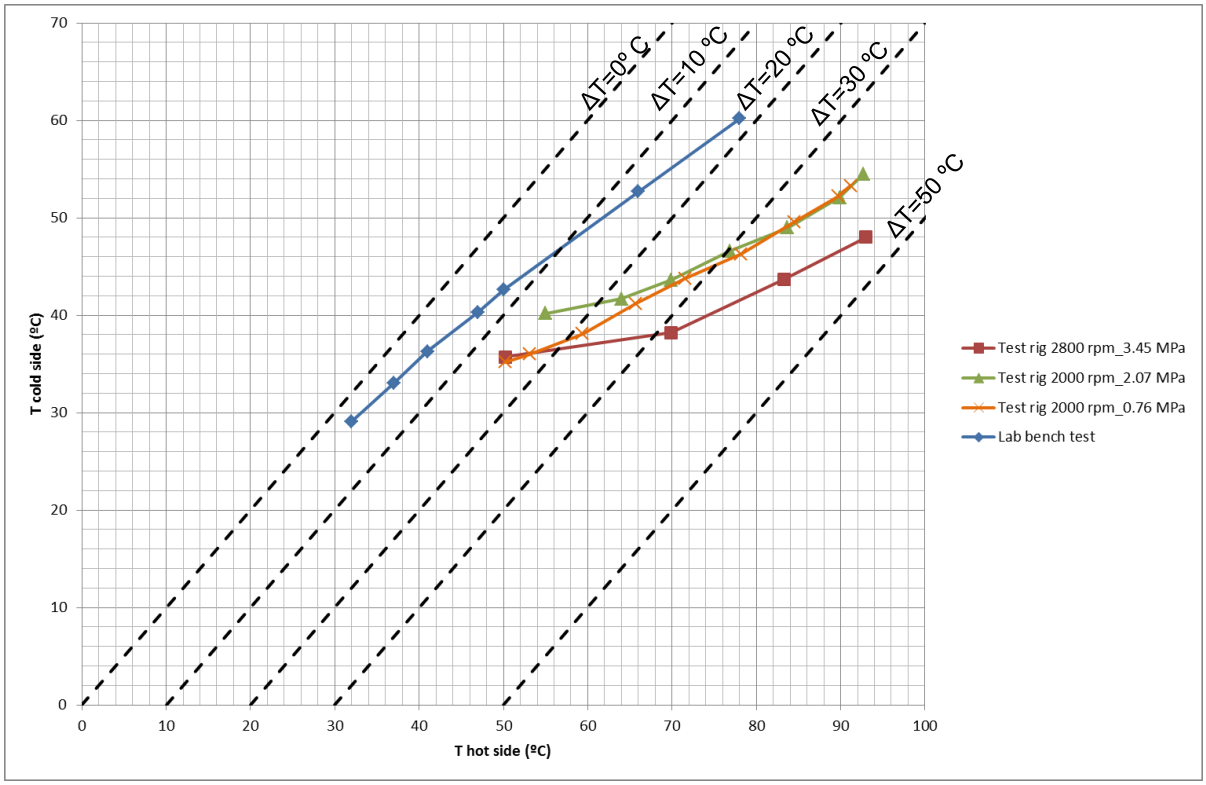

Figure 68: Temperature of the cold side as a function of the temperature of the cold side of the TEG for steady state conditions (lab bench test) and non-equilibrium condition test rig. Trials at different speed

The capacitor voltage of the charge and discharge was measured and is depicted in Figure 68. The machine was switched on with a rotor speed of 2800 rpm and an applied force of 3.45 MPa (triangle-shaped markers in Figure 69), the capacitor reached a voltage of 2.25 V, when the temperature of the bearing casing reached 95ºC. Then, it increased up 2.45V and the capacitor started to discharge although, the difference temperature was still high (approximately 20ºC). When the temperature reached 50ºC, the machine was turned on again (2000 rpm and 2.07 MPa), causing an increase in the temperature to 95ºC (rhombus-shaped markers), and the capacitor was charged up to 2.3V. The phenomenon of discharge occurred again. Finally, when the temperature of the casing reached 50ºC, the machines was turned on (2000rpm, 0.76 MPa) (circle-shaped markers) and the capacitor reached 2.35V, repeating the same behaviour of charge and discharge. Lastly, the machine cooled down until the sensor node stopped transmitting (1.71V).

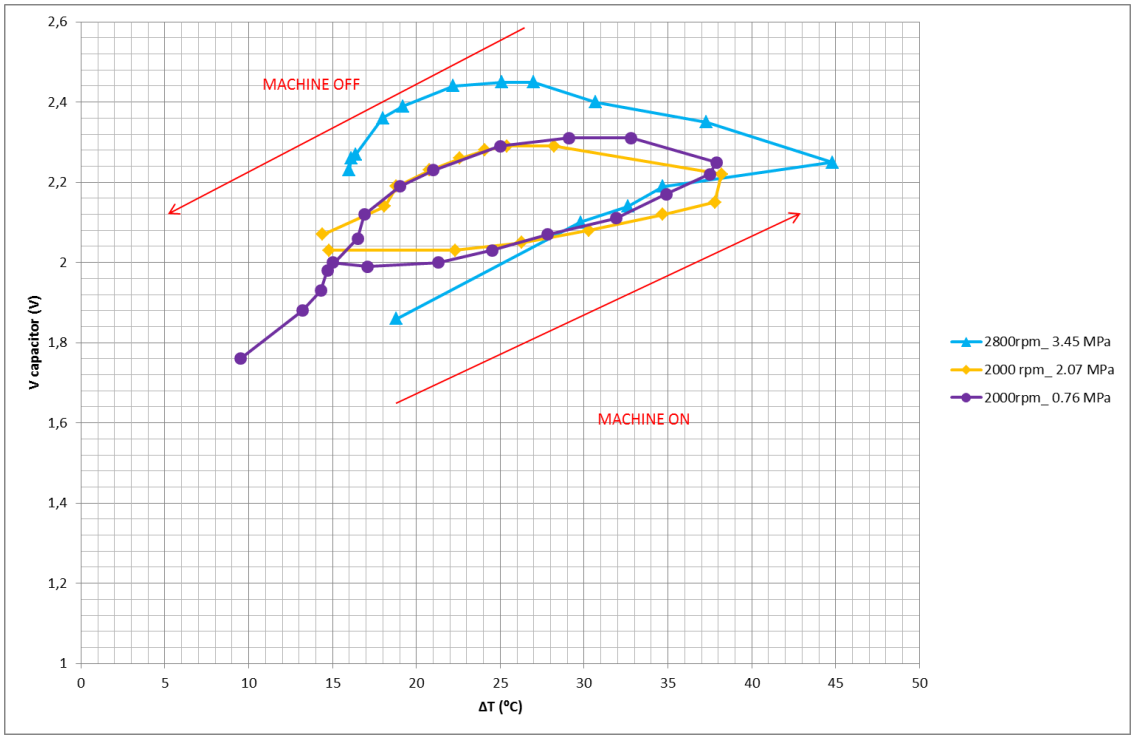

Figure 69: Capacitor voltage in the charge and discharge as a function of the temperature difference across the thermoelectric device

Several aspects of the behaviour depicted in Figure 69 have to be commented on. The first aspect is the loop shape of the curves and the fact that for the same temperature difference the capacitor voltage is different. The reason is that not only the temperature difference has influence over the power generation of the thermoelectric harvester. The fact that the machine is heating stage or cooling stage is the main reason of this phenomenon. Besides the conditions achieved in the thermoelectric device are not steady state conditions. When the machine is heating the capacitor is charged, when the machine is off the capacitor keeps charging but at difference rate, the machine starts to cool, and the capacitor is discharged through DC/DC converter. In order to solve this problem, a diode can be introduced between the DC/DC converter and the power management circuit, but the voltage would drop at least 0.6V. The capacitor would be barely charged and the duration of the operation of the node would decrease extremely.

The second aspect is that for instance, with a temperature difference of almost 38ºC, the voltage of the capacitor is 2.25V, however in the lab bench test (chapter 0), with ΔT=17.7ºC the capacitor was fully charged. It is due to the machine did not work in steady state conditions, the DC/DC converter needs to work with a stable temperature difference in order to avoid the variation in its main output.

Likewise, Figure 70 depicts the capacitor voltage as a function of the test rig operation time. The capacitor was charging and discharging during the operation time for 3 hours. When the machine was switched on the capacitor charged, but not until the maximum value, when the machine switched off the capacitor kept charging until the machine started to cool down, from this point the capacitor started to discharge. In Figure 70 and Figure 71 the different stages of the machine operation are indicated, when it was on and off and the different speed and pressure applied.

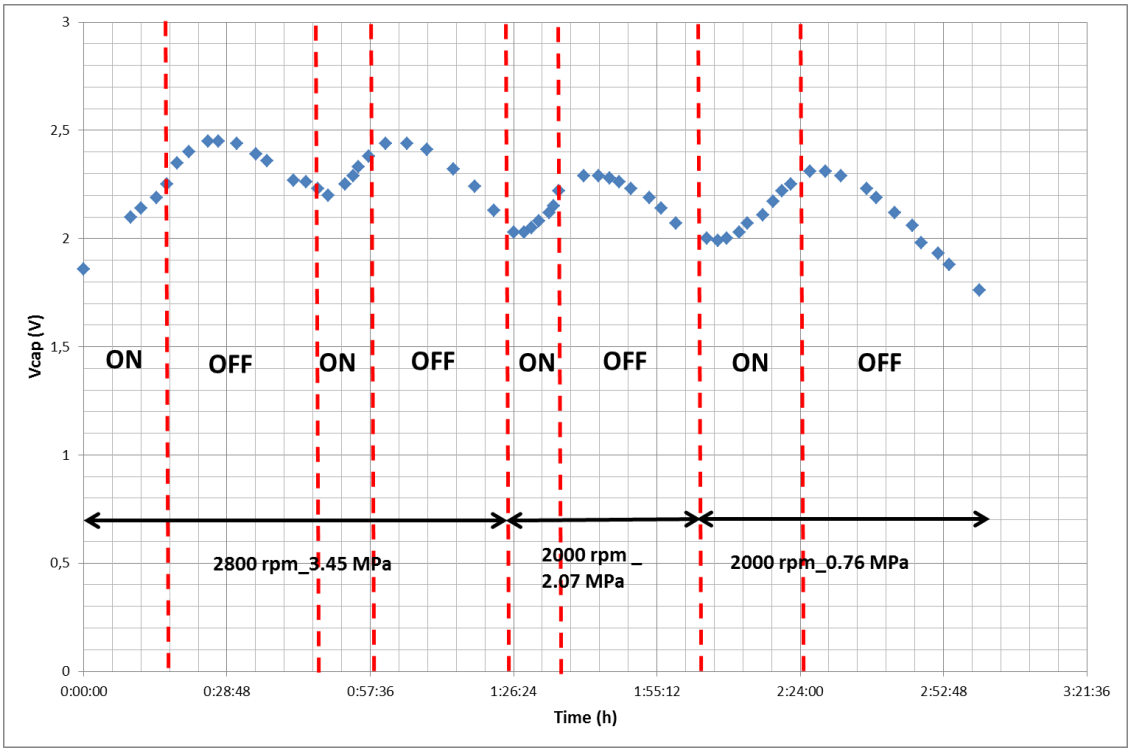

Figure 70: Capacitor voltage as a function of the time operation of the test rig

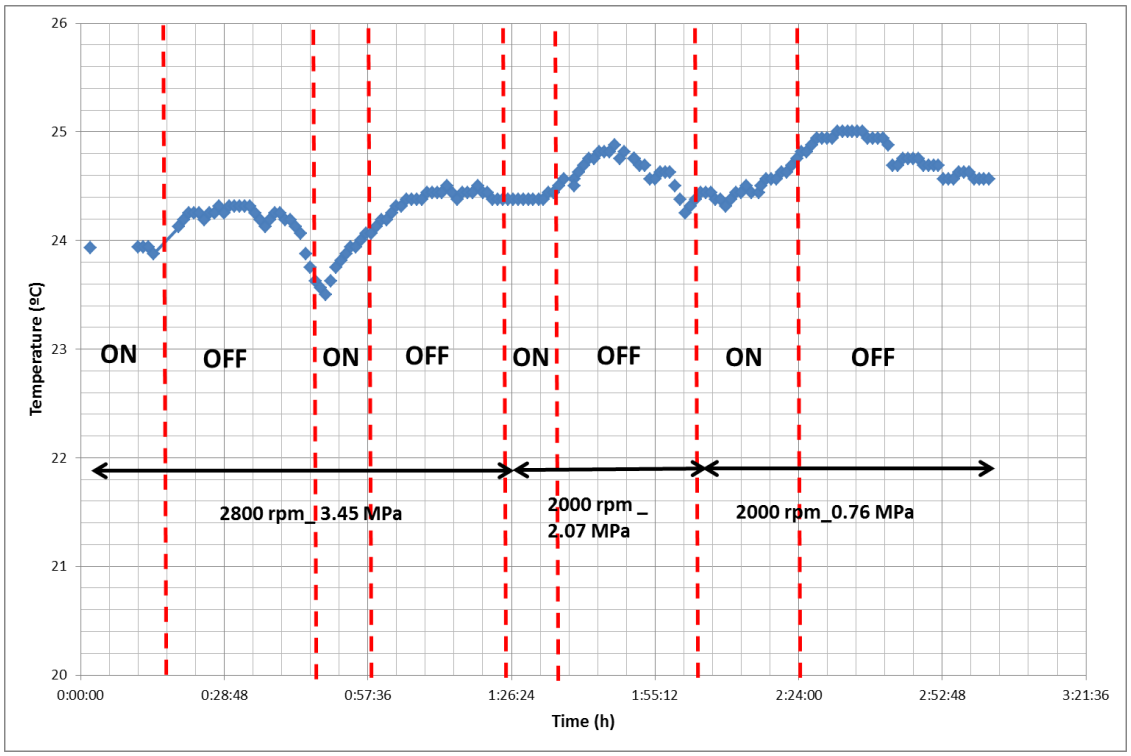

Figure 71: Temperature measured by the "Quax MS" sensor node during the monitoring period

The temperature and the accelerations measured during this period are shown in Figure 71 and Figure 72 The temperature monitored shows the peaks in the temperature when the machine was on and off. Finally when the machine was off the temperature was decreasing, but obviously it was higher than at the beginning of the experiment.

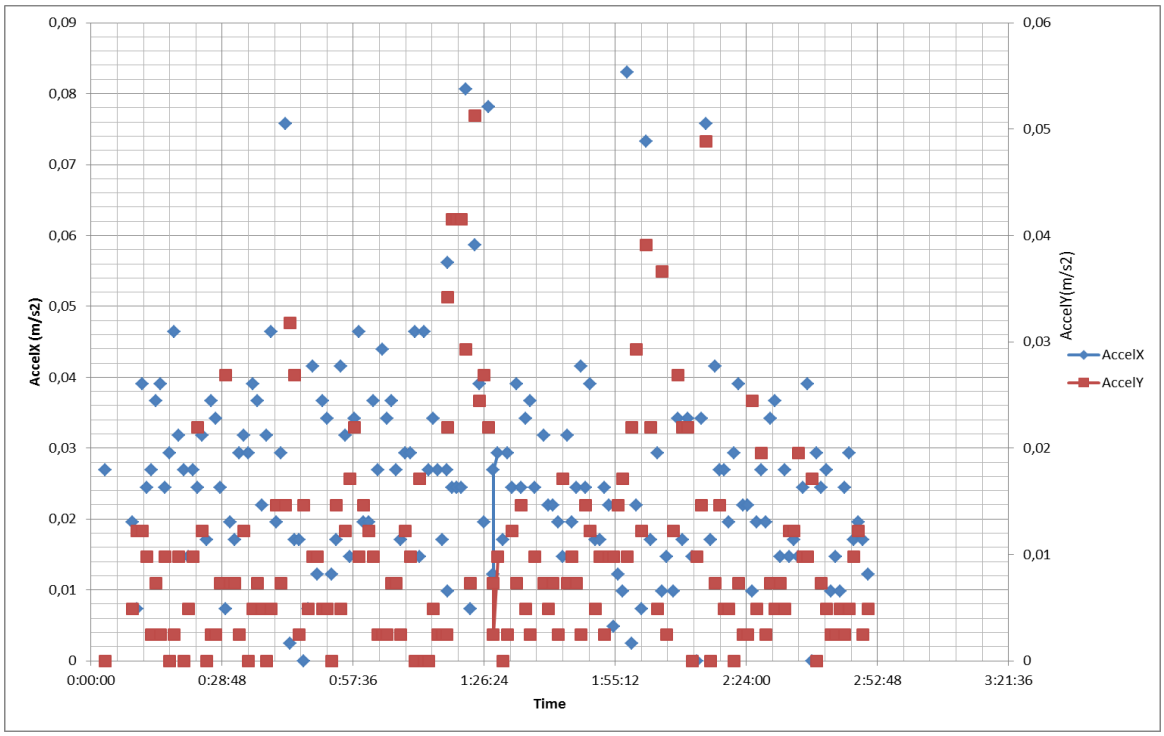

Figure 72: Acceleration measured by the "Quax MS" sensor node during the monitoring period

7.4 Summary

The energy harvesting system operation using the waste heat of a real machine was tested. The thermoelectric generator was placed on the bearing casing and the sensor node located on the structure of the machine. The sensor node sent the data (temperature and acceleration) via wireless to the final user (laptop). Zigbee protocol was used to send the information to the gateway and Wi-Fi was used to send the information from the gateway to the laptop (data receiver). The experiment was running for approximately three hours. During this time, the

waste heat from the bearing casing was enough to charge the capacitor and allow the data to be sent via wireless protocol to the final user.

The behaviour of the test rig with respect to the lab bench test was different. In the lab bench test (see chapter 0), the temperature difference was steady and from ΔT=12ºC the capacitor started to charge, powering the sensor. However, for the test rig, the temperature difference was achieved for a non-steady state condition. It was observed that for the same temperature difference, the capacitor was discharged or charged. When the machine heated up, the capacitor was charging at certain temperature difference. However, for the same temperature difference, if the machine was cooled down, the capacitor was discharged. In conclusion, although the temperature difference is high enough to charge the capacitor, the machine has to heat up. The DC/DC converter should act as a diode to reduce the discharge of the capacitor, but in this casing, the DC/DC converter decreases the time of discharge. One solution is to place a diode between the DC/DC converter and the power management unit, but the voltage reached would be 0.6V less than the one reached without it. That means the capacitor would take more time to charge and the maximum voltage achieved would be lower.

Hence, the different conditions, such as steady-state conditions, non-steady conditions or if the heat generator is heating up or cooling down, has to be taken into consideration, in order to study the voltage generation with waste heat using thermoelectric harvesters.

8 CONCLUSIONS AND FUTURE WORK

The purpose of this project was to demonstrate the operation of a self-powered short range wireless sensor node. Sensor nodes collect the data from the different components, inside the tidal turbine nacelle, to monitor the condition of these components. Among all the sources of energy that can be found in the nacelle of the turbine, waste heat from the components was chosen. The waste heat was harnessed by thermoelectric generators.

Wireless sensor nodes use the Zigbee communication protocol. This protocol is characterized by its low power consumption. The nodes send the information to the gateway and from the gateway, via Wi-Fi, the data are received by the final user.

The next step was to determine the power capabilities of the thermoelectric device. For this reason a commercial thermoelectric harvester was tested. The maximum voltage measured without load connected was approximately 800 mV at a temperature difference of 25ºC. On the other hand, if a load was connected, the voltage reached was 520mV and the maximum power was approximately 30 mW for a temperature difference of 17.7ºC.

Once, the thermoelectric generator was studied, the power of the sensor node was measured. The power consumption, when the node was sleeping, was roughly 5 mW for “Quax MS” sensor node and 1mW for “Quax DT” sensor node. When the node was transmitting the power consumption measured was more than 100mW. When the maximum temperature difference of 17.7ºC was reached in the laboratory, the thermoelectric device could power the sensor node when is sleeping, but during the transmission an energy support was needed.

In order to cover the gap between the thermoelectric device and the sensor node, a power management unit was constructed. The power management unit is an analog circuit, whose energy storage is a 10F capacitor. Moreover, to adapt the voltage from the thermoelectric generator to the sensor node a

DC/DC converter was utilized. The power management unit charges the capacitor and at the same time, it feeds the sensor.

The final objective of this thesis was to test the concept of operation of the whole system (thermoelectric generator, power management unit and sensor node). Thus, two different experiments were carried out.

The lab bench trial utilized a hot plate to heat the hot side of the thermoelectric device. The sensor node was connected when the temperatures of the cold and hot side were steady. From a ΔT=10ºC, the “Quax DT” sensor node (temperature sensor) worked with the thermoelectric generator connected, charging the capacitor and powering the sensor. Although, capacitor charging was very slow. The maximum temperature difference attained was 17.7ºC, the capacitor was fully charged and the node transmitted the data successfully. However, using the “Quax MS” sensor (accelerometer and temperature sensor), ΔT=10ºC was not enough temperature difference to charge the capacitor. From ΔT=12ºC, the system started to work properly. Thus, for the lab bench test, it was concluded that from certain temperature difference the system worked correctly. If the temperature difference was higher, the capacitor voltage reached was also higher.

In the test rig trial, a real machine was utilized as a heat source. The test rig is used to test roller bearing when a radial force is applied. When the applied force was higher, the waste heat from the machine was higher. The thermoelectric generator was attached to the hot part of the bearing casing. Thereby, the thermoelectric device was connected to the power management unit and the sensor node also placed on the machine. The machine was running and the thermoelectric generator using the waste heat generated enough energy to power the sensor and charge the capacitor. However, the conditions, in this casing, were not steady (the temperatures of the cold and hot side were variable). When the machine was on, the capacitor was charging for a certain temperature difference. However, when the machine was switched off, and cooling down, for the same temperature difference, the capacitor discharged. Thus, it was concluded that, besides the temperature difference, the fact of the

machine heats up or cooled down was crucial. When the machine was cooling down, the capacitor was discharged through the DC/DC converter as well. One solution would be to locate a diode between the DC/DC converter and the power management unit, however, the drop of the voltage would be too high (0.6 V) for this application. In order to improve the efficiency of the system, a variable maximum power point should be implemented in the DC/DC converter. Nevertheless, if a microprocessor is utilized the energy consumption will be very high. Moreover, it has to be designed for each application, because the temperature difference has to be perfectly defined, as well as the power generated.

The main aim of this project was to study the viability of the use of a wireless sensor node powered by thermoelectric generators as energy harvesters. It was focused on the communication inside the nacelle, where the communication protocol followed was the Zigbee protocol. However, the communication from the nacelle to shore must be established. As electromagnetic waves do not transmit information through the water, the communication will rely on acoustic waves.

Thereby, for the future work several aspects have to be specified:

- The communication inside the turbine is guaranteed using a land protocol for communication. Hence, the future work will study the development of another gateway that will be able to send the information via acoustic waves to another gateway (acoustic receiver) placed on a platform on the sea. The acoustic receiver will be connected to one antenna on the platform, which will send the data from the platform on the sea to the land. The latter communication will rely on electromagnetic waves, more powerful than acoustic waves in the air (WiFi, GPRS, Bluetooth…). Therefore, the communication of the whole system will be wireless, without the necessity of using cables, whose maintenance is highly costly. A schematic of the system explained can be seen in Figure 73.

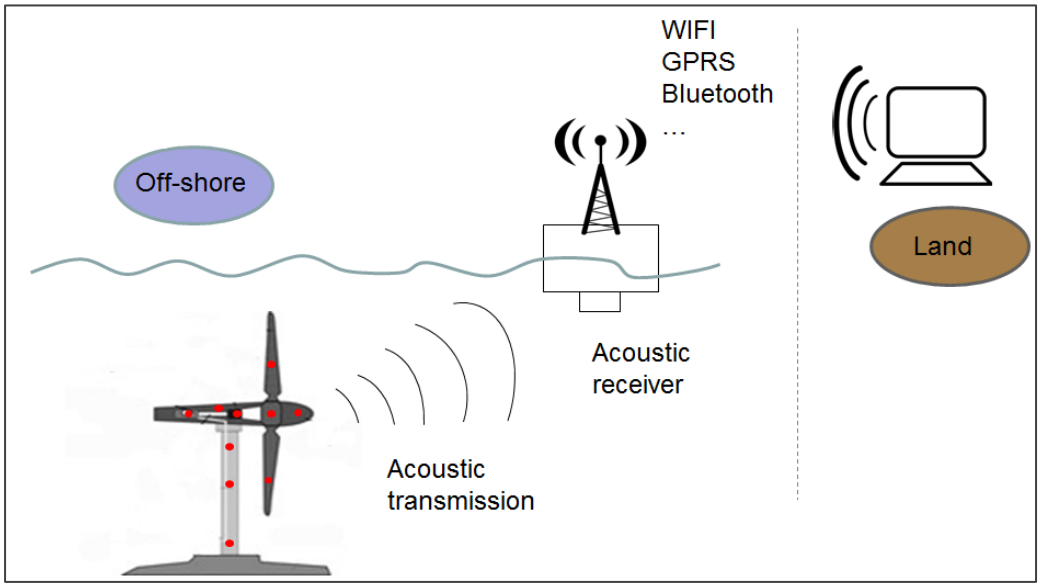

Figure 73: Schematic of the communication between the sensor nodes in the turbine and the land station.

- In this thesis PrismaSense wireless sensor nodes were used. However, the power consumption of these sensors, particularly, is relatively high when they work in the sleeping mode (when there is not transmission). Another aspect of the future work is to study how to minimize the power consumption of these sensor nodes, or another solution is to substitute these sensors by other sensor nodes with low power consumption.

- The thermoelectric generator greatly depends on the temperature of the machine where it is located. A better study of the temperature of the different parts of the turbine as well as the variation of the temperature during their operation must be done.

- Finally, a really important part of a thermoelectric generator is the heat sink that is attached to it. The purpose of the heat sink is to increase the temperature difference between the hot side and the cold side to

increase the power generated. The heat sink used in this project was four copper and plastic tubes with water inside attached to a copper plate on the cold side of the thermoelectric device. The operation of this heat sink can be maximized if the behaviour of the environment inside the nacelle under the water is carefully studied.

REFERENCES

[1] United Nations (1998), "Kyoto Protocol to the United Nations Framework Convention on Climate Change".

[2] European comission (May 2013), *A new directive on Energy Efficiency*, available at:http://ec.europa.eu/energy/efficiency/eed/doc/2011_directive/20110622_energy_efficiency_directive_slides_presentation_en.pdf.

[3] Benoit, M., Mattarolo, G. and Dhédin J-F (2010), *Energies marines hydrolienne et houlomotrice. Exemples de projets et de travaux de R&D*, available at: http://www.coriolis.polytechnique.fr/Confs/Benoit_conf.pdf (accessed May 2013).

[4] Green Tidal Turbines Limited (2012), *Market potential for Green Tide*, available at: http://green-tide.org/market/ (accessed May 2013).

[5] Thusu, R. (2010), *Wireless Sensor Use Is Expanding in Industrial Applications. Sensors Magazine*, available at: http://www.sensorsmag.com/networking-communications/wireless-sensor/wireless-sensor-use-is-expanding-industrial-applications-7212 (accessed 12/07/2012).

[6] Frank, R. (April 2012), *Energy harvesting for sensors*, available at: http://www.sensorsmag.com/sensors-mag/energy-harvesting-sensors-9748 (accessed 12/07/2012).

[7] Delta Stream Limited, (2009), *Delta Strema Demonstrator project, Ramsey Sound. Non-technical summary.*

[8] Jardine, A. K. S., Lin, D. and Banjevic, D. (2006), "A review on machinery diagnostics and prognostics implementing condition-based maintenance", *Mechanical Systems and Signal Processing,* vol. 20, no. 7, pp. 1483-1510.

[9] Walters, R. A., Tarbotton, M. R. and Hiles, C. E. (2013), "Estimation of tidal power potential", *Renewable Energy,* vol. 51, no. 0, pp. 255-262.

[10] Mitcheson, P. D., Yeatman, E. M., Rao, G. K., Holmes, A. S. and Green, T. C. (2008), "Energy harvesting from human and machine motion for wireless electronic devices", *Proceedings of the IEEE,* vol. 96, no. 9, pp. 1457-1486.

[11] Khan, M. J., Bhuyan, G., Iqbal, M. T. and Quaicoe, J. E. (2009), "Hydrokinetic energy conversion systems and assessment of horizontal and vertical axis turbines for river and tidal applications: A technology status review", *Applied Energy,* vol. 86, no. 10, pp. 1823-1835.

[12] Sea Generation Ltd., *Sea Generation Ltd.*, available at: http://www.seageneration.co.uk/ (accessed April 2013).

[13] Douglas, C. A., Harrison, G. P. and Chick, J. P. (2008), "Life cycle assessment of the Seagen marine current turbine", *Proceedings of the Institution of Mechanical Engineers Part M: Journal of Engineering for the Maritime Environment,* vol. 222, no. 1, pp. 1-12.

[14] Stables, M., *Tidal Stream Background Information*, available at: http://www.engineering.lancs.ac.uk/lureg/renewable_energy/tidal_stream.php (accessed May 2013).

[15] Calcagno, G. and Moroso, A. (2007), *The Kobold marine turbine: from the testing model to the full scale prototype*, available at: http://www.tidaltoday.com/tidal07/presentations/GuidoCalcagnoMoroso.pdf (accessed May 2013).

[16] Lunar energy Ltd (2010), *Lunar Energy, harnessing tidal power*, available at: http://www.lunarenergy.co.uk/ (accessed April 2013).

[17] atlantisstrom (2004), *Atlantisstrom*, available at: http://www.atlantisstrom.de/ (accessed May 2013).

[18] Huw David Design (2012), *Eco2*, available at: http://www.eco2uk.com/en/our_projects/project_detail.asp?project_id=13 (accessed 09/2012).

[19] DeltaStream, (2012), *DeltaStream Tidal Energy Solution*, Tidal Energy Limited, Cardiff.

[20] , *Prisma Sense* (2013), available at: http://www.prismaelectronics.eu/site/index.php?option=com_content&view=article&id=226&Itemid=651&lang=en (accessed 12/04/2013).

[21] Song, E.Y. and Lee, K.B., (2010), *IEEE 1451.5 standard-based wireless sensor networks*.

[22] Heidemann, J., Ye, W., Wills, J., Syed, A. and Li, Y. (2006), "Research challenges and applications for underwater sensor networking", *IEEE Wireless Communications and Networking Conference, WCNC,* Vol. 1, pp. 228.

[23] Heckman, A., Rovey, J. L., Chandrashekhara, K., Watkins, S. E., Mishra, R. and Stutts, D. (2012), "Ultrasonic underwater transmission of composite turbine blade structural health", *Proceedings of SPIE - The International Society for Optical Engineering,* Vol. 8343.

[24] Heidemann, J., Stojanovic, M. and Zorzi, M. (2012), "Underwater sensor networks: Applications, advances and challenges", *Philosophical Transactions of the Royal Society A: Mathematical, Physical and Engineering Sciences,* vol. 370, no. 1958, pp. 158-175.

[25] Xiao, Y. (2010), *Underwater acoustic sensor networks,* Auerbach Publications, Boca Raton.

[26] Wills, J., Ye, W. and Heidemann, J. (2006), "Low-power acoustic modem for dense underwater sensor networks", *WUWNet 2006 - Proceedings of the First ACM International Workshop on Underwater Networks,* Vol. 2006, pp. 79.

[27] Benson, B., Li, Y., Kastner, R., Faunce, B., Domond, K., Kimball, D. and Schurgers, C. (2010), "Design of a low-cost, underwater acoustic modem for short-range sensor networks", *OCEANS'10 IEEE Sydney, OCEANSSYD 2010.*

[28] Lu, C., Wang, S. and Tan, M. (2008), "Design and realization of sensor nodes for dense underwater wireless sensor networks", *IFAC Proceedings Volumes (IFAC-PapersOnline),* Vol. 17.

[29] Sanchez, A., Blanc, S., Yuste, P. and Serrano, J. J. (2011), "A low cost and high efficient acoustic modem for underwater sensor networks", *OCEANS 2011 IEEE - Spain.*

[30] Macias, E., Suarez, A., Chiti, F., Sacco, A. and Fantacci, R. (2011), "A hierarchical communication architecture for oceanic surveillance applications", *Sensors,* vol. 11, no. 12, pp. 11343-11356.

[31] Chalasani, S. and Conrad, J. M. (2008), "A survey of energy harvesting sources for embedded systems", *Southeastcon, 2008. IEEE,* pp. 442.

[32] Elvin, N. G. and Elvin, A. A. (2011), "An experimentally validated electromagnetic energy harvester", *Journal of Sound and Vibration,* vol. 330, no. 10, pp. 2314-2324.

[33] Vullers, R. J. M., van Schaijk, R., Doms, I., Van Hoof, C. and Mertens, R. (2009), "Micropower energy harvesting", *Solid-State Electronics,* vol. 53, no. 7, pp. 684-693.

[34] Beeby, S. P., Tudor, M. J. and White, N. M. (2006), "Energy harvesting vibration sources for microsystems applications", *Measurement Science and Technology,* vol. 17, no. 12, pp. R175-R195.

[35] Pereyma, M. (2007), "Overview of the Modern State of the Vibration Energy Harvesting Devices", *Perspective Technologies and Methods in*

MEMS Design, 2007. MEMSTECH 2007. International Conference on, pp. 107.

[36] Glynne-Jones, P., Tudor, M. J., Beeby, S. P. and White, N. M. (2004), "An electromagnetic, vibration-powered generator for intelligent sensor systems", *Sensors and Actuators A: Physical,* vol. 110, no. 1–3, pp. 344-349.

[37] Worthington, E. L., Zhu, M., Kirby, P. and Cranfield University. School of applied sciences (2010), *Piezoelectric energy harvesting: enhancing power output by device optimisation and circuit techniques.*

[38] Torres, E. O. and Rincón-Mora, G. A. (2009), "Electrostatic energy-harvesting and battery-charging CMOS system prototype", *IEEE Transactions on Circuits and Systems I: Regular Papers,* vol. 56, no. 9, pp. 1938-1948.

[39] Paradiso, J. A. and Starner, T. (2005), "Energy scavenging for mobile and wireless electronics", *IEEE Pervasive Computing,* vol. 4, no. 1, pp. 18-27.

[40] Mukhopadhyay, S.C., Leung, H. and SpringerLink, (2010), *Advances in wireless sensors and sensor networks*, Springer-Verlag, Berlin ; Heidelberg.

[41] Pobering, S. and Schwesinger, N. (2008), "Power supply for wireless sensor systems", *Sensors, 2008 IEEE,* pp. 685.

[42] Humdinger Wind Energy, L. (2010), *http://www.humdingerwind.com/#/wi_overview/*, available at: http://www.humdingerwind.com (accessed 29/06/2012).

[43] Wachutka, G. and Gerstenmaier, Y. (2006), "Thermoelectric and thermionic microgenerators: Chances, challenges and limitations", *Proceedings of the International Conference on Mixed Design of Integrated Circuits and Systems, MIXDES 2006,* pp. 48.

[44] Priya, S. and Inman, D. J. (2008), *Energy harvesting technologies,* Springer, New York ; London.

[45] Ryan, M. A. and Fleurial, J. -. (2002), "Where there is heat, there is a way: Thermal to electric power conversion using thermoelectric microconverters", *Electrochemical Society Interface,* vol. 11, no. 2, pp. 30-33.

[46] Goupil, C., Seifert, W., Zabrocki, K., Müller, E. and Snyder, G. J. (2011), "Thermodynamics of thermoelectric phenomena and applications", *Entropy,* vol. 13, no. 8, pp. 1481-1517.

[47] Snyder, G. J. and Ursell, T. S. (2003), "Thermoelectric efficiency and compatibility", *Physical Review Letters,* vol. 91, no. 14, pp. 148301/1-148301/4.

[48] Seifert, W., Ueltzen, M. and Müller, E. (2002), "One-dimensional modelling of thermoelectric cooling", *Physica Status Solidi (A) Applied Research,* vol. 194, no. 1, pp. 277-290.

[49] Snyder, G. J. and Toberer, E. S. (2008), "Complex thermoelectric materials", *Nature Materials,* vol. 7, no. 2, pp. 105-114.

[50] Ursell, T. S. and Snyder, G. J. (2002), "Compatibility of segmented thermoelectric generators", *Thermoelectrics, 2002. Proceedings ICT '02. Twenty-First International Conference on,* pp. 412.

[51] Agilent Technologies Inc. (January 2013)*, Agilent digital multimeters*, available at: http://cp.literature.agilent.com/litweb/pdf/5990-5315EN.pdf (accessed April 2013).

[52] Texas Instruments *, Microcontrollers (MCU) MSP430*, available at: http://www.ti.com/lsds/ti/microcontroller/16-bit_msp430/getting_started.page (accessed 07/04/2012).

[53] Shinghal, K., Noor, A., Srivastava, N. and Singh R. (2011), "Power Measurements of Wireless Sensor Network Node", *International Journal of Computer Engineering & Science,* vol. 1, no. 1, pp. 8-8-13.

[54] Lu, C., Raghunathan, V. and Roy, K. (2010), "Micro-scale energy harvesting: A system design perspective", *Proceedings of the Asia and South Pacific Design Automation Conference, ASP-DAC,* pp. 89.

[55] Lu, X. and Yang, S. -. (2010), "Thermal energy harvesting for WSNs", *2010 IEEE International Conference on Systems, Man and Cybernetics, SMC 2010,* 10 October 2010 through 13 October 2010, Istanbul, pp. 3045.

[56] Lu, X. and Yang, S. -. (2009), "Solar energy harvesting for zigbee electronics", *Sustainability in Energy and Buildings - Proceedings of the International Conference in Sustainability in Energy and Buildings, SEB'09,* pp. 19.

[57] Dalola, S., Ferrari, M., Ferrari, V., Guizzetti, M., Marioli, D. and Taroni, A. (2009), "Characterization of thermoelectric modules for powering autonomous sensors", *IEEE Transactions on Instrumentation and Measurement,* vol. 58, no. 1, pp. 99-107.

[58] Ferrari, M., Ferrari, V., Guizzetti, M., Marioli, D. and Taroni, A. (2007), "Characterization of thermoelectric modules for powering autonomous

sensors", *Conference Record - IEEE Instrumentation and Measurement Technology Conference,* .

[59] Doms, I., Merken and Van Hoof, C. (2007), "Comparison of DC-DC-converter architectures of power management circuits for thermoelectric generators", *Power Electronics and Applications, 2007 European Conference on,* pp. 1.

[60] Linear Technology, (2010), *LTC3105 400mA Step-Up DC/DC Converter with Maximum Power Point Control and 250mV Start-Up*, Linear Technology Coorporation, Milpitas, California, USA.

[61] Cooper Bussmann, (2012), *Supercapacitors HV Series*.

[62] Maxwell Technologies, I. (2013)*, Ultracapacitor D Cell Series*, available at: http://www.maxwell.com/products/ultracapacitors/products/d-cell-series (accessed 19/04/2013).

[63] Maxwell Technologies, I. (2013)*, Ultracapacitor PC10*, available at: http://www.maxwell.com/products/ultracapacitors/products/pc10-series (accessed 19/04/2013).

[64] CDE Cornell Dubilier, (2012), *Type EDL , Electric Double Layer Supercapacitors*, New Bedford, MA.

[65] Panasonic, (2008), *Electric Double Layer Capacitors (Gold Capacitor)/ HW*.

[66] Panasonic (2013)*, Nickel Metal Hybride Batteries*, available at: http://www.panasonic.com/industrial/batteries-oem/oem/nickel-metal-hydride.aspx (accessed 12/03/2013).

[67] Panasonic *, Lithium Batteries BR Series*, available at: http://industrial.panasonic.com/www-cgi/jvcr13pz.cgi?E+BA+3+AAA4004+BR-AG+7+WW (accessed 03/03/2013).

[68] Yuasa Battery (2006)*, Cylindrical Nicked- Cadmium (NiCd)*, available at: http://www.farnell.com/datasheets/1056237.pdf (accessed 12/04/2013).

[69] Tadiran Batteries GmbH (2011)*, Tadiran Batteries model: SL-360*, available at: http://www.tadiranbatteries.de/eng/products/ltc-batteries/product2.asp?ID=27 (accessed 12/03/2013).

[70] Park, C. and Chou, P. H. (2004), "Power utility maximization for multiple-supply systems by a load-matching switch", *Proceedings of the 2004 International Symposium on Lower Power Electronics and Design, ISLPED'04,* pp. 168.

[71] Park, C. and Chou, P. H. (2007), "AmbiMax: Autonomous energy harvesting platform for multi-supply wireless sensor nodes", *2006 3rd Annual IEEE Communications Society on Sensor and Adhoc Communications and Networks, Secon 2006,* Vol. 1, pp. 168.

[72] Simjee, F. and Chou, P. H. (2006), "Everlast: Long-life, supercapacitor-operated wireless sensor node", *Proceedings of the International Symposium on Low Power Electronics and Design,* Vol. 2006, pp. 197.

[73] Mateu, L., Codrea, C., Lucas, N., Pollak, M. and and Spies, P. (2006), "Energy Harvesting for Wireless Communication Systems Using Thermogenerators", *Proc. of the XXI Conference on Design of Circuits and Integrated Systems (DCIS),* November 22-24, Barcelona, Spain, .

[74] Taneja, J., Jeong, J. and Culler, D. (2008), "Design, modeling and capacity planning for micro-solar power sensor networks", *Proceedings - 2008 International Conference on Information Processing in Sensor Networks, IPSN 2008,* pp. 407.

[75] Fairchild semiconductor, (1997), *NDP6020P / NDB6020P P-Channel Logic Level Enhancement Mode Field Effect Transistor*.

[76] Linear Technology, (1996), *LTC1440/LTC1441/LTC1442 Ultralow Power Single/Dual comparator with Reference*, Milpitas, California, USA.

APPENDICES

Appendix A : Data of the behaviour of the thermoelectric harvester and a variable load connected

	T hot side (ºC)	T cold side (ºC)	ΔT	Resistance (Ω)	Current (mA)	Voltage (mV)	Power (mW)
Oil gearbox(mean)	32	29,1	2,9	0,8	24,6	19,9	0,5
				3,3	18,6	61,9	1,2
				5,7	14,9	84,3	1,3
				7,9	11,8	93,5	1,1
				10,6	9,2	97,2	0,9
				13,3	7,5	99,9	0,8
				15,5	6,6	101,5	0,7
Shaft bearing (mean)	37	33	4	0,8	35,4	28,7	1,0
				3,3	24,1	80,0	1,9
				5,7	18,2	103,3	1,9
				7,9	14,9	117,9	1,8
				10,6	11,4	121,3	1,4
				13,3	9,7	129,4	1,3
				15,5	8,5	131,4	1,1
Bearing driven end (mean)	41	36,3	4,7	0,8	41,0	33,2	1,4
				3,3	28,1	93,2	2,6
				5,7	21,3	120,9	2,6
				7,9	17,0	134,5	2,3
				10,6	13,7	144,9	2,0
				13,3	11,3	150,4	1,7
				15,5	10,0	154,1	1,5
Bearing not driven end	47	40,3	6,7	0,8	57,2	46,3	2,6
				3,3	37,7	125,1	4,7
				5,7	29,6	167,6	5,0
				7,9	23,7	187,3	4,4
				10,6	18,7	197,9	3,7
				13,3	15,5	206,0	3,2
				15,5	13,7	212,6	2,9
Gearbox (Max) windings (Min)	50	42,6	7,4	0,8	61,9	50,1	3,1
				3,3	41,7	138,3	5,8
				5,7	32,0	181,4	5,8
				7,9	25,6	202,6	5,2
				10,6	20,2	214,5	4,3
				13,3	17,1	227,2	3,9
				15,5	15,0	232,7	3,5
Shaft bearing (max)	66	52,7	13,3	0,8	95,2	77,1	7,3
				3,3	71,5	237,4	17,0
				5,7	55,1	312,3	17,2
				7,9	44,1	348,8	15,4
				10,6	34,9	369,5	12,9
				13,3	29,4	391,0	11,5
				15,5	26,0	402,9	10,5
Bearing (max)	78	60,2	17,8	0,8	120,1	97,3	11,7
				3,3	92,3	306,3	28,3
				5,7	70,1	397,4	27,9
				7,9	58,0	457,9	26,5
				10,6	46,2	489,9	22,6
				13,3	38,1	506,9	19,3
				15,5	33,7	520,8	17,5

Appendix B : Technical specifications of the sensor nodes and the gateway.

Technical Specifications	
Supply Voltage	3.3 Volt(typ.) (Min. 1,8V-Max. 3,6V)
Supply Current	330μA at 1MHz, 2.2V Standby: 1.1μA-Off Mode: 0.2 μA
Supply Source	2 AA batteries
Operating Temperature	-40 to 85 ºC (industrial)
Processor	Texas Instruments MPS430F1611
Memory	Program Flash 40Kbytes, RAM 10Kbytes, External EPROM 512K
Core	Risc 16Bit
Clock	8 Mhz Main Clock, 32.768KHz for software generated Real Time Clock
Response	Wake-Up from standby mode in less than 6μs
Range	Indoor/Urban range up to 300m-
Data rate	250KBps, Interface Data Rate up up 115.2Kbps
Operating frequency	2.4 GHz
Receiver Sensitivity	-100dBm

Figure 74: "Quax MS" sensor node. Technical specifications

Technical Specifications	
Supply Voltage	3.3 Volt(typ.) (Min. 1,8V-Max. 3,6V)
Supply Current	330μA at 1MHz, 2.2V Standby: 1.1μA-Off Mode: 0.2 μA
Supply Source	2 AA batteries
Capabilities	Separately power switch for each sensor and peripheral device
Operating Temperature	-40 to 85 ºC (industrial)
Processor	Texas Instruments MPS430F1611
Memory	Program Flash 40Kbytes, RAM 10Kbytes
Core	Risc 16Bit
Clock	12Mhz Main Clock, 32.768KHz Real Time Clock
Response	Wake-Up from standby mode in less than 6μs
Range	Indoor/Urban range up to 300m-
Data rate	250KBps, Interface Data Rate up up 115.2Kbps
Operating frequency	2.4 GHz
Receiver Sensitivity	-100dBm
Connectivity	8 Analog inputs that can be configured as digital too 3 PWM ports 7 Digital I/Os

Figure 75: "Quax DT" sensor node. Technical specifications

Power Specifications	
Supply Voltage	6-24V DC (indoor) or 110-220V AC (outdoor)
Supply Current	500mA @ peak 3.3V DC
	µA @ power down
Operating Temperature	-40°C up to +60 °C
ZigBee Communication	
ZigBee Module	Digi XBee ZB or Digi XBee-PRO ZB RF Module
Power Output	60mW (18dBm)
	100mW EIRP
Indoor/Urban range	up to 300m
Outdoor/RF Line-of-Sight range	up to 1.6km
RF data rate	250Kbps
Interface Data Rate	up to 115.2Kbps
Operating Frequency	2.4 GHz
Receiver Sensitivity	-100dBm
Spread Spectrum Type	DSSS
Networking Topology	Peer-to-Peer / Point-to-Point / Point-to-Multipoint / Mesh
Error Handling	Retries & acknowledgements
Filtering Options	Pan ID / channel / addresses
Channel capacity	12 Direct Sequence Channels
Addressing	65000 network addresses per channel
Encryption	128-bit AES
Antenna Options	U.FL RF connector, chip antenna / whip antenna

Indoor Case	
Sealing	IP40
Weight	140 grams
Width	117 mm
Height	73 mm
Depth	24 mm
Mounting Type	Desk / Wall mounting
Outdoor Case	
Sealing	IP66
Weight	300 grams
Width	240 mm
Height	80 mm
Depth	60 mm
Mounting Type	Desk / Wall Mounting
WiFi Communication	
WiFi Module	Lantronix MatchPort® b/g
Wireless Standards	IEEE 802.11b / IEEE 802.11g
Frequency Range	2.412-2.484 GHz
Output Power	14 dBm +2.0 dBm / - 1.5dBm (does not include antenna gain)
Maximum Receive Sensitivity	-91dBm @ 1Mbps
Data Rates with Automatic Fallback	54 Mbps – 1 Mbps
Range	up to 100 m indoor
Modulation Techniques	OFDM / DSSS / CCK / DQPSK / DBPSK / 64 QAM / 16 QAM
Network Interface	
Interface	Wireless 802.11b / 802.11g
Protocols Supported	ARP / UDP / TCP / Telnet / ICMP / SNMP / DHCP / BOOTP / AutoIP / HTTP / SMTP / TFTP
Security	
IEEE 802.11i-PSK with AES-CCMP Encryption	
WPA-PSK	
TKIP Encryption	
64/128 bit WEP	

Figure 76: Wi-Fi Gateway. Technical specifications

Appendix C : Schematic of power management unit

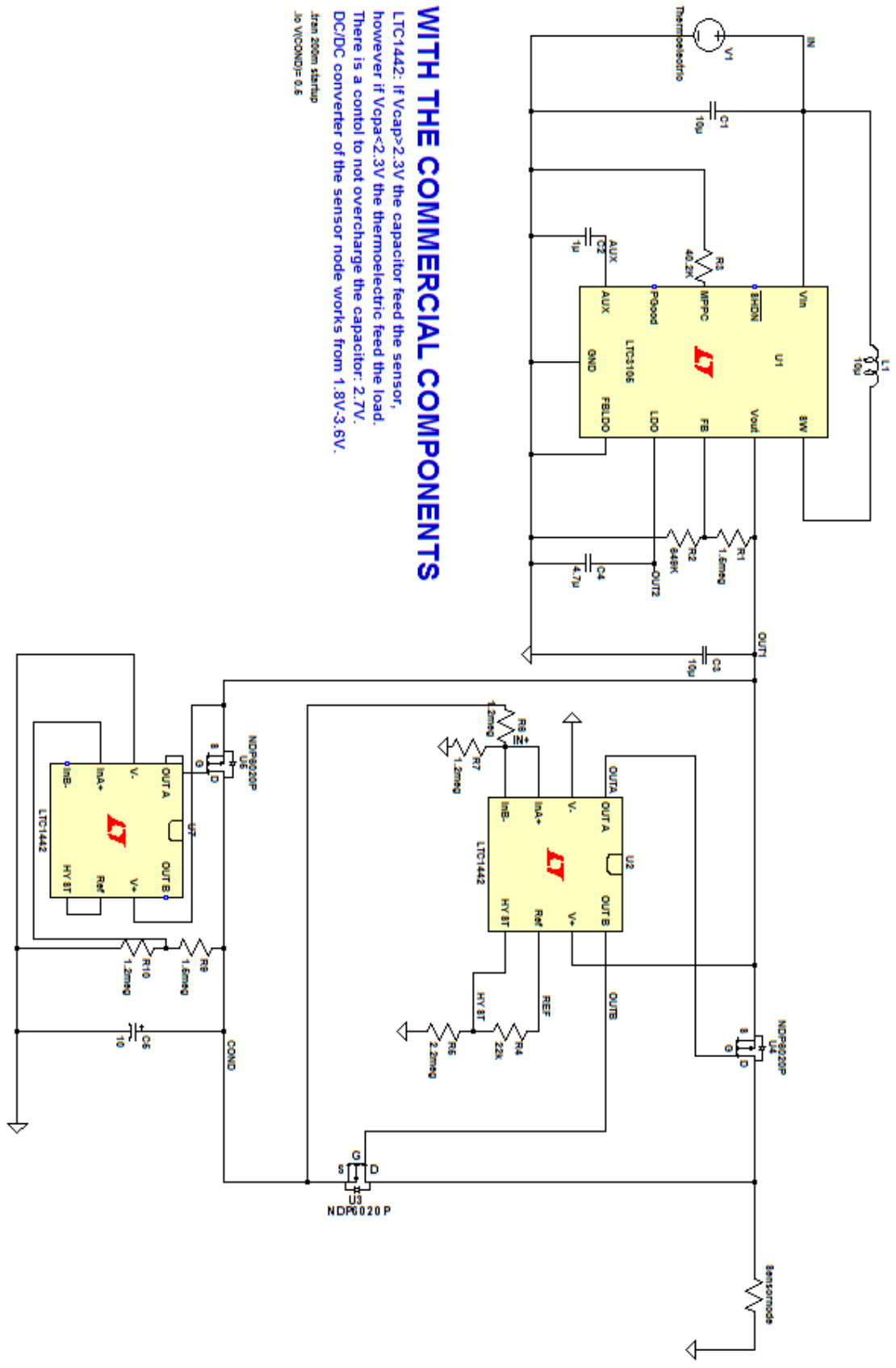

Figure 77: Schematic of the power management circuit and DC/DC converter.

Appendix D : Heating and cooling rates of the bearing casing

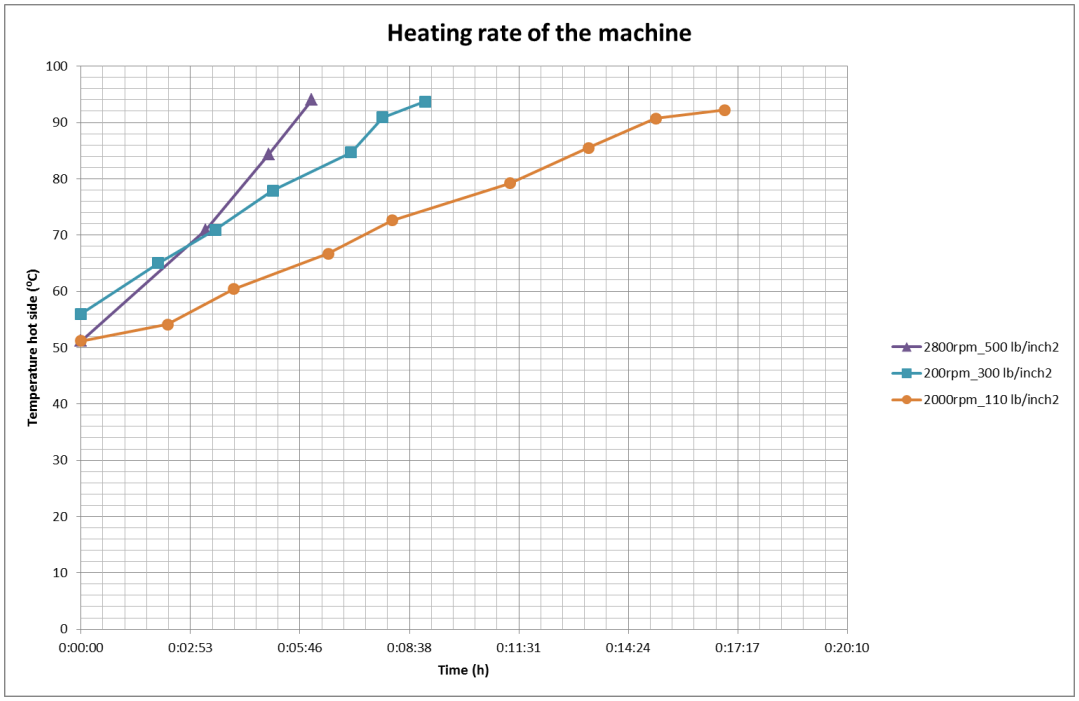

Figure 79: Heating rate of the bearing casing.

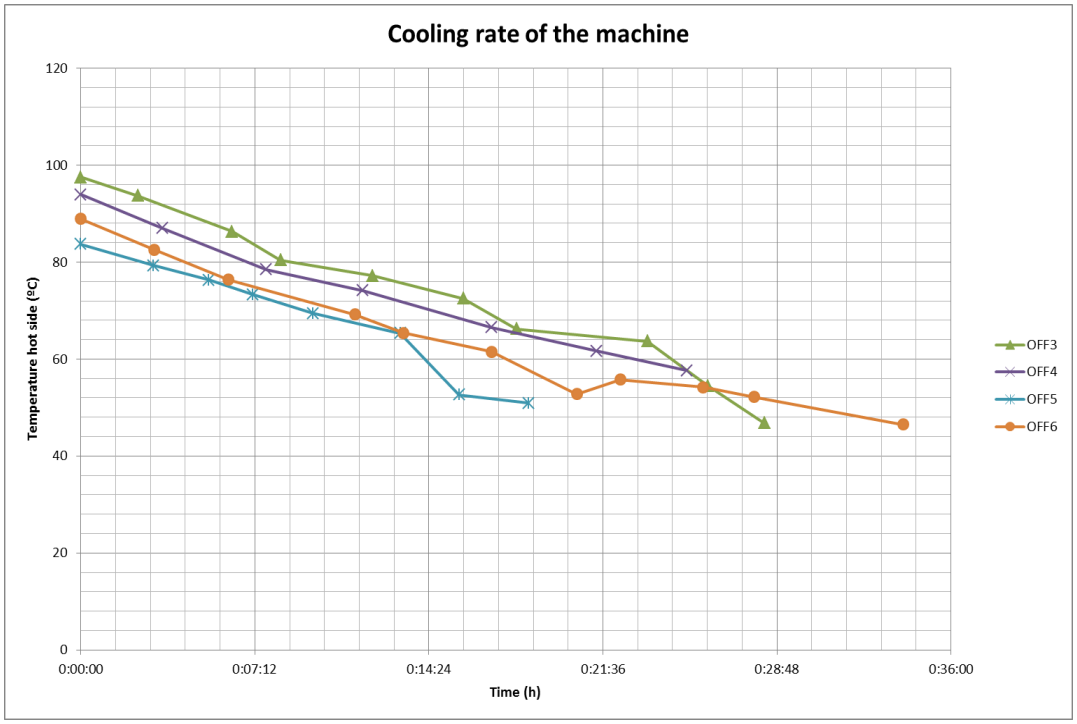

Figure 78: Cooling rate of the bearing casing